SIMULATION AND MODEL DEVELOPMENT FOR AUTO-IGNITION AND REACTION FRONT PROPAGATION IN LOW-TEMPERATURE HIGH-PRESSURE LEAN-BURN ENGINES

by

Jason Brian Martz

A dissertation submitted in partial fulfillment
of the requirements for the degree of
Doctor of Philosophy
(Mechanical Engineering)
in The University of Michigan
2010

Doctoral Committee:

Professor Dionissios N. Assanis, Chair
Professor James F. Driscoll
Professor Margaret S. Wooldridge
Assistant Research Scientist Aristotelis Babajimopoulos
Visiting Research Scientist George A. Lavoie
Scott B. Fiveland, Caterpillar Inc.

To Melissa

ACKNOWLEDGMENTS

There are many people who I wish to thank for making the past six years such an enjoyable experience. Without their support, this work would not have been possible. First and foremost, I would like to thank my thesis advisor, Professor Dennis Assanis. I have known Dennis since 1999, and am grateful for the two opportunities that he has given me over time in his lab. I deeply appreciate his devotion to this university, and to his students both in his lab and in his engines classes. He is an inspirational leader, teacher, mentor and friend.

Next, I would like to thank my doctoral committee members, including Professors Margaret Wooldridge and Jim Driscoll for their support and suggestions throughout the course of this work. Professor Wooldridge has provided much of the optical data used in the validation work within this thesis, while Professor Driscoll has been a tremendous scientific influence, and I would especially like to acknowledge the physical insight that he provided during his turbulent combustion class.

I was extremely fortunate to work closely with Research Scientists Aris Babajimopoulos and George Lavoie. Both George and Aris have provided continuous scientific insight, support and friendship over the past six years. In particular, I'd like to thank Aris for all of the computational guidance and technical assistance that he has provided during my stay. I'd also like to thank George for his scientific leadership and for the inspiration that he has continuously provided throughout the years. Thank you both for constantly being there during this wonderful experience.

I also wish to thank my good friend Dr. Scott Fiveland of Caterpillar Inc. I am truly grateful to Scott for all that he has done, especially for our interaction early on as this topic was under development.

Next, I would like to thank Professor Hong Im, who has been both a great teacher and collaborator. I have learned a tremendous amount from Prof. Im through his classes and during our interactions. Special thanks are also in order for Professor Zoran Filipi for his helpful scientific discussions and suggestions over the years.

I'm also grateful to so many people from the lab for their support. In particular, I'd like to thank Rob Middleton for our numerous collaborations. I also truly appreciate the help of Rob and Mark Hoffman for taking the time to review various sections of this dissertation. I'd like to also thank Bruno Vanzieleghem, Aris and Janardhan Kodavasal for providing their codes as the starting point for this work, and would also like to thank SeungHwan Keum, Chaitanya Sampra and Chris Depcik for their technical help and friendship. In addition, I'd like to thank Brad Zigler, Peter Keros and Stani Bohac for sharing the experimental data used in this dissertation. I would also like to thank my good friends Karl Pass, Guntram Lechner, Jerry Fuschetto and Kayo Ramirez. Thank you to the countless others from home, the Autolab and Professor Sick's group who have made the last several years an unforgettable experience. In addition, I would like to thank my friends from the NCRB and Fuller Pool swim groups.

I'd also like to thank my family, including my mother, grand parents and sister for providing me with their continuous support and encouragement for as long as I can remember. Without you, I would not have made it to where I am today. Finally, I'd like to thank my best friend and wife Melissa. She has been a constant source of love, inspiration, encouragement and support, and has sacrificed so much without complaint over the past six years.

TABLE OF CONTENTS

LIST OF FIGURES

LIST OF TABLES

ABSTRACT

While Homogeneous Charge Compression Ignition (HCCI) combustion is capable of highly efficient, ultra-low NO_x operation, it lacks direct mechanisms for timing and burn rate control and suffers from marginal power densities. Concepts such as Spark-Assisted Compression Ignition (SACI) combustion have shown the ability to partially address these shortcomings, however detailed SACI models are currently lacking.

To address the need for reaction front data within the ultra-dilute, high pressure and preheat temperature SACI regime, laminar premixed reaction front simulations were performed and correlations for burning velocity and front thickness were developed from the resulting dataset. Provided that preheat temperatures were elevated and that burned gas temperatures exceeded 1500 K, moderate burning velocities were observed at equivalence ratios typical of mid and high load HCCI operation. For a given burned gas temperature, burning velocities increased when moving from the SI to the SACI combustion regime, i.e. towards higher dilution and higher pre-heat temperatures.

Given the proximity of SACI pre-heat temperatures to the ignition temperature, additional simulations examined the combustion regime, structure and general behavior of the reaction front as it propagated into an auto-igniting end-gas. While significant increases in burning velocity accompanied the transition from deflagrative to chemically dominated combustion, the reaction front contributed minimally to end-gas consumption once end-gas temperatures exceeded 1100 K.

A model capable of capturing SI, SACI and HCCI combustion modes was formulated and implemented into KIVA-3V. Using the correlated laminar flame speed data, the model was capable of predicting trend-wise agreement with cylinder pressure

and imaging data from an optical SACI engine. The simulated presence of flame surface density suggests that although the simulated reaction fronts are ultra-dilute, they are nevertheless within the flamelet regime during the deflagration portion of SACI combustion. End-gas auto-ignition occurred when the charge compression heating from boundary work and reaction front heat release combined to drive the end-gas to its ignition temperature, providing additional latitude for the execution and control of low temperature combustion processes. Additional simulations were performed to assess the ability of this additional deflagrative combustion mode to enable high efficiency operation with elevated work output relative to HCCI combustion.

CHAPTER 1

INTRODUCTION

1.1 HCCI Background

Homogeneous Charge Compression Ignition (HCCI) combustion is a response to the need for low polluting, highly efficient internal combustion engines. Under ideal conditions, HCCI delivers the most desirable performance and emissions characteristics of premixed spark ignited (SI) and compression ignition direct injection (CIDI) combustion, providing high levels of thermal efficiency with ultra-low engine-out oxides of nitrogen (NO_x) and particulate emissions [1-3].

During HCCI, a highly dilute fuel air mixture is compressed to the point of auto-ignition. Ignition is typically phased in proximity to top dead center (TDC), while combustion occurs in a near constant volume manner. Optimal thermal efficiencies are achieved by phasing combustion shortly after TDC, marking a trade-off between work and heat transfer processes [4, 5]. Because of the near constant volume combustion process, the thermal efficiency of HCCI is less sensitive to combustion timing than in SI or CIDI engines [4, 5]. Although the combustion process is rapid, peak cyclical gas temperatures are limited through high levels of charge dilution with excess air or recirculated exhaust products.

Relative to stoichiometric SI engines, an increase in gross thermal efficiency is made possible by increasing the displacement work of the cycle for a given energy input. The increased compression ratio used to promote auto-ignition, in conjunction with the

elevated ratio of specific heats enabled through lean operation leads to significant relative gains in gross indicated efficiency [6]. In contrast to stoichiometric SI engines, where load and fuel delivery are effectively controlled by varying the trapped air mass through intake throttling at a fixed equivalence ratio, air-dilute HCCI operates un-throttled and controls load by directly regulating the cyclical fuel mass and allowing equivalence ratio to float. As a result, the pumping mean effective pressure (PMEP) penalty associated with throttling is avoided, enhancing the net brake work output and efficiency of the cycle.

In spite of its efficiency drawbacks, the stoichiometric SI engine enjoys a dominant share of the passenger car market largely because of the cost effective reduction of engine out NOx, HC and CO emissions enabled by its three-way catalyst system [7]. In contrast, within HCCI, engine out NO_x emissions are mitigated through the low peak cycle temperatures associated with the ultra-high levels of charge dilution, while particulate emissions (PM) are prevented by avoiding the local equivalence ratio and temperature regimes required for soot precursor formation [8]. Through these in-cylinder emissions control approaches, the need for the costly NOx and particulate after-treatment required by CIDI engines is avoided.

1.2 The HCCI Combustion Process

A general understanding of HCCI was established in the late 1970's through the high speed chemiluminescence and Schlieren imaging studies of Noguchi et al. [9] and Onishi et al. [1]. In contrast to Schlieren images of SI combustion, where sharp density gradients were observed across the flame front, images of HCCI combustion showed a near-uniform mixture density throughout the combustion chamber. Radical species were evenly distributed throughout the combustion chamber during HCCI, while in SI combustion these species were confined to the flame front. Given the thermal and

compositional homogeneity observed for HCCI, it was established that HCCI combustion generally lacked reaction fronts and therefore must be chemically controlled.

Later studies added sequential burning to this conceptual picture. In the Planar Laser Induced Fluorescence (PLIF) imaging study of HCCI by Hultqvist et al. [10], combustion occurred in a distributed, sequential manner throughout the combustion chamber, with the initial ignition sites located in thermally and compositionally favorable areas. The global pressure rise resulting from combustion within the earlier burning zones promoted combustion in the less reactive, later burning ones. The chemiluminescence study of Dec et al. also showed this sequential auto-ignition process, demonstrating that combustion was initiated within the core gasses and was completed in the cooler, near wall, thermal boundary layer regions by the end of the combustion process [11]. This broad distribution of reaction zones throughout the combustion chamber leads to the rapid, yet non-instantaneous combustion process characteristic of HCCI, where combustion durations are typically on the order of 5-15 degrees crank angle (deg CA) [12]. Although short lived, this sequential ignition process has displayed significant thermal and compositional gradients between the burned and unburned zones. For example, Hultqvist et al. [10] observed reaction front-like structures propagating at rates ranging from 5 to 30 m/s from the burned into the unburned regions of the combustion chamber during the later stages of HCCI combustion It could not be determined if this observation was due to reaction front propagation or simply to burned gas expansion.

Ignition within HCCI occurs at intermediate temperatures between 850 and 1200 K [13] and is largely governed by the thermal decomposition of H_2O_2 into OH. This chain branching reaction is responsible for ignition during the premixed portion of diesel combustion, the initiation of SI engine end-gas knock and the commencement of HCCI combustion [13]. Cool flame heat release, if any, only serves to advance the timing of the H_2O_2 decomposition through its effect on the charge's temperature-time history [14].

For the HCCI combustion process to be completed, Sjöberg and Dec [15] showed that peak gas temperatures must exceed 1500 K for completion of the CO to CO_2 conversion reactions, the most prominent of which was shown by kinetic simulation to be the attack of CO by OH.

1.3 HCCI Combustion Challenges

Numerous challenges hamper the commercialization and the feasible operating range of HCCI combustion systems. As HCCI combustion is kinetically controlled, ignition timing and combustion rates are highly sensitive to the local thermodynamic state, which is a function of both the initial state within the cylinder and the path taken during the compression process. Slight variation in the initial state, such as that caused by compositional or thermal variation in the residual fraction from cycle to cycle, can significantly alter the characteristics of combustion in the subsequent cycles [16].

Early HCCI combustion tends to be extremely rapid, given the higher relative reactant temperatures. This can result in elevated peak cylinder pressure, pressure rise rate and ringing [17], while late combustion can lead to partial burning, misfiring and high levels of cycle to cycle variability [18]. Excessive engine out thermal NO_x may also result if peak in-cylinder temperatures are not properly managed, even at low loads [19]. As a result of these limits, the range of ignition timings available to HCCI is generally quite narrow. Unfortunately, at high loads, HCCI combustion control becomes especially problematic, as combustion must be retarded towards the stability and misfire limit in order to comply with mechanical loading, ringing and thermal NOx constraints [4, 20]. This convergence of these limits effectively establishes the maximum load limit of the engine.

The high levels of charge dilution required to moderate mixture reactivity and to mitigate knock and NO_x emissions effectively limit the chemical energy release available

for work production. As a result, the power density of HCCI engines can be a factor of two to three lower than modern heavy-duty, lean burn SI gas and CIDI engines, compromising both mechanical and brake thermal efficiency [6]. The primary path towards improving naturally aspirated HCCI power density is through the lowering of peak cylinder pressure and pressure rise rates. This is accomplished through the lowering of compression ratio and the retarding and lengthening of the overall combustion rates [6], which, as stated above is not possible at high load where combustion has already been retarded to the stability and misfire limit.

1.4 Factors Influencing HCCI Combustion

1.4.1 Fuels

A variety of fuels have been used in HCCI combustion. Early HCCI studies examined gasoline [1, 9] and diesel fuel [21], while Najt and Foster utilized the primary reference fuels isooctane and n-heptane to examine the effect of octane number on combustion phasing [22]. More recent studies have included gasoline, diesel, natural gas, di-methyl ether, hydrogen, and methanol [23]. A variety of dual fuel approaches also exist, where high and low octane number fuels are blended to vary ignition properties in an attempt to control combustion phasing [19, 23-25].

Ignition requirements are fuel specific due to fuel dependent low temperature kinetics [22, 26], while CO oxidation kinetics, which dominate heat release for hydrocarbon fuels, are largely fuel independent [22, 27] . Lower ignition temperatures are desirable, as they allow for combustion to proceed without reaching the burned gas temperatures where NO_x emissions become problematic. At the same time, the ignition temperature of the fuel should be high enough to allow for the use of realistic inlet temperatures and compression ratios [25].

Specific fuel studies include the work of Christensen et al., which examined isooctane, ethanol and natural gas fueled HCCI for a fixed compression ratio of 21:1, where intake manifold temperature (IMAT) and equivalence ratio were adjusted to control combustion phasing [3]. While the thermal efficiencies of HCCI were diesel-like, the peak cylinder pressures corresponding to HCCI combustion were elevated. A follow-up study examined octane number (ON) effects, evaluating pure and blended mixtures of the primary reference fuels (PRF) in addition to 98 octane gasoline, diesel fuel and blends of the commercial fuels [24]. The equivalence ratio was fixed at 0.33, while compression ratio and IMAT were varied to maintain combustion phasing near TDC. From the experimental results, it was noted that in order to maintain combustion phasing at a fixed IMAT, compression ratio had to increase with ON in order to compensate for the increased ignition temperature. In addition, 10-90% mass fraction burn (MFB) durations were noted to decrease with ON, given the overall higher ignition and peak cycle temperatures. The highest gross indicated efficiencies (43%) for the primary reference fuels were obtained with isooctane, using a compression ratio of 21.5:1, while gross indicated efficiencies of around 36-37% were observed for the low octane number blends with compression ratios around 10:1. The relatively moderate decreases in gross indicated efficiency with lower compression ratios were attributed in part to the lower cycle temperatures and heat losses associated with the lower ignition temperature of the low octane number fuels.

1.4.2 Intake Manifold Temperature, Equivalence Ratio and Internal EGR

Given the chemically controlled nature of HCCI, ignition timing and combustion rate are often controlled through IMAT, which is tailored in conjunction with other parameters affecting the mixture reactivity such as compression ratio, intake manifold pressure (MAP), fuel composition, equivalence ratio, exhaust gas recirculation (EGR)

rate and engine speed [22, 28-31]. Elevated IMATs, which hinder power density, can be avoided through the proper tailoring of compression ratio to the fuel type [2].

The slow response time of intake heating systems can make the transient control of HCCI problematic. As a result, internal EGR (IEGR), composed of the residual fraction from the previous cycle, is often substituted for pre-heated air as a diluent in automotive applications, due to the residual's high sensible internal energy [31]. The amount of IEGR is typically controlled by manipulating the valve events. For example, researchers at Stanford were able to achieve up to 5 bar indicated mean effective pressure (IMEP) with naturally aspirated HCCI and varying levels of IEGR. To control IEGR, an electro-hydraulic, fully variable valve train was used with a re-induction strategy, where exhaust was drawn back into the cylinder from the exhaust manifold either by late exhaust valve closing (LEVC) or late intake valve opening (LIVO) [32]. A follow up study used negative valve overlap (re-expansion) and re-induction strategies with full and reduced intake valve lifts [31]. Negative valve overlap in conjunction with direct injection has been used to enable HCCI operation over a wide range of the speed load map of an automotive gasoline engine equipped with an electromechanical valve train. HCCI was possible at speeds from 1000 to 4500 RPM, with BMEP ranging from 1 to 6 bar [33], while cycle average fuel consumption was reduced by 18% relative to the base SI engine. These results are similar to the dual mode SI/HCCI concept reported in [34], where part load HCCI combustion with 30-70% IEGR enabled through negative valve overlap, was examined for speeds ranging from 1000 to 4000 RPM and BMEP's up to 4.5 bar. The average fuel consumption was reduced by 12% relative to SI operation.

The fuel-air equivalence ratios of HCCI range from globally lean to stoichiometric when EGR dilution is used [2, 20]. For air dilute HCCI, the range of equivalence ratio is quite limited. Olsson was able to operate as lean as $\Phi = 0.13$ at idle conditions, however, combustion efficiencies were only on the order of 65% [5]. Dec modeled similar conditions ($\Phi = 0.15$) and found that peak temperatures were too low to

drive combustion to completion [35]. At high loads on the other hand, the maximum equivalence ratio for air dilute HCCI mixtures is limited to $\Phi \sim 0.4$ to 0.5 because of excessive combustion and pressure rise rates, knock, and NO_x emissions [18]. For high load HCCI operation with stoichiometric equivalence ratios and EGR dilution, EGR rates can be as high as 60% [36].

1.4.3 Load Enabling Technologies

Turbo and supercharging are often applied to HCCI in order to overcome the low power densities and mechanical efficiencies associated with the high levels of charge dilution [5, 25, 37]. Unfortunately, because of the elevated mixture dilution ratios and gross thermal efficiencies, HCCI exhaust temperatures are several hundred Kelvin cooler relative to CIDI exhaust [5, 6, 25]. The resulting low enthalpy limits the turbine shaft work output/compressor work input, negatively affecting the ability to increase the intake manifold pressure. To compensate, the kinetic energy of the exhaust gas can be increased by reducing the flow area of the turbine nozzle, however the resulting backpressure increases PMEP, which may significantly detract from the brake work and thermal efficiency [6].

Numerous studies have shown the ability of both turbo and super-charging to improve the power density of HCCI. Christensen et al. were able to increase the maximum net IMEP of HCCI from 5 bar, for naturally aspirated operation, to 14 bar with 300 kPaa of supercharging on a single-cylinder test engine, with fuels including iso-octane, ethanol and natural gas [38]. Olsson et al. achieved 16 bar BMEP with a multi-cylinder, turbocharged HCCI engine using air dilute n-heptane and ethanol mixtures at equivalence ratios on the order of 0.5 with 300 kPaa boost [5], while the maximum BMEP for the same engine in a diesel configuration was 21 bar. At high loads, the brake thermal efficiency of the HCCI engine ranged between 35 and 40% compared to 45% for

the diesel. This difference in BMEP and efficiency was largely due to the higher PMEP imposed by the HCCI air system.

Cooled, external EGR has also been evaluated as a load enabling technology. The single zone HCCI simulations of Dec with the detailed LLNL (Lawrence Livermore National Laboratory) isooctane mechanism [39] showed that the main effect of EGR on HCCI combustion is a thermal one [35], where the lower gammas of EGR dilute mixtures produce lower end of compression temperatures. In addition, the slightly slower burn rates observed at constant ignition timings were attributed to the lower oxygen concentrations of the EGR dilute mixture.

Christensen and Johansson examined naturally aspirated HCCI with EGR at a compression ratio of 18:1 with iso-octane, ethanol and natural gas fuels [30]. Combustion phasing was fixed near TDC by manipulating EGR rate and IMAT, while fuel delivery was kept constant. As EGR rates were increased, combustion became later and slower, however, combustion rates remained excessive. Additional studies by Christensen et al. showed that the load range of HCCI could be extended through the combination of cooled EGR with boosted intake manifold pressure and near stoichiometric equivalence ratios [37]. A maximum gross IMEP of 16 bar was attained with a boost pressure of 250 kPaa and 48% EGR. The peak cylinder pressure was 170 bar, while gross indicated thermal efficiency was 46% with NO_x emissions below 0.04 g/kW-hr.

The utility of EGR for extending HCCI loads has been mixed. For example, the work of Olsson et al. [4] at intermediate loads showed that at comparable location of 50% MFB (CA50), there was negligible difference in combustion rate between EGR and air dilute mixtures. In contrast, Morimoto et al. were able to increase HCCI loads by 20%, relative to an air diluted baseline case, through the use of cooled EGR [40]. Transitioning from 0 to nearly 55% EGR (Φ = 0.27 to 0.50) at constant fueling and similar ignition timings nearly doubled the 10-90 burn duration from 7 to 13° CA. More recently, Dec and Yang [36] have increased the load of a gasoline fueled HCCI engine

from approximately 5 bar gross IMEP for naturally aspirated operation to 16.3 bar gross IMEP at 325 kPaa intake manifold pressure. Without EGR, the maximum equivalence ratio had to be decreased below the baseline level of 0.38 in order to keep the ringing intensity below 5 MW/m^2. As a result, the peak IMEP diminished for the air dilute boosted cases once intake manifold pressures exceeded 180 kPaa, while the use of EGR for these higher load boosted cases provided the retarded CA50 necessary for compliance with the ringing limits.

Concepts employing charge stratification through direct fuel injection, such as premixed charge compression ignition (PCI), can lengthen combustion durations [8]. However, a transition to diffusion controlled combustion with diesel-like emissions can occur once the injection event continues beyond the end of the ignition delay. Bessonette et al. were able to achieve over 16 bar BMEP for PCI combustion using gasoline and diesel fuels, but only with elevated Bosch smoke numbers at high load [41].

1.4.4 SACI Combustion

Several approaches have attempted to trigger HCCI combustion with an external ignition source. These approaches have been subsequently named Spark-Assisted, Compression Ignition (SACI) combustion [42]. Using a laser induced plasma with a mixture of isooctane and natural gas at $\Phi = 0.43$ with a 40° BTDC plasma timing, Kopecek et al. were able to advance the centroid of the heat release rate by approximately 5° CA relative to conventional HCCI combustion [43]; for mixtures with equivalence ratios below $\Phi = 0.37$ the external ignition source had no effect on ignition timing. Additional imaging studies by Kopecek et al. with both laser and spark ignition [44] showed apparent reaction front propagation lasting roughly 10-15° CA before transitioning to HCCI type combustion. The front was attributed to either deflagrative combustion or early HCCI combustion triggered by the ignition source. Similar to the

previous study, reaction fronts could not be produced with either plasma or spark in mixtures having equivalence ratios leaner than $\Phi = 0.36$.

The main effect of the SACI approach used by AVL [45] was the improvement of IMEP coefficient of variation (COV) at low loads, while a secondary effect was the control of combustion phasing, which was on the order of a few degrees CA. It was claimed that flame propagation did not occur under SACI conditions and that the addition of energy from the spark instead triggered localized HCCI combustion.

More recently, the use of spark-assisted HCCI under high load, naturally aspirated conditions in an automotive engine has shown the ability to extend the load of HCCI by approximately 20% for speeds ranging from 1000 to 3000 RPM [46]. The load range was extended through the use of direct injection during both the NVO and compression stroke, along with spark-assist and internal and external EGR under stoichiometric operation.

While spark ignition is used to initiate combustion in both SI and SACI engines, SACI engines employ mixtures with significantly higher unburned gas temperatures (T_u) to ensure end-gas auto-ignition, in addition to high levels of charge dilution to limit both peak burned gas temperatures (T_b) and end-gas combustion rates. In images of SACI combustion from optical engines [47-49], reaction fronts have been shown to originate and propagate away from the spark plug in an organized manner during what has been referred to as the initial deflagration phase of SACI combustion [49]. During this phase, reaction fronts with expansion speeds ranging from 2–5 m/s have been observed by Zigler et al. [47], while Persson et al. [48] have reported expansion speeds from approximately 0.5-10 m/s. The deflagration phase eventually transitions to one dominated by bulk ignition of the end-gas, in a process that appears similar to end-gas knock observed in SI engines [50].

This multi-mode combustion behavior is supported by the global heat release rate analysis of SACI experiments. The initially low heat release rates of SACI are

characteristic of turbulent deflagrative combustion. Around the ignition temperature of the end-gas, these low heat release rates abruptly transition to the short and rapid ones characteristic of end-gas auto-ignition [48, 49, 51]. The potential for deflagrative reaction fronts within SACI has also been predicted by laminar flame simulations. The PREMIX [52] based study of Huang et al. showed that although ultra-dilute, the elevated T_u of mixtures used in HCCI and SACI engines are capable of supporting laminar reactions fronts over a broad range of conditions, except at highly advanced ignition timings or at excessively dilute, low load conditions [51].

1.5 Existing SI Knock Models

A variety of SI knock models are potentially available for the simulation of SACI combustion. For example, zero and quasi-dimensional models such as those in [53] could be used, however, these models currently lack a direct mechanism for determining the turbulent wrinkling of the flamefront, the primary mechanism for the elevated combustion rates within turbulent combustion systems. As a result, empirical expressions are often used for calculating the turbulent flame speed. In addition, these models lack the spatial resolution required to resolve combustion chamber geometry effects, direct injection events, and the potential compositional and thermal stratification occurring within the combustion chamber.

A variety of multi-dimensional CFD models, such as KIVA-3V, can provide the spatial resolution that the zero and quasi-dimensional models lack. In particular, concepts such as the G-Equation coupled with detailed chemical kinetics have been used to model knocking SI combustion [54, 55]. Like the zero dimensional models, the G-Equation relies upon empirical expressions for the turbulent flame speed [56], while the chemical kinetics are also computationally expensive due to their evaluation within each computational cell. In addition, the iso-octane air laminar burning velocity data of

Metghalchi and Keck [57], valid for equivalence ratios ranging from 0.8 to 1.5, were refit to a form from Gulder [58] in an attempt to improve burning velocity predictions under lean SI conditions [59]. Many KIVA-3V knock modeling approaches also assume that combustion within a computational cell is controlled either by reaction front propagation or by homogeneous ignition [54, 60]. More recently, a Damköhler number defined with the turbulent and flame timescales has been used to select between flame and homogeneous reactor models for the modeling SI combustion with knock [55]. Unfortunately, the simulation results using this approach have shown significant dependence to the value of the Damköhler number used in transitioning between combustion models.

There is also a variety of applications of the Coherent Flamelet model [61] for SI combustion with end-gas knock [62, 63], where the laminar burning velocities are also calculated from Metghalchi and Keck [57]. As the authors of these studies had no burning velocity data for very lean or rich mixtures, the burning velocity correlations were linearly extrapolated from the lean or rich correlation extremes to zero laminar flame speeds at equivalence ratios of 0 and 3, respectively. The latest of these approaches [62] models knock with the tabulated lookup of homogeneous ignition simulation results performed with detailed chemical kinetics [64, 65]. Additional studies have used the CFM model with knock integrals to determine the time and location of the onset of knock [66].

1.6 Objective and Document Organization

While many experimental studies of SACI have demonstrated the ability to partially address the ignition, combustion rate control and power density issues associated with HCCI, there is currently a lack of fundamental SACI simulation studies within the

literature. To facilitate the fundamental understanding of SACI combustion and to augment ongoing SACI combustion experiments, the main objective of the current work is to develop and validate a detailed SACI combustion model. A secondary objective is to investigate the relevant mixed mode combustion regime where both reaction fronts and autoignition can occur.

The document is organized as follows:

- The lack of burning velocity and front thickness data within the SACI regime contributes to the current absence of analytical SACI combustion studies within the literature. To address the need for this data within the highly dilute, high pre-heat temperature SACI combustion regime, steady one dimensional laminar reaction front simulations are performed to obtain burning velocity and front thickness data. Correlations of burning velocity and front thickness are developed for this dataset. The results of this study are summarized in Chapter 2.
- An understanding of the combustion regime, structure and general behavior for reaction fronts propagating into auto-igniting end-gases is currently lacking. In addition, limited fundamental data is available for the development and validation of models of this process, which plays are role in the SACI combustion process. These studies are also reported in Chapter 2.
- Chapter 3 outlines the development and implementation of a detailed model for SACI combustion into KIVA-3V. The model includes physically based sub-models for reaction front propagation and end-gas auto-ignition.
- Chapter 4 presents the results of validation studies of the newly developed SACI combustion model. Validation is performed with data from SI metal engine experiments and with data from optical engine experiments examining SACI combustion.
- In Chapter, 5 the KIVA-3V SACI combustion model is exercised in an attempt to extend the range of low temperature combustion concepts with SACI combustion.

- Finally, conclusions and recommendations for future work are presented in Chapter 6.

The topics in this dissertation have also been reported in the following publications:

Lavoie, G.A., **Martz, J.B**., Wooldridge, M.S. and Assanis, D.N., "A Multi-Mode Combustion Diagram for Spark Assisted Compression Ignition," *Combustion and Flame* 157: 1106-1110, 2010.

Martz, J.B., Kwak, H., Im, H.G., Lavoie, G.A. and Assanis, D.N., "Combustion Regime of a Reacting Front Propagating into an Auto-Igniting Mixture," *Proceedings of the Combustion Institute* (In Press), 2010.

Martz, J.B., Middleton, R.J., Lavoie, G.A., Babajimopoulos, A. and Assanis, D.N., "A Computational Study and Correlation of Premixed Isooctane-Air Laminar Flame Properties under Spark Ignited and Spark Assisted Compression Ignition Engine Conditions," *Combustion and Flame*, 2010 (Accepted).

Martz, J.B., Kwak, H., Im, H.G., Lavoie, G.A., Assanis, D.N., Fiveland, S.B., "Propagation of a Reacting Front in an Auto-Igniting Mixture," *Proceedings of the 6th U.S. National Combustion Meeting* (2009).

1.7 References

1. Onishi, S., Jo, S.H., Shoda, K., Jo, P.D., and Kato, S., "Active Thermo-Atmosphere Combustion (ATAC) - A New Combustion Process for Internal Combustion Engines," SAE Paper 790501, 1979.

2. Thring, R., "Homogeneous-Charge Compression-Ignition (HCCI) Engines," SAE Paper 892068, 1989.

3. Christensen, M., Johansson, B., and Einewall, P., "Homogeneous Charge Compression Ignition (HCCI) Using Isooctane, Ethanol and Natural Gas - A Comparison with Spark Ignition Operation," SAE Paper 972874, 1997.

4. Olsson, J.O., Tunestal, P., Ulfvik, J., and Johansson, B., "The Effect of Cooled EGR on Emissions and Performance of a Turbocharged HCCI Engine," SAE Paper 2003-01-0743, 2003.

5. Olsson, J.O., Tunestal, P., Haraldsson, G., and Johansson, B., "A Turbo Charged Dual Fuel HCCI Engine," SAE Paper 2001-01-1896, 2001.

6. Hiltner, J., Fiveland, S.B., Agama, R., and Willi, M., "System Efficiency Issues for Natural Gas Fueled HCCI Engines in Heavy-Duty Stationary Applications," SAE Paper 2002-01-0417, 2002.

7. Heywood, J.B., 1988, *Internal Combustion Engine Fundamentals*. McGraw-Hill, New York.

8. Jacobs, T.J., *Simulatneous Reduction of Nitric Oxide and Particulate Matter Emissions from a Light-Duty Diesel Engine Using Combustion Development and a Diesel Oxidation Catalyst*, Ph.D. Thesis University of Michigan, Ann Arbor (2005).

9. Noguchi, M., Tanaka, Y., Tanaka, T., and Takeuchi, Y., "A Study on Gasoline Engine Combustion by Observation of Intermediate Reactive Products during Combustion," SAE Paper 790840, 1979.

10. Hultquvist, A., Christensen, M., Johansson, B., Richter, M., Nygren, J., Hult, J., and Alden, M., "The HCCI Combustion Process in a Single Cycle - High-Speed Fuel Tracer LIF and Chemiluminescence Imaging," SAE Paper 2002-01-0424, 2002.

11. Dec, J.E., Hwang, W., and Sjöberg, M., "An Investigation of Thermal Stratification in HCCI Engines Using Chemiluminescence Imaging," SAE Paper 2006-01-1518, 2006.

12. Fiveland, S.B., and Assanis, D.N., "A Four-Stroke Homogeneous Charge Compression Ignition Engine Simulation for Combustion and Performance Studies," SAE Paper 2000-01-0332, 2000.

13. Westbrook, C.K., "Chemical Kinetics of Hydrocarbon Ignition in Practical Combustion Systems," *Proceedings of the Combustion Institute* 28: 1563-1577, 2000.

14. Ribaucour, M., Minetti, L., Sochet, L., Curran, H., Pitz, W.J. and Westbrook, C.K., "Ignition of Isomers of Pentane: An Experimental and Kinetic Modeling Study," *Proceedings of the Combustion Institute* 28: 1671-1678, 2000.

15. Sjöberg, M. and Dec, J.E., "An Investigation Into Lowest Acceptable Combustion Temperatures for Hydrocarbon Fuels in HCCI Engines," *Proceedings of the Combustion Institute* 30: 2719-2726, 2005.

16. Glewen, W.J., Wagner, R.M., Edwards, D.E. and Daw, C.S., "Analysis of Cyclic Variability in Spark-Assisted HCCI Combustion Using a Double Wiebe Function," *Proceedings of the Combustion Institute* 32:.2885-2892, 2009.

17. Eng, J.A., "Characterization of Pressure Waves in HCCI Combustion," SAE Paper 2002-01-2859, 2002.

18. Olsson, J.O., Tunestal, P., Johansson, B., Fiveland, S.B., Agama, R., Willi, M., and Assanis, D.N., "Compression Ratio Influence on Maximum Load of a Natural Gas Fueled HCCI Engine," SAE Paper 2002-01-0111, 2002.

19. Flowers, D., Aceves, S., Smith, R., Torres, J., Girard, J. and Dibble, R., "HCCI In a CFR Engine: Experiments and Detailed Kinetic Modeling," SAE Paper 2000-01-0328, 2000.

20. Ryan, T.W. and Callahan, T., "Homogeneous Charge Compression Ignition of Diesel Fuel," SAE Paper 961160, 1996.

21. Gray, A. and Ryan, T., "Homogeneous Charge Compression Ignition (HCCI) of Diesel Fuel," SAE Paper 971676, 1997.

22. Najt, P.M. and Foster, D.E., "Compression-Ignited Homogeneous Charge Combustion," SAE Paper 830264, 1983.

23. Epping, K., Aceves, S., Bechtold, R., and Dec, J.E., "The Potential of HCCI Combustion for High Efficiency and Low Emissions," SAE Paper 2002-01-1923, 2002.

24. Christensen, M., Hultqvist, A. and Johansson, B., "Demonstrating the Multi Fuel Capability of Homogeneous Charge Compression Ignition Engine with Variable Compression Ratio," SAE Paper 1999-01-3679, 1999.

25. Olsson, J.O., Tunestal, P. and Johansson, B., "Boosting for High Load HCCI," SAE Paper 2004-01-0940, 2004.

26. Kelly-Zion, P.L., and Dec, J.E., "A Computational Study of the Effect of Fuel Type on Ignition Time in HCCI Engines," *Proceedings of the Combustion Institute* 28: 1187-1194, 2000.

27. Law, C., 2006, *Combustion Physics*. Cambridge University Press, New York.

28. Fiveland, S.B., *Modeling and Experimental Studies of a Large-Bore Natural Gas Engine Operating on Homogeneous Charge Compression Ignition*, Ph.D. Thesis University of Michigan, Ann Arbor (2001).

29. Christensen, M., and Johansson, B., "Supercharged Homogeneous Charge Compression Ignition (HCCI) with Exhaust Gas Recirculation and Pilot Fuel," SAE Paper 2000-01-1835, 2000.

30. Christensen, M., and Johansson, B., "Influence of Mixture Quality on Homogeneous Charge Compression Ignition," SAE Paper 982454, 1998.

31. Caton, P.A., Song, H.H., Kaahaaina, N.B., and Edwards, C.F., "Strategies for Achieving Residual -Effected Homogeneous Charge Compression Ignition Using Variable Valve Actuation," SAE Paper 2005-01-0165, 2005.

32. Kaahaaina, N.B., Simon, A.J., Caton, P.A., and Edwards, C.F., "Use of Dynamic Valving to Achieve Residual-Affected Combustion," SAE Paper 2001-01-0549, 2001.

33. Wolters, P., Salber, W., Geiger, J.D. Duesmann, M., and Dilthey, J., "Controlled Auto Ignition Combustion Process with an Electromechanical Valve Train," SAE Paper 2003-01-0032, 2003.

34. Allen, J., and Law, D., "Variable Valve Actuated Controlled Auto-Ignition: Speed Load Maps and Strategic Regime of Operation," SAE Paper 2002-01-0422, 2002.

35. Dec, J.E., "A Computational Study of the Effects of Low Fuel Loading and EGR on Heat Release Rates and Combustion Limits in HCCI Engines," SAE Paper 2002-01-1309, 2002.

36. Dec, J.E., and Yang, Y., "Boosted HCCI for High Power without Engine Knock and with Ultra-Low NOx Emissions - Using Conventional Gasoline," SAE Paper 2010-01-1086, 2010.

37. Christensen, M., and Johansson, B., "Supercharged Homogeneous Charge Compression Ignition (HCCI) with Exhaust Gas Recirculation," SAE Paper 2000-01-1835, 2001.

38. Christensen, M., Johansson, B., Amneus, P., and Mauss, F., "Supercharged Homogeneous Charge Compression Ignition," SAE Paper 980787, 1998.

39. Curran, H., Gaffuri, P., Pitz, W.J., and Westbrook, C.K., "A Comprehensive Modeling Study of iso-Octane Oxidation," *Combustion and Flame*, Vol. 129: 253-280, 2004.

40. Morimoto, S., Kawabata, Y., Sakurai, T., and Amano, T., "Operating Characteristics of a Natural Gas-Fired Homogeneous Charge Compression Ignition Engine (Performance Improvements Using EGR) ," SAE Paper 2001-01-1034, 2001.

41. Bessonette, P.W., Schleyer, C.H., Duffy, K.P., Hardy, W.L., and Liechty, M.P., "Effect of Fuel Property Changes on Heavy-Duty HCCI Combustion," SAE Paper 2007-01-0191, 2007.

42. Lavoie, G., Martz, J., Wooldridge, M., and Assanis, D., "A Multi-Mode Combustion Diagram for Spark Assisted Compression Ignition," *Combustion and Flame*, Vol. 157: 1106-1110, 2010.

43. Kopecek, H., Winter, E., Lackner, M., Winter, F., and Hultqvist, A., "Laser-Stimulated Ignition in a Homogeneous Charge Compression Ignition Engine," SAE Paper 2004-01-0937, 2004.

44. Weinrotter, M., Winter, E., Iskra, K., Neger, T., Olofsson, J., Seyfried, H., Alden, M., Lackner, M., Winter, F., Vressner, A., Hultqvist, A., and Johansson, B., "Optical Diagnostics of Laser-Induced and Spark Plug-Assisted HCCI Combustion," SAE Paper 2005-01-0129, 2005.

45. Fuerhapter, A., Piock, W., and Fraidl, G., "CSI - Controlled Auto Ignition - the Best Solution for the Fuel Consumption - Versus Emission Trade-Off?," SAE Paper 2003-01-0754, 2003.

46. Yun, H., Wermuth, N., and Najt, P.M., "Extending the High Load Operating Limit of a Naturally-Aspirated Gasoline HCCI Combustion Engine," SAE Paper 2010-01-0847, 2010.

47. Zigler, B., *An Experimental Investigation of the Properties of Low Temperature Combustion in an Optical Engine*, Ph.D. Thesis University of Michigan, Ann Arbor (2008).

48. Persson, H., Hultqvist, A., Johansson, B., and Remon, A., "Investigation of the Early Flame Development in Spark-Assisted HCCI Combustion Using High-Speed Chemiluminescence Imaging," SAE Paper 2007-01-0212, 2007.

49. Reuss, D.L., Kuo, T., Silvas, G., Natarajan, V., and Sick, V., "Experimental Metrics for Identifying Origins of Combustion Variability During Spark-Assisted Compression Ignition," *International Journal of Engine Research*, Vol. 9: 409-434, 2008.

50. Schiessl, R., Dreizler, A., Maas, U., Grant, A., and Ewart, P., "Double-Pulse PLIF Imaging of Self-Ignition Centers in an SI Engine," SAE Paper 2001-01-1925, 2001.

51. Huang, Y., Sung, C., and Eng, J.A., "Dilution Limits of n-Butane/Air Mixtures Under Conditions Relevant to HCCI Combustion," *Combustion and Flame*, Vol 136: 457-466, 2004.

52. Kee, R., Grcar, J., Smooke, M., and Miller, J., "A Fortran Program for Modeling Steady Laminar One-Dimensional Premixed Flames," Sandia National Laboratory Report SAND85-8240, 1985.

53. Filipi, Z. and Assanis, D.N., "Quasi-dimensional Computer Simulation of the Turbocharged Spark-Ignition Engine and Its Use for 2- and 4-valve Engine Matching Studies," SAE Paper 910075, 1991.

54. Liang, L., Reitz, R., Iyer, C., and Yi, J., "Modeling Knock in Spark-Ignition Engines Using a G-Equation Combustion Model Incorporating Detailed Chemical Kinetics," SAE Paper 2007-01-0165, 2007.

55. Yang, S. and Reitz, R.D., "Improved combustion submodels for modeling gasoline engines with the level set G equation and detailed chemical kinetics," *Proceedings of the Institution of Mechanical Engineers, Part D, Journal of Automobile Engineering*, Vol.223 (5): 703-726, 2009.

56. Peters, N., 2000. *Turbulent Combustion*. Cambridge University Press, New York.

57. Metghalchi, M. and Keck, J., "Burning Velocities of Mixtures of Air with Methanol, Isooctane, and Indolene at High Pressure and Temperature," *Combustion and Flame*, Vol 48: 191-210, 1982.

58. Gülder, O.L., "Correlations of Laminar Combustion Data for Alternative S.I. Engine Fuels," SAE Paper 841000, 1984.

59. Liang, L. and Reitz, R.D., "Spark Ignition Engine Combustion Modeling Using a Level Set Method with Detailed Chemistry," SAE Paper 2006-01-0243, 2006.

60. Eckert, P., Kong, S.C., and Reitz, R.D., "Modelling Autoignition and Engine Knock Under Spark Ignition Conditions," SAE Paper 2003-01-0011, 2003.

61. Baritaud, T., Duclos, J., and Fusco, A., "Modeling Turbulent Combustion and Pollutant Formation in Stratified Charge Engines," *Proceedings of the Twenty-Sixth International Symposium on Combustion*: 2627-2635, 1996.

62. Colin, O., Benkenida, A., and Angelberger, C., "3D Modeling of Mixing, Ignition and Combustion Phenomena in Highly Stratified Gasoline Engines," *Oil and Gas Science and Technology-Rev. IFP*, Vol. 58(1): 47-62, 2003.

63. Colin, O. and Benkenida, A., "The 3-Zones Extended Coherent Flame Model (ECFM3Z) for Computing Premixed/Diffusion Combustion," *Oil and Gas Science and Technology-Rev. IFP*, Vol. 59(6): 593-609, 2004.

64. Knop, V. and Jay, S., "Latest Developments in Gasoline Auto-Ignition Modelling Applied to an Optical CAI Engine," *Oil and Gas Science and Technology-Rev. IFP*, Vol. 61(1): 121-137, 2006.

65. Colin, O., da Cruz, A.P., and Jay, S., "Detailed chemistry-based auto-ignition model including low temperature phenomena applied to 3-D engine calculations," *Proceedings of the Combustion Institute* 30: 2649-2656, 2005.

66. Teraji, A., Tsuda, T., Noda, T., Kubo, M., and Itoh, T., "Development of a Three-Dimensional Knock Simulation Method Incorporating a High-Accuracy Flame Propagation Model," *International Journal of Engine Research* Vol. 6 (1): 73-83, 2005.

CHAPTER 2

REACTION FRONT SIMULATIONS UNDER SACI COMBUSTION CONDITIONS

Multiple premixed combustion modes are employed in both current production and research based engine systems. A multi-mode combustion diagram (MMCD) has been proposed to separate the deflagration dominated SI combustion regime from that of the near homogeneous compression-ignited HCCI combustion regime and the SACI combustion regime, where elements of SI and HCCI combustion are combined [1]. The MMCD diagram shown in Figure 2.1 separates these combustion regimes for an iso-octane air mixture in terms of T_u and Φ at TDC. By selecting the appropriate T_u and Φ, the corresponding T_b is obtained from constant pressure equilibrium calculations, shown for a pressure of 40 bar in the figure. The dashed line at 2200 K (residual gas fraction) and the solid line at 2000 K (air) represent the approximate T_b's corresponding to NO_x emissions of 1 g/kg fuel; beyond these limits, NO_x aftertreatment is typically required. The bulk quench limit line corresponds to a T_b of 1500 K, below which Sjöberg and Dec have noted insufficient CO to CO_2 oxidation during HCCI combustion [2]. Moving from the left to right on the diagram, several additional limit lines are encountered. The flame limit line is drawn for laminar burning velocities ranging from 10-15 cm/s, which correspond to experimental engine limit conditions reported by Flynn et al. [3] and Lavoie and Blumberg [4], while the knock limit line is defined as the T_u where constant

volume combustion isentropically compresses the end-gas to 1000 K. The flame speeds in the figure are calculated from [5]. The auto-ignition line (for late combustion) and the early combustion limit lines are obtained with the ignition delay correlation of He et al. [6] while noting that for properly phased HCCI combustion, the ignition delay at TDC conditions is typically on the order of 10 crank angle degrees, regardless of engine speed [7]. At 1000 RPM, 10 crank angle degrees correspond to approximately 1.6 ms A reasonable range of ignition timings was defined by varying T_u such that the corresponding ignition delays vary by +/- 50% from that at TDC, resulting in a ±5 degree crank angle change in ignition delay at 1000 RPM. The circles shown on the diagram correspond to SI combustion experiments [4], the triangles to HCCI combustion experiments [2, 8] and the dashed ovals to SACI experiments [9-14].

If the turbulent reaction fronts observed within the SACI combustion regime are be modeled as turbulent flames [15], then detailed information pertaining to the laminar reaction front is needed. This information includes the premixed laminar burning velocity and the reaction front thickness [16]. In this study, iso-octane has been used as a surrogate for gasoline, the incumbent fuel for automotive SI, SACI and HCCI applications, given the similar laminar burning velocities [17] and ignition delays [7] of the two fuels. From the previous high pressure iso-octane air flame studies shown in Table 2.1, it is apparent that the works of Metghalchi and Keck [18], Ryan and Lestz [19], Bradley et al. [20] and Jerzembeck et al. [17] are confined primarily to the relatively near stoichiometric, low T_u's characteristic of the SI combustion regime.

Two previous computational studies are also listed in Table 2.1. While the range of these studies is wider than that of the experiments, these studies are largely confined to the T_u's and pressures associated with conventional SI combustion. For example, the work of Göttgens et al. produced laminar burning velocity and thickness correlations for a range of fuels, including propane, examining Φ from 0.3 to 1.0, however pressure and pre-heat temperature only ranged from 1 to 40 bar and 298 to 800 K, respectively [21].

In addition, the computational study of Müller et al. [22] correlated the laminar burning velocity and flame temperature for a variety of fuels including iso-octane, however the range of Φ in this study was limited to values between 0.6 to 1.0. To address the need for ultra dilute, high pressure and high pre-heat temperature reaction front data within the SACI regime, a large dataset of simulated iso-octane air reaction fronts relevant to both the SI and SACI combustion regimes has been generated with a one dimensional laminar flame simulation. The results and insight gained from this work, along with correlations for the burning velocity and reaction front thickness of the steady simulation results are reported in Section 2.3.

The above study of steady reaction fronts was performed at unburned temperatures in proximity to the ignition temperature. The behavior and combustion regime of reaction fronts propagating into auto-igniting end-gases during SACI combustion [23-25] is not well understood. To better understand the behavior of fronts under these conditions and to support their modeling in KIVA-3V, two model problems are used to investigate the key features of front propagation into end-gasses with varying levels of reaction progress resulting from auto-ignition. These model problems include both steady flow reactor and transient one dimensional simulations, which are respectively described in Sections 2.5 and 2.6.

2.1 Reaction Front Simulation Descriptions

The constant pressure simulations of laminar, planar iso-octane air reaction fronts discussed in Section 2.3 and 2.6 were performed with HCT [26], which solves the transient, one dimensional momentum, species and energy transport equations. HCT has been used both in the simulation of laminar flames [27-30] and in the development and validation of chemical kinetic mechanisms [31-35]. To improve simulation accuracy, an adaptive mesh was used to produce a fine mesh in the vicinity of the reaction front. The

mesh in the current work had a total of 75 cells, 30 of which were adaptive. HCT was configured so that the reaction front propagated towards the left, closed boundary of the domain, while the domain's right boundary was open and set to the domain pressure. External and radiative heat losses were neglected, while the initial jump to the product composition and temperature across the front was determined from constant pressure equilibrium calculations.

Within the HCT calculations, the premixed laminar burning velocity, S_L, was found in part with S_b, the time rate of change of the position of the reaction front, defined as the location of the average temperature between the maximum temperature within the HCT domain (T_{max}) and T_u. The corresponding burning velocity at the front position, S_f, was found with the gas velocity at the reaction front position, u_f, and S_b, where $S_f = S_b - u_f$. In turn, S_L was calculated by assuming quasi-steady front propagation and then applying the continuity equation to a control volume situated between the unburned gas and the front position, so that $S_L = \rho_f S_f / \rho_u$, where the density at the reaction front position and of the unburned gas are ρ_f and ρ_u, respectively. During steady front propagation, the burning velocities predicted by the above approach are equivalent to those calculated with the expression $S_L = S_b$ [27].

For the steady flow reactor simulations in Section 2.5, CHEMKIN SENKIN [36] was utilized to obtain homogeneous ignition solutions while PREMIX [37] was used to simulate steady reaction front propagation. Both simulations were configured as constant pressure reactors, while radiative and external heat losses were also neglected. Because mass burning fluxes were constant throughout the PREMIX domain, S_L was determined with $S_L = \rho_{in} S_{in} / \rho_u$, where ρ_{in} and S_{in} are the density and burning velocity at the inlet to the PREMIX reactor.

The chemical kinetics calculations in this work were performed with the skeletal 215 species iso-octane mechanism of Tham et al. [38], which was developed from the detailed Lawrence Livermore National Lab iso-octane mechanism [35]. In addition, the

Sandia TRANSPORT [39] routine was used to calculate mixture average mass and thermal transport properties for the reaction front simulations. Unless otherwise noted, air composition for all simulations was one mole of molecular oxygen per 3.76 moles of molecular nitrogen.

2.2 Mechanism and Simulation Validation

To verify the validity of the chemical mechanism and simulation, results from HCT ignition delay and flame speed predictions were compared to several fundamental experiments. Predicted constant volume ignition delays were compared to the results of the high and low pressure iso-octane air shock tube experiments of Davidson et al. [40], Vasu et al. [41] and Shen et al. [42], for Φ = 1.0, 0.5 and 0.25, as shown in Figure 2.2. For these simulations, HCT was initialized with the experimental post shock conditions reported in Shen et al. and Davidson et al., while the computational ignition delay was defined as the time to the maximum time rate of hydroxyl (OH) change. Computational ignition delays calculated with the time to the maximum rate of temperature change were quite similar. Good overall agreement between the experiments and computations was observed for temperatures in excess of 1000 K, except for the 10 atmosphere stoichiometric experiments of Shen. The agreement with the dataset of Davidson under similar conditions was significantly better. At temperatures below 1000 K, the predicted ignition delays were longer than those of the experiments; this behavior is comparable to that observed with the detailed mechanism [35].

The initial simulation of atmospheric reaction fronts produced elevated laminar burning velocities relative to experimental values, which is consistent with the experience of Jerzembeck et al. [17]. To compensate, the mixture thermal conductivity was scaled by a factor of 0.8 for all subsequent simulations, reducing predicted atmospheric laminar burning velocities by roughly 10% relative to those with no thermal conductivity scaling

for the atmospheric flames. Figure 2.3 (left) compares the atmospheric pressure laminar burning velocities obtained from HCT to the stretch corrected iso-octane air experiments of Davis and Law [43] and Kumar et al. [44]. With the thermal conductivity scaling, good overall agreement was noted across the range of Φ (0.6 to 1.5) and T_u (298 to 470 K).

In Figure 2.3 (right), the HCT predicted laminar burning velocities are compared to the results of the stretch-corrected atmospheric experiments of Kumar et al. and to the stretch corrected high pressure experiments of Jerzembeck et al. at 10 and 25 bar [17]. Consistent with the Jerzembeck high pressure experiments, the high pressure HCT validation simulations used a volume fraction of molecular oxygen in air of 20.5%. The predicted lean cases showed good agreement with the high pressure experiments, while the simulation slightly under-predicted the high pressure stoichiometric burning velocities. The poor agreement for the rich Φ's has been attributed in part to the lack of rich kinetic pathways within the detailed iso-octane mechanism [17]. Finally, while the simulation consistently under-predicted the results of the 25 bar data set, the lean results were within the range of the uncertainty reported for the experiments.

2.3 Steady Reaction Fronts Under SI and SACI Conditions

The simulation of steady, laminar premixed reaction fronts within the SI and SACI regime was performed with HCT. This range of simulated conditions significantly extends upon that of previous works shown in Figure 2.4. A total of 770 constant pressure laminar burning velocity simulations were performed, with Φ, T_u and pressure ranging from 0.1 to 1.0, 298 to 1000 K and 1 to 250 bar, respectively, as shown in Table 2.2.

The convergence to steady burning velocity and reaction front propagation was determined by allowing the transient HCT solution to evolve in time until the moving

average of the current calculation of S_L was within the larger of 0.01 cm/s or 0.1% of the moving average of the previous 10 S_L calculations. The simulations were typically run for an additional 50 to 150 S_L calculations once at a steady S_L to conclusively ensure convergence to a steady burning velocity. In addition, in the event that steady burning velocities were predicted during auto-ignition, the reaction front was considered to be unsteady in the event that the temperature rise within the unburned gas exceeded 0.5% of its initial value. In most cases, this criteria was not required, as burning velocities were noted to increase during auto-ignition, as described more fully in Section 2.6.

Using the above criteria, 534 steady reaction fronts were obtained from the initial 770 simulations. Of the 534 steady fronts, 53 had a steady S_L below 5 cm/s, which has been traditionally used as a flammability limit because of the lack of external and radiative heat losses within the computations [30]. Consistent with Göttgens et al. [21] and Müller et al. [22], these points were not included in the steady correlations. Steady reaction fronts were not obtained for 103 of the simulations that auto-ignited and for 133 of the simulations that quenched. When quenching, the initial temperature jump imposed upon the domain was smoothed over time via diffusion rather than forming a propagating front.

The range of conditions where steady reaction front propagation was observed depended on both T_b and pressure. Steady reaction fronts could be established when T_b exceeded 1500 K for pressures up to 250 bar and for Φ as low as 0.5. As pressure decreased, the range of Φ where steady fronts were obtained broadened. For T_b in excess of 1500 K, and for pressures up to 60 bar, steady reaction fronts could be established for as low as Φ = 0.4, while at pressures below 15 bar, steady reaction fronts could be established as low as Φ= 0.3. For fronts with T_b less than 1500 K, corresponding primarily to Φ = 0.2 and below, no steady reaction fronts were observed with burning velocities in excess of 5 cm/s. Replacing the 5 cm/s cutoff limit with a mass burning flux based limit as suggested by [9] did not improve the yield of steady points.

Correlations of the burning velocities of steady fronts from the current work [5] were fit using the two equation asymptotic burning velocity form of Göttgens et al. [21] along with modified inner layer temperature and adiabatic flame temperature expressions developed in [5]. An additional correlation for the flame thickness, which was based upon the maximum temperature gradient within the reaction front, was also fit with forms from Göttgens et al. [21].

The laminar burning velocity, S_L, of the steady dataset was fit with Equations (2.1) through (2.3), where the fit parameters for Equations (2.1) and (2.2) are included in Table 2.3:

$$S_L = F\left(Y_f^u\right)^M \exp\left(-G/T^0\right)\left(\frac{T_u}{T^0}\right)\left(\frac{T_b - T^0}{T_b - T_u}\right)^n \tag{2.1}$$

Equation (2.1) includes terms for Y_f^u, the fuel mass fraction of the unburned gas and the inner layer temperature, T^0, which is representative of the crossover temperature within the flame [45]. The inner layer temperature is provided by Equation (2.2):

$$T^0 = \left(\frac{-E}{\ln\left(p/B\right)}\right)\left(Y_f^u + C_7\right)^{C_8} + C_9 T_u + a_1 p^{a_3}\left(\left(Y_f^u\right)^{a_2} - Y_{f,stoich}^{a_2}\right) \tag{2.2}$$

In addition, Equation (2.1) requires an expression for the constant pressure adiabatic flame temperature, T_b, which is calculated with Equation (2.3), using the fit parameters from Table 2.4:

$$T_b = T_u + \Phi\left(c + d\Phi + e\Phi^2 + fT_u + gp\right) \tag{2.3}$$

Over the range of the dataset, comparison of the correlation predicted burning velocities to the HCT steady burning velocities produced an average error of 2.5% with a standard deviation of 3.0%.

The dataset's flame thickness, δ, was fit with Equation (2.4), using the fit parameters from [5] and T_b, T^0 and S_L, determined from Equations (2.1) - (2.3).

Equation (2.4) includes l_F, given by Equation (2.5), and an expression for the ratio of mixture thermal conductivity to heat capacity, provided by Equation (2.6).

$$\delta = c_f \frac{T_b - T_u}{T^0 - T_u} l_F \tag{2.4}$$

$$l_F = \frac{\left(\lambda / c_p\right)\Big|_{T^0}}{\rho_u S_L} \tag{2.5}$$

$$\lambda / c_p = 2.58 \times 10^{-5} \left(T / 298\ K\right)^{0.7}\ kg/m-s \tag{2.6}$$

The HCT results and burning velocity correlations for the reaction fronts developed from the HCT simulations were compared to the burning velocity correlations of Müller et al. [22] and Metghalchi and Keck [18], and to the atmospheric, stretch corrected laminar burning velocity experiments of Davis and Law and Kumar et al. at pre-heat temperatures of 298 K in Figure 2.5 (left) and 470 K in Figure 2.5 (right). The HCT predicted burning velocities, and the laminar burning velocity correlation predictions from HCT and Müller et al. all show good agreement with the experimental data, even in the rich regions where the mechanism and correlations were not developed. In addition, good agreement between the experimental data and the Metghalchi and Keck power law is observed for the T_u = 298 K case, with a slight under-prediction of burning velocity by the power law at 470 K.

Experimental, stretch corrected laminar burning velocity data at 1 to 25 bar from the isobaric bomb studies of Bradley et al. [20] and Jerzenbeck et al. [17] was compared against the HCT simulation burning velocities and their correlations, the burning velocity correlations of Müller et al. [22] and Metghalchi and Keck [18] for Φ = 0.8, Figure 2.6 (left) and Φ =1.0, Figure 2.6 (right). Good agreement is demonstrated between the experiments, the HCT simulations and their correlation, Equations (2.1) through (2.3), and the correlation of Müller et al. Reasonable predictions are also provided by the

power law, however, significant under-prediction of the burning velocity is noted at low pressures, while significant over-prediction occurs at the higher pressures. The step change at 10 bar is due to a jump in T_u from 358 K in Bradley et al. experiments to 373 K in those of Jerzenbeck et al.

The equivalence ratio sweep shown in Figure 2.7 (left) at T_u = 900 K, 40 bar, includes predictions within the ultra-lean, high pressure, high T_u conditions characteristic of SACI combustion. The HCT simulations predict viable, steady burning velocities for Φ as lean as 0.4, while extrapolation of the HCT burning velocity correlations, Equations (2.1) through (2.3), show finite burning velocities to $\Phi \sim 0.2$. In addition, the predictions made with the Müller et al. [22] and Metghalchi and Keck [18] correlations are extrapolations under the conditions in this figure. As expected, the laminar burning velocity predictions from the HCT correlation using Equations (2.1) through (2.3) show the best agreement with the HCT simulation results. In particular, while the Müller et al. correlation shows trend-wise agreement with the HCT simulations, the agreement worsens as Φ is decreased, while noting that at a Φ = 0.4, significant extrapolation of the Müller burning velocity correlation is required to arrive at the predicted 5 cm/s burning velocity shown in the figure. This burning velocity is significantly lower than the 20 cm/s from the HCT predictions and correlations at the same Φ. In addition, while good performance is noted for the power law relative to the HCT simulations at moderately lean and stoichiometric conditions, a significant divergence in burning velocity is noted as Φ approaches the lean limit, which is predicted as a constant Φ = 0.57 by the mathematical form of the power law. While predictions at ultra lean Φ with the power law also represent a significant extrapolation from the range of the initial fit data, the predicted lean limit is significantly richer than that of the HCT simulation trend and those reported for SACI engine experiments [1].

Laminar burning velocity iso-lines of 10, 30, 60 and 100 cm/s from the HCT simulation and correlation are shown as a function of T_u-T_b at 40 bar in Figure 2.7 (right).

It can be seen in the figure that the correlation is extrapolated for a portion of the 10 cm/s iso-line, as steady reaction fronts were not obtained under a Φ = 0.4 for this iso-line. At constant T_b, the significant increases in S_L that occur with decreasing Φ and increasing T_u are notable. The negative slope of the S_L iso-lines shows that a constant S_L can be maintained at low Φ-T_b operation through the elevation of T_u. Similar behavior is observed when using the Müller et al. S_L correlation. To eliminate the variable density effects associated with varying T_u, the data are recast in terms of mass burning flux iso-lines, $f^0 = \rho_u S_L$, which are shown in Figure 2.8 (left). This figure has a similar trend-wise behavior to Figure 2.7 (right), and while the slopes of the iso-lines in Figure 2.8 (left) are somewhat reduced, it is apparent that the effect of variable density is not the only cause for the behavior shown in Figure 2.7 (right). This behavior marks an interesting departure from the typically observed dominance of S_L by T_b at a constant pressure [45], perhaps made evident by the extended range of this study. While the root cause of this behavior was not determined, it appears to result from the modification of the reactive-diffusive balance within the reaction front. Speculating with regard to potential chemical effects on the behavior of S_L at constant T_b, the rate of the $H + O_2 \leftrightarrow OH + O$ chain branching reaction will be affected by the increased oxygen concentration in air dilute systems, which may enhance the supply of OH to the main heat release reaction $CO + OH \leftrightarrow CO_2 + H$, which would in turn increase both heat release rates and mass burning fluxes. In addition, the increases in burning velocity could also be associated with increases in the species mass diffusion and thermal conductivity coefficients with temperature [45].

The reaction front thickness contours plotted in Figure 2.8 (right) also show a slightly negative slope. Therefore, for a constant burned gas temperature, a slight reduction in flame thickness may occur as one shifts to the right towards leaner mixtures with higher pre-heat temperatures. The importance of the flame thickness to the flamelet concept is discussed further in Chapter 3.

While transient reaction fronts with finite laminar burning velocities could be established under most conditions with T_b around 1500 K and above, the process of obtaining steady reaction fronts under conditions with high T_u, high pressure and low Φ was challenging. To understand why, the timescales of reaction front propagation, τ_F, were compared to the ignition delay of the end-gas, τ_{ID}, where the ratio τ_{ID}/τ_F, is plotted in the T_u- T_b domain, again at 40 bar as shown in Figure 2.9. The ignition delay was calculated using the unburned gas conditions in the iso-octane ignition delay correlation of He et al. [6], while the reaction front time was defined as the time required for the front to traverse one front width, which was calculated with the correlated reaction front thickness and laminar burning velocity, where $\tau_F = \delta/S_L$. To reach steady burning velocities, it was noted that the reaction fronts typically required at least 8-10 front thicknesses of travel from their initial profile. Within the lower right hand portion of the domain where viable reaction fronts were anticipated, but steady front data was lacking (T_u ~ 900-1000 K, T_b ~ 1500 - 1600 K), the reaction front times are on the order of one tenth of the end-gas ignition delay, meaning that the front can travel approximately 10 front thicknesses during the ignition delay. The lack of steady reaction front data in the lower right hand portion of Figure 2.9 therefore is likely due to the fact that the ignition delay time and the time required by the front to achieve steady propagation are comparable, and as a result the front may not have sufficient time to adjust to a steady configuration prior to auto-ignition. In contrast, while chemistry is fast and ignition delays short within the upper right hand portion of the diagram (T_u ~ 1000 K, T_b ~ 2400 K), the front times are reduced, such that the front travels roughly 100 thicknesses during the ignition delay period, allowing ample time for adjustment to a steady configuration. The broadening in the range of steady reaction fronts with decreasing pressure can also be partially explained by these results, given that ignition delay increases as pressure decreases.

Because the front times observed for the steady flames are significantly shorter than the ignition delay, it is reasonable to conclude that these propagating fronts are essentially deflagrations, because if these fronts were ignition waves, then the corresponding front times would be on the order of the ignition delay, a behavior that is not observed in Figure 2.9. These results also suggest that the experimental determination of steady burning velocity and other front data within the SACI regime will be challenging, given that the timescales of the front are only one to several orders greater than the ignition delay within the SACI regime.

These timescales also have practical implications to SACI combustion, where load is often controlled through Φ. The contribution of the reaction front to the overall energy release will be marginal for operation in the lower right hand corner of the data within of the T_u- T_b domain of Figure 2.9, i.e. where $\tau_{ID} / \tau_F <\sim 10$. For operation with elevated equivalence ratio ($\Phi > 0.4$), the reaction front times become short relative to the ignition delay and the fronts can travel a significant distance prior to the end of the ignition delay. As Φ is reduced to lower load however, auto-ignition becomes the more dominant combustion mode as the deflagration portion of combustion contributes less to the overall heat release event, given the increased front time relative to the ignition delay. This observation reinforces previous conclusions [1] which suggest that homogeneous SACI combustion is most effective under medium and high load operating conditions, where Φ's are elevated.

2.4 The Propagation of Reaction Fronts into Auto-Igniting End-Gases: Background

The steady reaction front study in Section 2.3 was performed with many cases having pre-heat temperatures in proximity to the ignition temperature of the iso-octane air mixture. From images of SACI combustion [23-25], reaction front propagation appears to continue even as the end-gas upstream of the front auto-ignites; the behavior of the

front and its significance to the overall combustion process during this time are not well understood. In order to improve upon the understanding of this behavior and to support its modeling within KIVA-3V, the propagation of reaction fronts into end-gasses with varying levels of reaction progress was examined with both steady flow reactor and transient one dimensional simulations.

As mentioned previously, reaction front expansion speeds ranging from 2–5 m/s have been observed by Zigler [25], while Persson et al. [23] have reported expansion speeds from approximately 0.5-10 m/s during the initial deflagration phase of SACI combustion. Reaction front-like structures attributable either to turbulent flames or burned gas expansion, with expansion speeds ranging from 5 to 30 m/s, have been observed in proximity to HCCI ignition kernels by Hultqvist et al. during the late stages of HCCI combustion [46]. Schiessl et al. have also recorded mean expansion speeds around the ignition kernels in the knocking end-gas of an SI engine [47], where apparent mean reaction front expansion speeds were on the order of 25 m/s with a standard deviation of 16 m/s. Additional studies by König et al. in a knocking SI engine showed reaction fronts propagating away from end-gas ignition kernels with apparent flame speeds ranging from 6 to 9 m/s, while the main flame front was observed to propagate at 10.3 to 12.5 m/s [48].

The wide range of burning velocities within the above studies suggests that reaction fronts propagating into inert and reacting end-gases may be within entirely different subsonic premixed combustion regimes, which in turn are governed by differing physical phenomena. For reaction fronts propagating in premixed mixtures, two subsonic combustion regimes have been proposed by Zel'dovich [49]. In the normal deflagration regime, the reaction front's propagation rate is characterized by the laminar flame speed, and front propagation is governed by the diffusive reactive balance within the reaction zone of the flame. Within the spontaneous ignition front regime however, the front is nothing more than a cascade of ignition events within a pre-existing temperature gradient

that gives the appearance of front propagation. The apparent propagation rate of these fronts is typically much greater than that of the laminar flame speed.

A variety of computational studies have examined reaction front propagation during end-gas ignition. Significant reaction front acceleration was observed during end-gas ignition in the work of Pitz and Westbrook [50]; this work also showed that the presence of the reaction front did not directly affect the ignition delay of the end-gas. More recent studies have focused on classifying the combustion regime of the front. For example, Gu et al. characterized the front's combustion regime with its temperature gradient [51], while direct numerical simulation studies have characterized the front's combustion regime by comparing planar burning velocity predictions from PREMIX to the front propagation speed from DNS [52, 53]. In addition, Bansal and Im have also developed a Damköhler number based criteria for separating combustion regimes in stratified mixtures [54].

The above studies rely upon detailed spatial information to assess the combustion regime of the reaction front. This information is not currently available within simulations such as KIVA-3V, which relies upon sub-grid models for the simulation of reaction front propagation. Many KIVA-3V and RANS knock modeling approaches have assumed that computational cells are consumed either by the reaction front propagation or by homogeneous ignition [55-57], while more recent work has used a Damköhler number as a criterion to switch between flame and homogeneous reactor models at the onset of and during knock [57]. The results of these simulations have shown significant dependence to the magnitude of the Damköhler number used to transition between combustion models. In addition, limited fundamental data is available for the development and validation of these models. As a result, indirect methods such as the comparison of the modeled and experimental cylinder pressure traces are often used for the purposes of model validation.

To improve upon the modeling of reaction fronts during SACI combustion, a series of model problems are used to investigate the key physical processes governing reaction front propagation into end-gases with varying levels of reaction progress. New techniques are developed to identify the combustion regime of the reaction front, while further insight is provided into the importance of these fronts to the reactant mass entrainment process occurring within the cylinder during auto-ignition.

2.5 The Steady Propagation of Reaction Fronts into Auto-Igniting End-Gases Within a Flow Reactor

In this section, PREMIX and SENKIN are used as a model problem for a reaction front propagating into an end-gas just prior to and during auto-ignition, representing the quasi-steady evolution of a single laminar reaction front within a turbulent flame.

The homogeneous ignition of mixtures at thermal conditions representative of the end-gas of an air-dilute SACI or HCCI engine at TDC was simulated with SENKIN. Four homogeneous reactor simulations for Φ = 0.45 at a constant pressure of 20 atmospheres were performed at initial temperatures, T_u, of 600, 700, 800 and 900 K. Constant pressure combustion of these mixtures yields adiabatic flame temperatures, T_b, of 1658, 1742, 1829 and 1918 K respectively.

The SENKIN homogeneous ignition calculations provide the temperature and composition for an end-gas with reaction progress ranging from zero to unity. In turn, these mixtures are used as the upstream boundary condition for the PREMIX flow reactor, where the PREMIX flow reactor inlet temperature, T_{in}, and its associated composition are obtained from a single time/reaction progress within the SENKIN solution. In this study, T_{in} ranged from $T_{in} = T_u$ for a case with no inlet reaction progress, up to T_{in} = 1100 K, representative of a case with significant end-gas reaction progress. T_{in} was varied in increments of 25-100 K, and for each T_{in} and T_u, a reaction progress variable, c, is defined where $c = (T_{in} - T_u)/(T_b - T_u)$. For the range of T_{in} studied, 600 to

1100 K in this work, the reaction progress at the inlet of the PREMIX reactor, c, varied from 0.0 to 0.473, depending on T_u. For a given T_u, varying the PREMIX reactor inlet temperature, T_{in}, is representative of the quasi-steady evolution of the reaction front as it propagates into an auto-igniting end-gas at varying levels of end-gas reaction progress. Given that the mass burning flux, $\dot{m}''$, within PREMIX is constant, the reaction front speed, S_{front}, is obtained from $S_{front} = \dot{m}'' / \rho_u$, where ρ_u is the initial density within the SENKIN reactor. Figure 2.10 shows the spatial temperature profiles (left) and heat release rates (right) within the PREMIX domains for different c - T_{in} corresponding to T_u = 900 K, T_b = 1918 K. For the c = 0, T_{in} = 900 K case, the end-gas lacks a temperature gradient upstream of the front because the incoming mixture's reactivity `is negligible, which is typical of reaction front propagation within the normal deflagration regime. As the reaction progress of the mixture entering the PREMIX reactor increases, a noticeable temperature gradient develops upstream of the front. In addition, the maximum temperature gradient within the front is observed to decrease with c and T_{in}, consistent with the combustion regime transition behavior noted by Gu et al. [51] and Sankaran et al. [52].

Figure 2.11 (left) shows S_{front} as a function of T_{in}, where each solid line corresponds to a given T_u at varying levels of c and T_{in}. The dashed line, for mixtures with zero incoming reaction progress (T_{in} = T_u), shows the thermal effect of T_u on the front's burning velocity. It is apparent that for inlet temperatures up to approximately 950 K, that the increases in front speed with T_{in} is slight and trend wise similar to the increases obtained through pre-heating only (the dashed line). In addition, all of the solid lines are located below the dashed line, suggesting that fronts with T_{in} up to 950 K are essentially deflagrations. However, as T_{in} is increased beyond 1000 K, a substantial increase in front speed occurs with additional inlet pre-heating, showing that the speed of the reaction front is a strong function of the upstream reaction progress, suggesting that the front may be within the spontaneous ignition front regime.

To understand the physical mechanisms governing the front propagation discussed above, the spatial coordinate system in Figure 2.10 (left) is transformed to a time based one, where the time coordinate is determined from the incremental times required for a Lagrangian particle to traverse the PREMIX cell, using the velocity and cell thicknesses from the PREMIX solution [58]. The resulting PREMIX temperature time histories are shown in Figure 2.11 (right) as solid lines, while the dashed lines in Figure 2.11 (right) are for the corresponding time dependent homogeneous ignition solutions from SENKIN, starting at the same initial condition as those in the PREMIX solution. For the various levels of inlet reaction progress shown in Figure 2.11 (right), it is apparent for the $T_{in} = 900$ K case that the PREMIX solution achieves chemical equilibrium much earlier than the corresponding SENKIN solution. This advance occurs because of the integral role that transport plays in the energy transfers within the reaction front of the PREMIX solution, where the species and energy transported upstream from the reaction zone lead to earlier reaction. This suggests that the fronts with $T_{in} = 900$ K are normal deflagrations. For $T_{in} \approx 1000$ K and beyond, however, the PREMIX and SENKIN solutions are nearly identical, suggesting that the evolution of the reaction front is dictated primarily by chemistry, indicating that a transition from the normal deflagration to the spontaneous ignition front regime occurs around the $T_{in} = 1000$ K case.

To quantify the combustion regimes present in Figure 2.11 (right) two characteristic timescales are developed from the reaction front and homogeneous ignition solutions, τ_{Flame} and τ_{Chem}, respectively. These time scales are defined as the corresponding time from the conditions at the inlet of the PREMIX reactor, for both SENKIN and PREMIX solutions, to the appropriate times where the mixture temperature reaches 99% of T_b. The ratio τ_{Flame}/τ_{Chem} therefore ideally ranges from 0 to 1 and is indicative of the relative importance of transport within the reaction front. As τ_{Flame}/τ_{Chem} approaches 0, the front is in the normal deflagration regime as τ_{Flame} is much smaller than

τ_{Chem} because of the balance between reaction and diffusion within the reaction zone of the flame. On the other hand, when $\tau_{Flame}/\tau_{Chem} \approx 1$, the effect of transport is minimal and the combustion process occurs in a chemically dominated fashion. At intermediate values of τ_{Flame}/τ_{Chem}, combustion occurs in a mixed mode between the two regimes.

The reaction front speed S_{front} is shown as a function of τ_{Flame}/τ_{Chem} in Figure 2.12 (left). From the figure, the front speeds remain relatively flat for τ_{Flame}/τ_{Chem} up to 0.95, suggesting that the reaction front is deflagration-like. Beyond τ_{Flame}/τ_{Chem} of 0.95, a rapid increase in the front speed is noted as the end-gas reaction progress becomes substantial and combustion within the front becomes chemically dominated.

Figure 2.12 (right) shows that the front's maximum temperature gradient rapidly diminishes as the combustion within the front becomes chemically dominated, that is when τ_{Flame}/τ_{Chem} exceeds 0.95. As τ_{Flame}/τ_{Chem} transitions from 0.95 to values near 1.0, the maximum temperature gradient of the reaction front ranges from approximately 1000 to 10000 K/mm. For $\tau_{Flame}/\tau_{Chem} < 0.95$, a wide range of maximum temperature gradients are also observed within the front, however the sensitivity of the maximum temperature gradient to τ_{Flame}/τ_{Chem} is not as pronounced. Given the wide range of maximum temperature gradients observed within the chemically dominated regime of front propagation ($\tau_{Flame}/\tau_{Chem} \geq 0.95$), it is anticipated that the maximum temperature gradient can only serve as an approximate indicator of the front's combustion regime.

From Figure 2.10 (left), it is apparent that the reaction front is positioned to the right of the PREMIX reactor inlet. Therefore, referencing the above results to variables such as T_{in} only provides a linkage to the PREMIX reactor inlet conditions and not to the front itself. The reaction front-base temperature, T_{front} is used to separate the front from the end-gas, where T_{front} is defined as the initial PREMIX temperature where the PREMIX and SENKIN solution temperatures differ by more than 1%, at equivalent solution times. This temperature departure provides a measure of where transport effects begin to influence the evolution of the reaction front. Figure 2.13 shows T_{front} with

respect to τ_{Flame}/τ_{Chem}. For deflagration waves, it is apparent that T_{front} is comparable to T_{in}. At $\tau_{Flame}/\tau_{Chem} \approx 0.95$, effectively the start of the spontaneous ignition front regime in these simulations, T_{front} is approximately 1100 K. These results suggest that T_{front} can be used as a metric for transitioning between the normal deflagration and spontaneous ignition front combustion regimes, where for $T_{front} < 1100$ K, the reaction front is essentially a normal deflagration, which has been shown in this work to be relatively insensitive to the degree of upstream reaction progress. Beyond 1100 K however, reaction front propagation is mostly a function of the end-gas reaction progress, as the front is essentially an ignition cascade beginning within the upstream mixture.

2.6 The Unsteady Propagation of Reaction Fronts into Auto-Igniting End-gases

In the previous section, the propagation of steady reaction fronts into auto-igniting end gases was examined. The structure of the fronts in that section may not be completely representative of a front within an engine environment, given the spatially dependent residence times of the mixture within the flow reactor. This variation in residence times leads to the thickened reaction front structure for the reacting end-gas cases shown in Figure 2.10 (left). In the current study, the transient propagation of a premixed, one-dimensional reaction front into an auto-igniting end-gas mixture is simulated under SACI conditions using HCT. The evolution of the front's burning velocity, temperature gradient and structure are analyzed in order to better understand the physical mechanisms present within the front during the SACI combustion process.

The configuration of the model problem within the current study is similar to that of Pitz and Westbrook [50], where the reaction front propagates towards the closed end of a tube, while the other end of the tube is open. In addition, the domain pressure is maintained constant in order to remove system compression heating effects and minor local pressure variations imposed by the energy release.

Runs were performed with equivalence ratio, pressure, unburned and the resulting adiabatic flame temperatures, T_b, selected to be relevant to SACI combustion, as shown in Table 2.5. The initial unburned conditions of the baseline case, Case 4, were selected to approximate the state in proximity to the spark ignition event in the optical engine images of SACI combustion by Zigler [25]. This state corresponds to a pressure, p, of 17.4 bar, an initial end-gas temperature, T_u, of 907.7 K and Φ of 0.45, with zero initial reaction progress. For Case 4, the reaction front was initially located 1.3 cm into the domain in order to prevent the entire end-gas from being consumed by the front, while an overall domain length of 1.5 cm was chosen to provide sufficient room to accommodate the initial reaction front profile. Using the same steadiness criteria described in Section 2.3, all of the reaction fronts shown in Table 2.5 initially achieved steady burning velocities prior to the ignition of the end-gas.

Figure 2.14 (left) shows the evolution of the domain's temperature profiles at select times for Case 4. For the first 16 ms of the simulation, the reaction front is noted to travel from the right to the left of the domain, where modest upstream heat release is responsible for the gradual increase in the end-gas temperature. The burning velocity of the front changes little during the first 16 ms of travel, given the near uniform front movement in time shown in the figure. Beyond 1100 K (20.6 ms), the end-gas achieves thermal runaway, while by 20.9 ms end-gas auto-ignition is completed. Due to the increase in the temperature and specific volume of the end-gas beyond end-gas temperatures ($T_{E.G.}$) of 1100 K, the front is displaced to the right of the domain.

Figure 2.14 (right) shows the time based evolution of the end-gas temperature, the maximum temperature gradient within the reaction front and front's burning velocity from 16 to 25 ms. For the initial 2 ms of the simulation, not shown in the figure, the reaction front attains a steady burning velocity on the order of 44 cm/s with a maximum temperature gradient of 22185 K/mm, while the end-gas temperature remains at the initial temperature of 907.7 K. From 16 to approximately 20.6 ms, the end-gas temperature

rises slowly due to heat release, while the front speed increases and the maximum temperature gradient within the front gradually diminishes. Beginning around an end-gas temperature of 1100 K (20.6 ms), the burning velocity and the front's maximum temperature gradient rapidly evolve. By 1800 K (20.8 ms), the burning velocity is on the order of 415 cm/s, increasing by nearly a factor of ten over the initial steady value, while the peak temperature gradient within the front reaches 1240 K/mm, a roughly twenty-fold decrease.

The detailed structure of the Case 4 reaction front is shown in Figure 2.15. This figure includes the front's temperature profile and the normalized spatial rates of sensible energy change due to reaction and heat conduction for end-gas temperatures of 907.7 K (4.0 ms), 1199.8 K (20.7 ms), 1401.5 K (20.8 ms) and 1598.6 K (20.8 ms). For each of these end-gas temperatures, the domain's peak heat release rate is observed to consistently occur at the location where the temperature is approximately 1600 K, which is the approximate temperature where CO to CO_2 conversion becomes prominent for iso-octane air mixtures during HCCI combustion [2]. At $T_{E.G.}$ = 907.7 K (4.0 ms), Figure 2.15 (top left), the front structure is similar to that of a deflagration, where a clear transition is noted between the nearly chemically inert pre-heat zone and the reaction zone within the front. In addition, the absolute magnitudes of the rates of energy change due to heat conduction and heat release are similar.

Figure 2.15 (top right), coincides with the time when significant increases in the burning velocity are noted in Figure 2.14 (right), at $T_{E.G.}$ = 1199.8 K (20.7 ms). From the figure, low but non-negligible levels of end-gas heat release appear upstream of the front. Also from the figure, it is apparent that the overall thickness of the reaction front is little changed between 907.7 K (4.0 ms) and 1199.8 K (20.7 ms). As a result, the maximum temperature gradient within the front must decrease with end-gas reaction progress given that the temperature difference between the end and burned gasses decreases with auto-ignition while front thickness remains nearly constant. The lower peak rates of energy

change due to heat conduction observed in Figure 2.15 (top right) with auto-ignition correspond to the reduction in the maximum temperature gradient within the front. In addition, the peak heat release rate within the front is observed to diminish slightly as the upstream reactants are consumed by auto-ignition. Overall, the front's structure remains deflagration-like given the continued importance of heat conduction to energy transfer within the front. Similar behavior is observed for the front at $T_{E.G.}$ = 1401.5 K, Figure 2.15 (lower left).

By $T_{E.G.}$ = 1598.6 K in Figure 2.15 (lower right), the peak temperature gradients within the front are noticeably reduced. The temperature difference between the end and burned gasses is now approximately 300 K and heat conduction is observed to play a minor role to the rate of energy change within the front. In addition, the heat release has lost its peaked profile, as $T_{E.G.}$ is nearly 1600 K and the end-gas reaction rates are now comparable to the peak values within the front. The end gas heat release rates for Case 4 peak around an end-gas temperature of 1620 K.

The behavior of Case 4 in Figure 2.15 (lower right) suggests that combustion becomes chemically controlled around an end-gas temperature of 1600 K. In the normal deflagration regime, the burning velocity of the front is expected to be sensitive to variations in the magnitude of the transport coefficients, while within the spontaneous ignition front regime the burning velocity should be insensitive to these changes. To examine the combustion regime of the reaction front, Figure 2.16 shows the results of a parametric study that varied the magnitudes of the transport coefficients in proximity to the end-gas temperatures where heat conduction effects were shown to be minimal in Figure 2.15. The simulations in Figure 2.16 began with the base transport coefficients used in Figure 2.14 through Figure 2.15. Upon reaching the end-gas temperature indicated in Figure 2.16 (1200-1600 K as shown), the magnitude of the mass diffusion and thermal conductivity coefficients were multiplied by factors of 0.25, 0.50, and 0.75 throughout the computational domain. Results with zero and near zero factors had slight

numerical instabilities and are not shown. In addition, the burning velocities shown in Figure 2.16 are for end-gas temperatures up to roughly 100 K below the adiabatic flame temperature because of difficulty experienced in calculating stable burning velocities towards the end of the end-gas combustion event.

The reduction in the laminar burning velocity with the multiplication of the transport coefficients by factors of 0.25 and 0.50 is clear for $T_{E.G.}$ = 1200 K (upper left), 1400 K (upper right) and 1500 K (lower left) in Figure 2.16. When the transport coefficients for these cases are scaled by factors of 0.25, it is interesting to note that the burning velocities remain elevated and do not trend towards zero, suggesting that the timescales of the front propagation are approaching those of an ignition front, while at the same time it is obvious that transport effects are clearly non-negligible. In Figure 2.16 (lower right), where the end-gas temperature is near 1600 K, the burning velocity shows minimal sensitivity to the magnitude of the transport coefficients.

From the above results for Case 4 in Figure 2.15, heat conduction was shown to influence the energy transfers within the front for $T_{E.G.}$ below 1600 K, while in Figure 2.16 the burning velocity of the front is shown to be sensitive to modifications of the transport coefficients for $T_{E.G.}$ below 1600 K, behaviors characteristic of a reaction front within the normal deflagration regime. Beyond 1600 K, however, the burning velocity of the front is relatively insensitive to the transport coefficient magnitudes, while heat conduction is shown to be almost completely negligible, which is characteristic of a front within the chemically controlled, spontaneous ignition front regime [49, 51], where the thermal and compositional gradients within the front are low in order to minimize the effect of transport [51]. Cases 2-9 in Table 2.5 showed similar tendencies, where the rate of energy change within the front due to heat conduction becomes marginal once $T_{E.G.}$ ranges from 1600 to 1800 K.

Figure 2.17 (left) shows the ability of the laminar burning velocity correlation to capture the simulated burning velocity for a range of conditions in Table 2.5, where the

solid lines in the figure are results from the transient HCT simulations and the dashed lines are the burning velocity correlation predictions from Equations (2.1) through (2.3) with the fuel mass fraction left at its initial, unburned value throughout the run. In the figure, select predictions from the burning velocity correlation are omitted for clarity. It is clear that the correlation performs reasonably well for end-gas temperatures up to 1100 K. Beyond this temperature the correlation over-predicts the burning velocity of the front.

Given the poor ability of Equation (2.1) through (2.3) to fit the burning velocity beyond 1100 K, the importance of the reaction front to the consumption of the reactant mixture during end-gas auto-ignition is evaluated by transforming the domain's coordinate system from a spatial to mass per unit area based system by integrating from the origin to the right hand boundary of a given computational cell with Equation (2.7).

$$m(x) = \int_0^x \rho dx \tag{2.7}$$

The results of this integration for Case 4 at select times are shown in Figure 2.17 (right). It is clear that for end-gas temperatures up to 1100 K (20.6 ms) that the reaction front dominates the consumption of the end-gas reactants. However, beyond an end-gas temperature of 1100 K, the reaction front plays a relatively minor role in the end-gas consumption process relative to auto-ignition, as the front's movement in the mass space is limited. By an end-gas temperature of 1600 K, where combustion was shown to be chemically dominated, the movement of the front in mass space is trivial. The minor changes in the left endpoint of the mass domain result from a volume decrease within the domain's first cell due to grid rezoning and also result from the density reduction within the cell during auto-ignition.

Equation (2.8) is used to calculate the mass per unit area entrained by the reaction front as a function of time, m_{ent}, for the majority of the conditions shown in Table 2.5:

$$m_{ent} = \int_{t=0}^{t} \rho_u S_{Front} dt \tag{2.8}$$

The results in Figure 2.18 (left) for various Φ and Figure 2.18 (right) for various p and T_u using Equation (2.8) show that a significant mass of reactants are consumed by the reaction front up to end-gas temperatures of approximately 1100 K. Beyond 1100 K however, the mass entrained by the reaction front is clearly marginal.

This end-gas temperature of 1100 K is in proximity to the temperature where the high temperature chain branching reaction H + O_2 ↔ O + OH becomes significant [45, 59, 60]. It is similar to the temperature at the front base in Section 2.5 where front propagation becomes chemically dominated [61], the temperature observed by Kelly-Zion and Dec [60] where combustion becomes rapid in HCCI, and is in line with the ignition temperature for high temperature systems discussed by Westbrook [59]. Even though elevated burning velocities are observed during auto-ignition for Case 4, the limited reactant mass entrained by the front beyond 1100 K is a result of the limited time available for front propagation once the end-gas chemistry becomes fast. While transport effects are non-negligible until the end-gas temperature ranges from 1600-1800 K, the importance of transport diminishes with auto-ignition, which further limits the reactant mass entrained by the front. As a result, the amount of mass entrained by the front in Figure 2.18 may be slightly overstated once combustion within the front becomes chemically dominated ($T_{E.G.}$ > 1600 K for Case 4), as ignition fronts only give the appearance of propagation as they sequentially auto-ignite through a temperature gradient.

2.7 Conclusions

The need for iso-octane air laminar reaction front data within the highly dilute, high pressure and pre-heat temperature conditions of the SACI combustion regime has

been addressed by this work. Steady premixed laminar reaction fronts were simulated with Φ, T_u and pressure ranging from 0.1 to 1.0, 298 to 1000 K and 1 to 250 bar, respectively, conditions relevant to both the SI and SACI combustion regimes, extending upon earlier studies [18, 22] which were focused primarily on the SI combustion regime.

In general, it was shown that with the elevated pre-heat temperatures of HCCI and SACI combustion, that reaction front propagation with moderate burning velocities could be supported at equivalence ratios characteristic of mid and high load HCCI combustion. At a given T_b, it was also shown that burning velocities increased when moving from the SI to the SACI combustion regime. In addition, steady reaction fronts with burning velocities in excess of 5 cm/s could not be established when T_b was below 1500 K. While viable transient reaction fronts were predicted under the low Φ - high T_u conditions relevant to SACI combustion, timescale analysis showed that the difficulty in producing steady reaction fronts under these conditions resulted from the lack of time available for the front to achieve steady propagation prior to auto-ignition. Correlations of steady flame burning velocity and thickness were subsequently developed. Under SI combustion conditions, the HCT simulated reaction fronts and burning velocity correlation showed good agreement with both atmospheric and high pressure laminar flame data and the correlation of Müller et al. [22]. Under simulated SACI conditions, the laminar burning velocity correlations provide excellent agreement with the current dataset, versus the trend-wise agreement shown by extrapolating the Müller et al. correlation. It was also demonstrated that SACI combustion should be most useful at medium and high engine loads, due to the moderate laminar burning velocities for these conditions.

Given the proximity of the above steady reaction front simulations to ignition conditions, steady flow reactor simulations were performed to examine the combustion regime of reaction fronts propagating into conditions with elevated pre-heat temperatures. The front's combustion regime was characterized using a ratio of the flame and

homogeneous ignition timescales, while an additional metric, the reaction front base temperature, was developed to separate the transport affected solution of the reaction front from that of the chemically controlled end-gas. When the timescale ratio was below 0.95, moderate changes in the reaction front burning velocity and thickness occurred with variation in the timescale ratio, suggesting that reactions fronts behave in a deflagrative manner under these conditions. Beyond a timescale ratio of 0.95 however, significant increases in burning velocity and decreases in front thickness occurred, suggesting chemically dominated front propagation. At a timescale ratio of 0.95, the front base temperature was approximately 1100 K, suggesting that this temperature can be used as an end-gas temperature marker for the transition to chemically dominated front propagation.

Additional unsteady reaction front propagation studies were performed under conditions relevant to SACI combustion. Early in the simulations, the reaction front was shown to propagate as a deflagration, where peak absolute heat conduction and reaction rates within the front were of similar magnitude. Heat conduction was shown to be non-negligible to the energy transfers within the front until the end-gas achieved high levels of reaction progress. As end-gas reaction progress proceeded, the peak temperature gradient within the front diminished until reaching a point where heat conduction effects were negligible, typically for end-gas temperatures between 1600 and 1800 K under the conditions examined. A parametric study examining the magnitude of the species mass diffusion and heat conduction coefficients confirmed the transition to chemically dominated combustion around these end-gas temperatures. It was shown that the burning velocity correlation could reasonably reproduce the transient simulation results as long as end-gas temperatures did not exceed 1100 K. While significant reaction front acceleration was noted beyond these temperatures, the contribution of the front to the overall heat release was shown to be minimal, given the limited reactant mass consumed by the front because of the rapid end-gas chemistry.

Table 2.1: Previous high pressure iso-octane air laminar burning velocity studies.

Authors	Φ	**Pressure**	T_u **(K)**
Ryan and Lestz (1980) [19]	0.7 - 1.3	4 - 18 atm	470 - 600
Metghalchi and Keck (1982) [18]	0.8 - 1.5	0.4 - 50 atm	298 - 700
Bradley et al. (1998) [20]	0.8 - 1.0	1 - 10 bar	358 - 450
Jerzembeck et al. (2009) [17]	0.7 - 1.2	10 - 25 bar	373
Göttgens et al. (1992) [21]	0.3 – 1.0	1 - 40 bar	298 - 800
Müller et al. (1997) [22]	0.6 – 1.0	1 - 40 bar	298 - 800

Table 2.2: The range of conditions for the steady laminar reaction fronts simulations.

Φ	0.1	0.2	0.3	0.4	0.5	0.6	0.7	0.8	0.9	1.0	
T_u **(K)**	298	400	600	800	900	950	1000				
P **(bar)**	1.0	2.5	5.0	10.0	15.0	25.0	40.0	60.0	100.0	160.0	250.0

Table 2.3: Fit parameters for the laminar burning velocity and inner layer temperature expressions, Equations (2.1) and (2.2).

F **(cm/s)**	***M***	***G*** **(K)**	***n***	***B*** **[bar]**	***E*** **(K)**
280583	2.0837	-1375.3	4.9991	2.52E+10	81006

C_7	C_8	C_9	a_1	a_2	a_3
0.01599	0.4539	0.3218	0.72	-1.1	0.1

Table 2.4: Fit parameters for the adiabatic flame temperature, Equation (2.3).

c	***d***	***e***	***f***	***g***
2638.1	194.6	-773.045	-0.34968	0.3432

Table 2.5: The conditions examined within the transient reaction front study.

Case	1	2	3	4	5	6	7	8	9
$\boldsymbol{\Phi}$	0.30	0.35	0.40	0.45	0.50	0.45	0.45	0.45	0.45
$\boldsymbol{T_u}$ **(K)**	907.7	907.7	907.7	907.7	907.7	950	1000	907.7	907.7
$\boldsymbol{T_b}$ **(K)**	1617	1723	1825	1925	2020	1962	2007	1925	1926
p **(bar)**	17.4	17.4	17.4	17.4	17.4	17.4	17.4	50	100

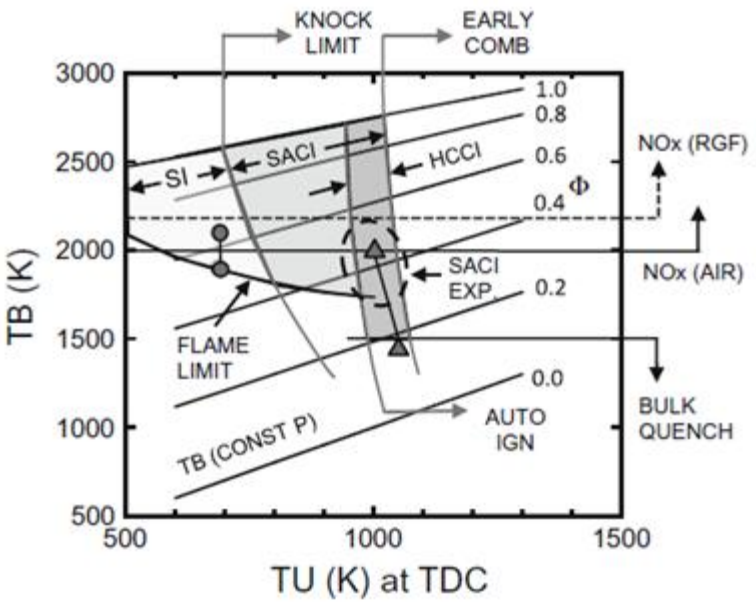

Figure 2.1: Multi-mode combustion diagram with the SI, SACI and HCCI combustion regimes [1].

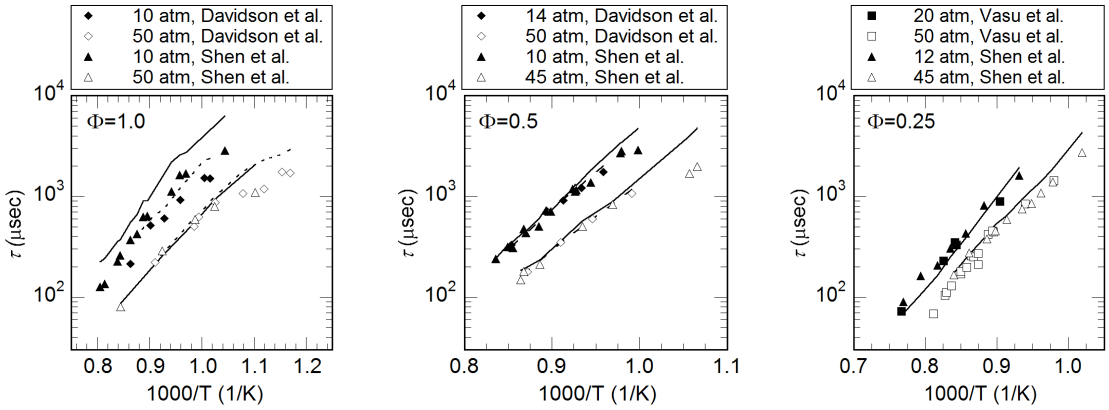

Figure 2.2: Ignition delays for iso-octane air mixtures at Φ = 1.0 (left), Φ = 0.5 (middle) and Φ = 0.25 (right). Experimental data [40-42] at high pressure (open symbols) and low pressure (filled symbols). Solid lines are simulations initialized at the post-shock initial conditions from Shen et al. [42], while the dashed lines are simulations initialized at the post-shock initial conditions from Davidson et al. [40].

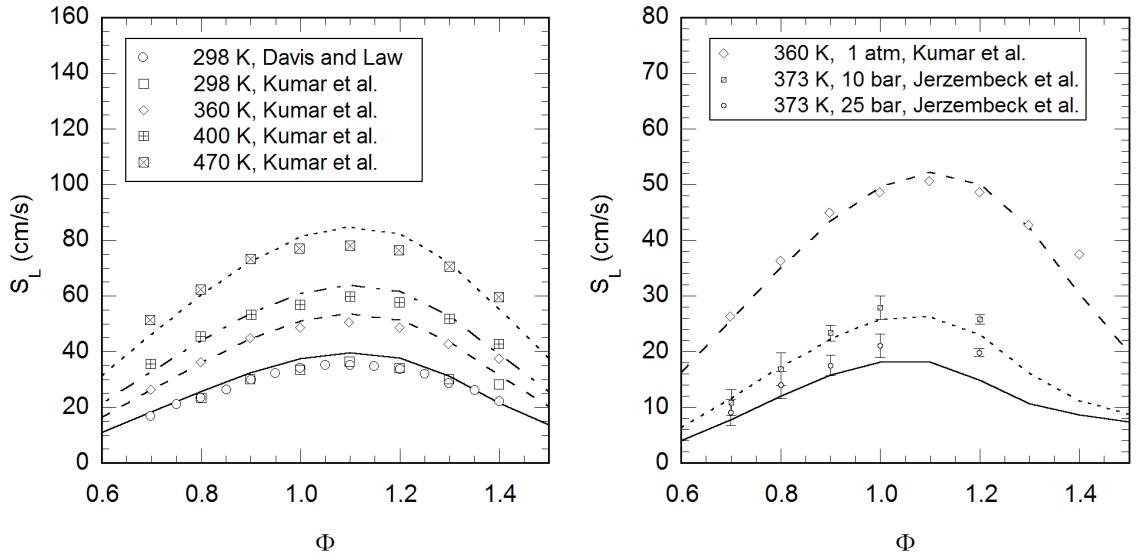

Figure 2.3: Iso-octane air laminar burning velocity as a function of Φ at atmospheric pressure for T_u ranging from 298 to 470 K (left) and with T_u = 360 K at 1 atm and T_u = 373 K at 10 and 25 bar (right). Experimental data (symbols) [17, 43, 44] vs. simulation (lines).

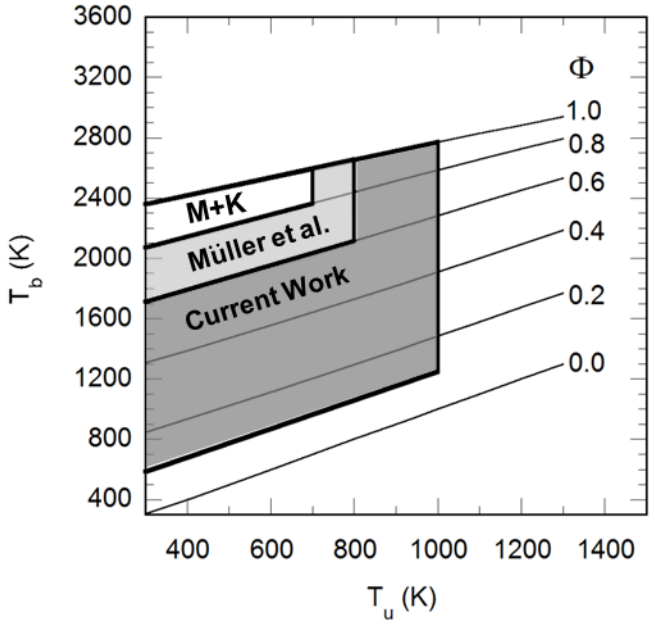

Figure 2.4: The range of T_u, T_b and corresponding Φ investigated in this work, compared to the previous studies of Müller et al. [22] and Metghalchi and Keck (M+K) [18].

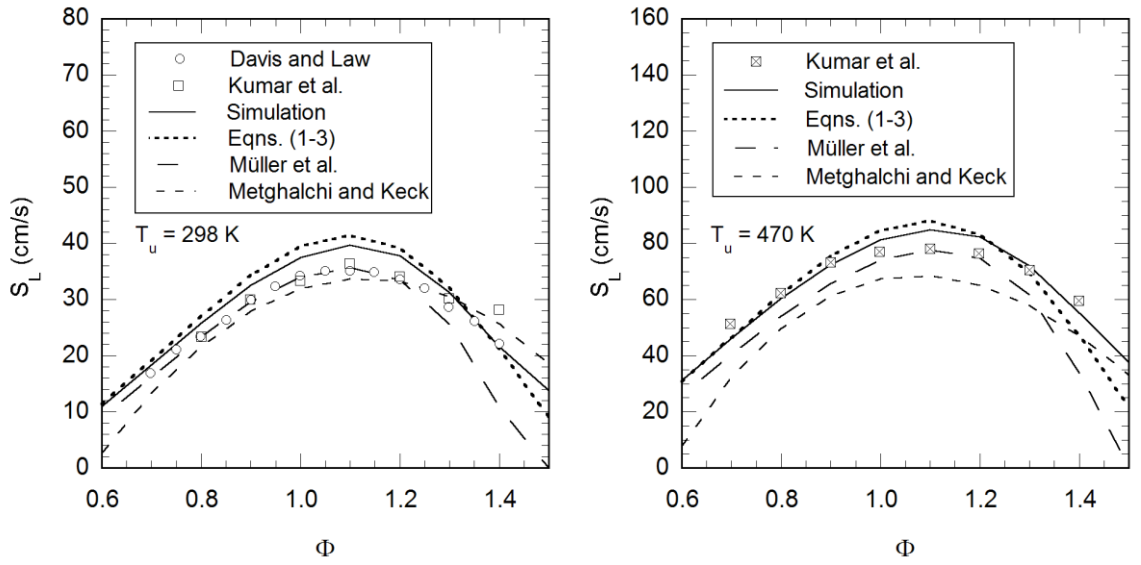

Figure 2.5: Iso-octane air laminar burning velocity as a function of Φ at atmospheric pressure for T_u = 298 K (left) and T_u = 470 K (right). Experimental data (symbols) [43, 44], HCT simulation results (solid line), with laminar burning velocity correlation predictions using Equations (2.1) through (2.3), Müller et al. [22] and Metghalchi and Keck [18] (dashed lines).

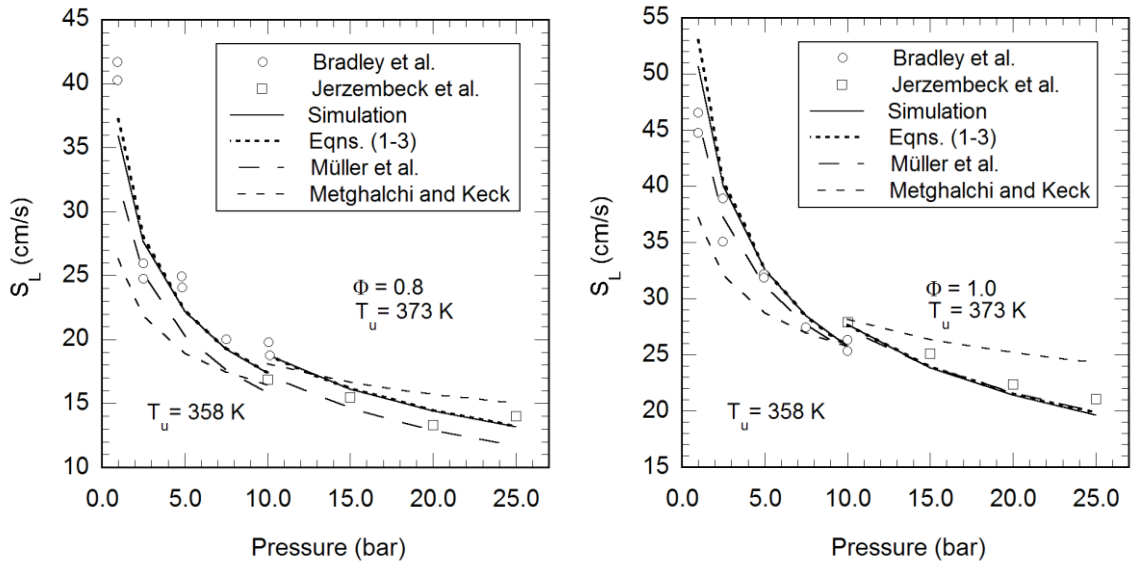

Figure 2.6: Iso-octane air laminar burning velocity as a function of pressure for Φ = 0.8 (left) and Φ = 1.0 (right). Experimental data (symbols) [17, 20], HCT simulation results (solid line), with laminar burning velocity correlation predictions using Equations (2.1) through (2.3), Müller et al. [22] and Metghalchi and Keck [18] (dashed lines).

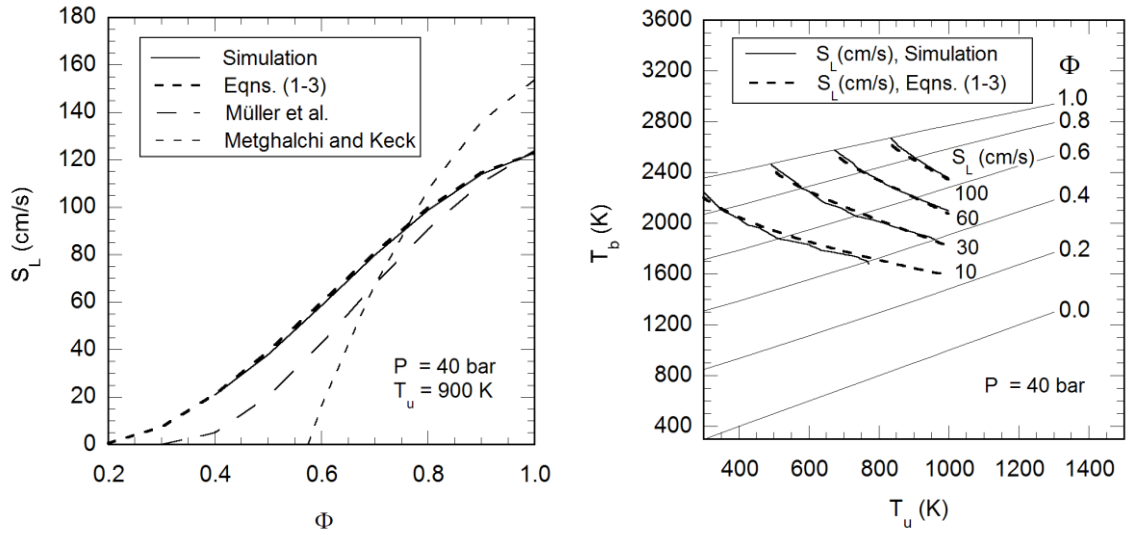

Figure 2.7: Iso-octane air laminar burning velocity as a function of Φ at T_u = 900 K, p = 40 bar (left) and laminar burning velocity iso-lines in the T_u - T_b domain at 40 bar (right). Laminar burning velocity simulation results from HCT (solid line), with laminar burning velocity correlation predictions (dashed lines) using Equations (2.1) through (2.3), Müller et al. [22] and Metghalchi and Keck [18] as noted.

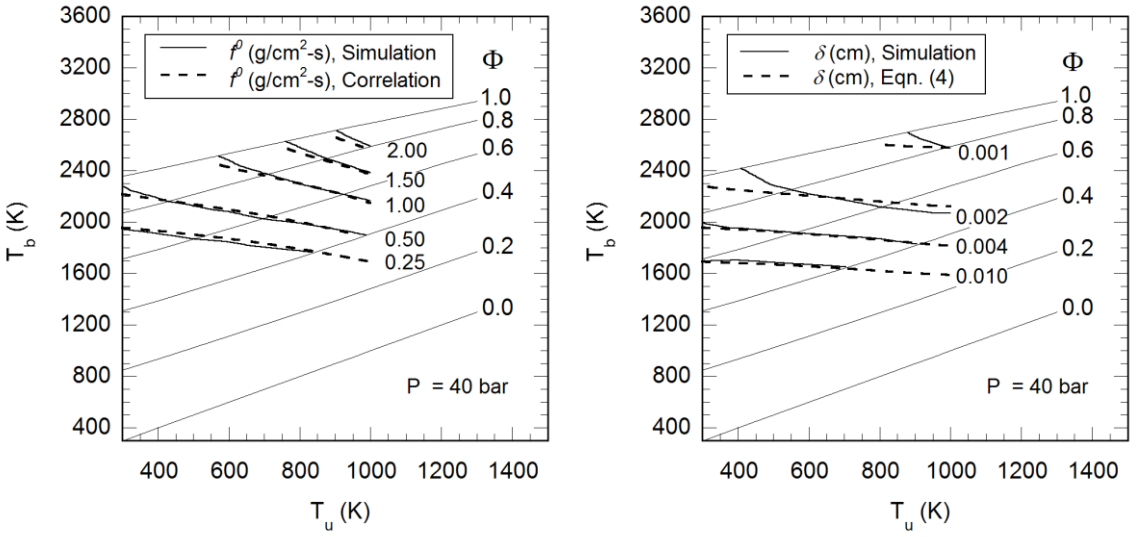

Figure 2.8: HCT and correlated mass burning flux contours, f^0, from Equations (2.1) through (2.3) and the unburned gas density (left) and HCT and correlated laminar flame thickness contours, δ, from Equation (2.4) (right) in the T_u - T_b domain at 40 bar.

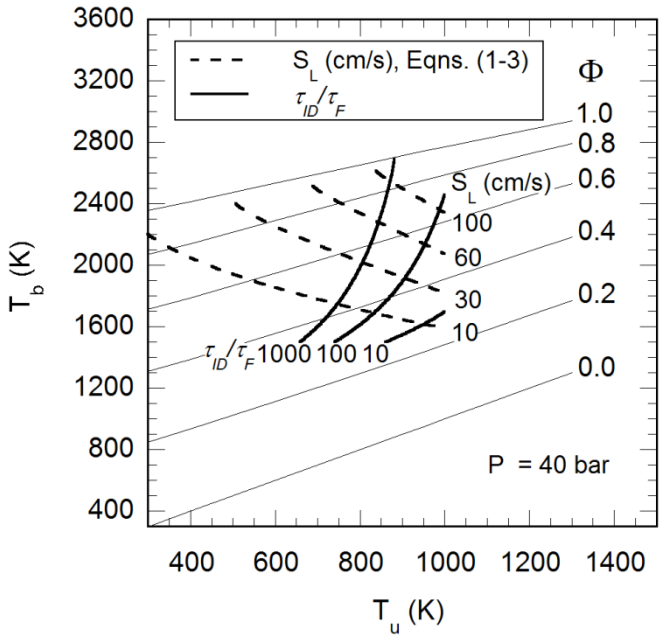

Figure 2.9: The ratio of ignition delay τ_{ID} to correlated reaction front time, τ_F, with S_L from Equations (2.1) through (2.3) and δ from Equation (2.4) in the T_u - T_b domain at 40 bar.

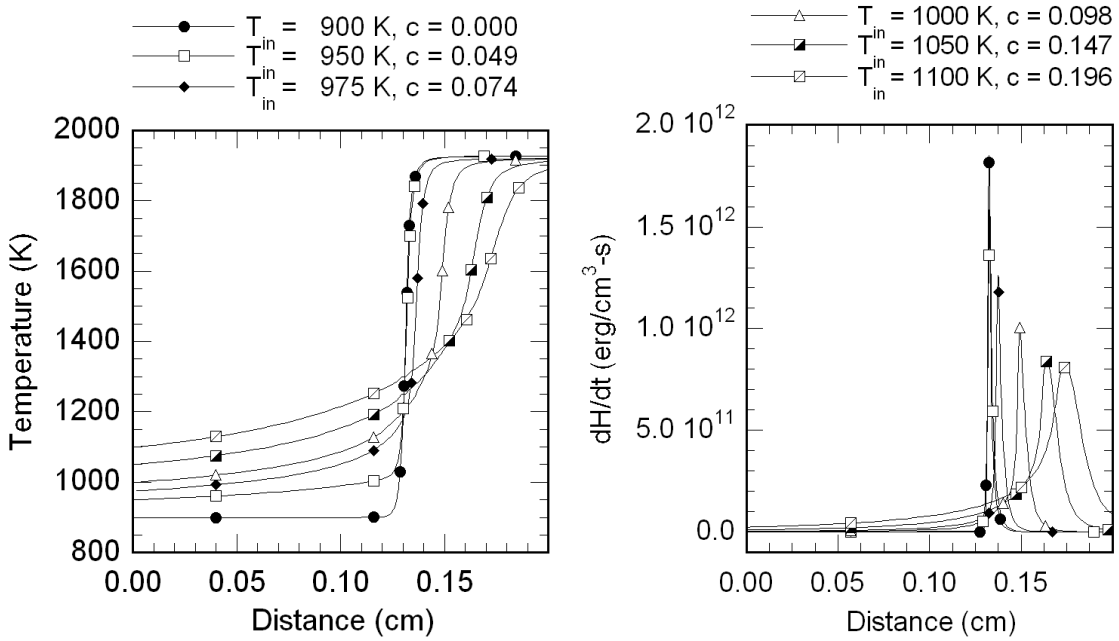

Figure 2.10: Spatial temperature (left) and heat release rate profile (right) from the PREMIX calculations for various levels of inlet reaction progress based on the SENKIN data for T_u = 900 K.

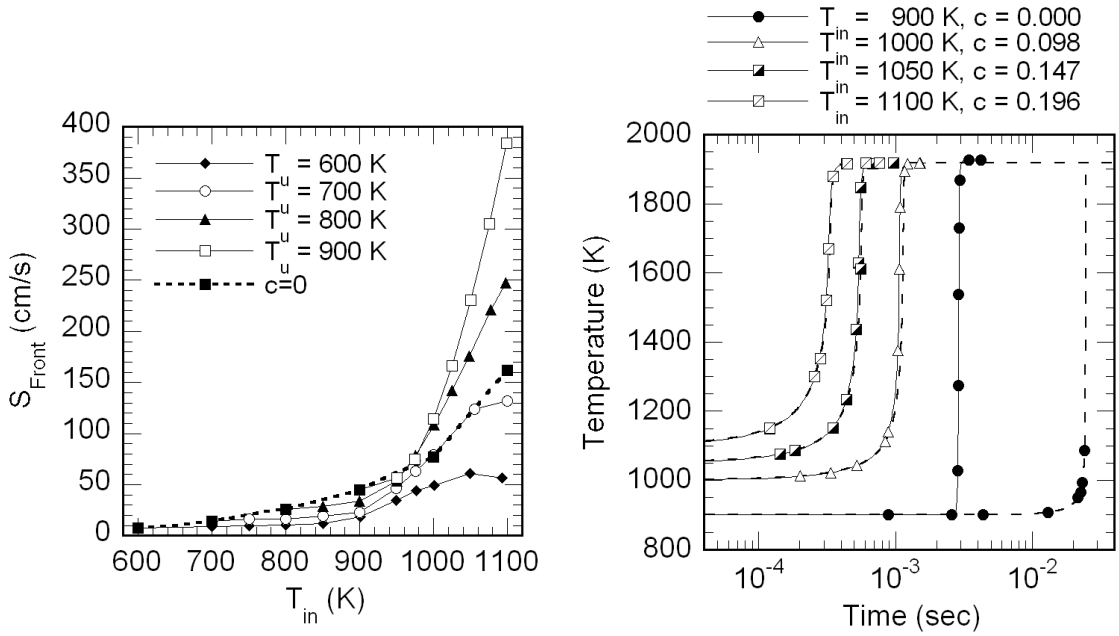

Figure 2.11: Reaction front speed versus T_{in}, for various T_u (left), where cases with zero inlet reaction progress are noted by the dashed line. PREMIX (solid lines) and SENKIN (dashed lines) temperature-time histories for T_u = 900 K (right). Time is referenced to the inlet of the PREMIX reactor.

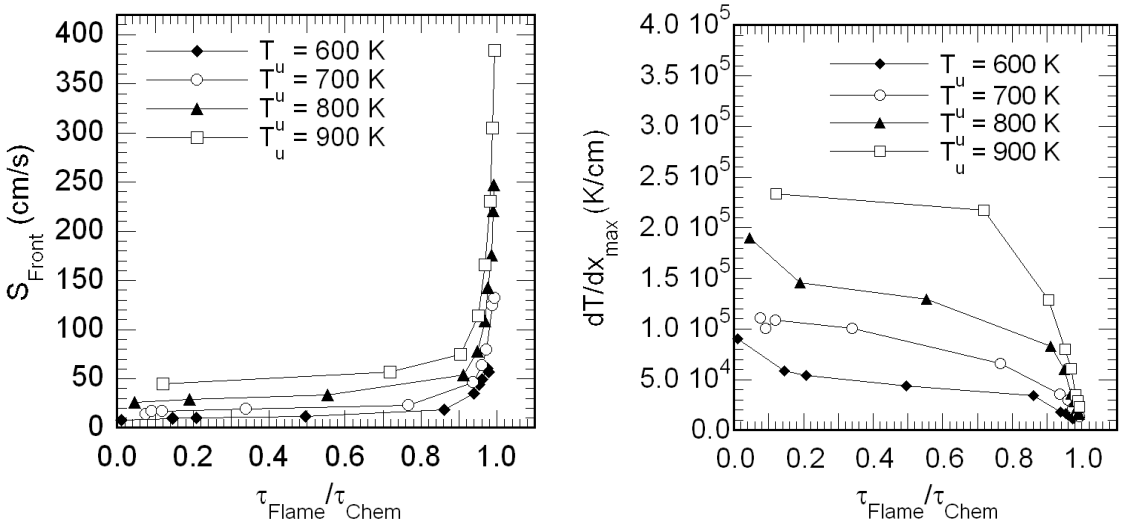

Figure 2.12: Reaction front speed as a function of τ_{Flame}/τ_{Chem} for various T_{in} at a given T_u (left), and the maximum temperature gradient as a function of τ_{Flame}/τ_{Chem} for various T_{in} at a given T_u (right).

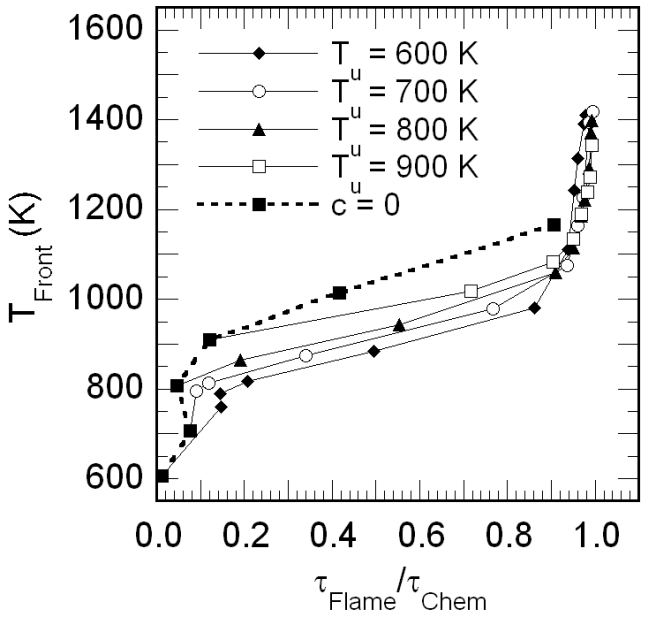

Figure 2.13: Reaction front base temperature (T_{front}) versus τ_{Flame}/τ_{Chem} for various T_{in} at a given T_u.

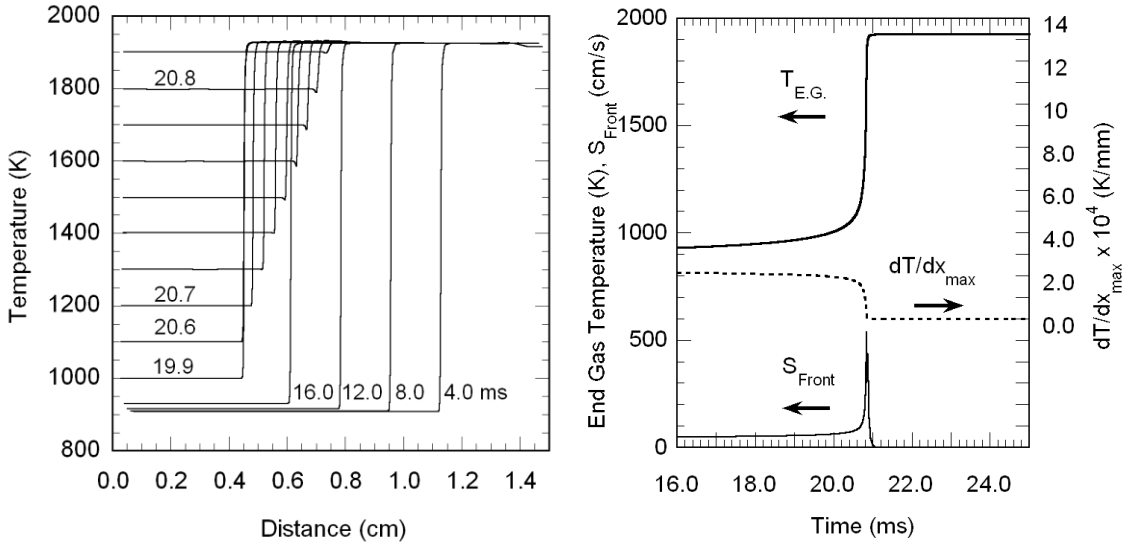

Figure 2.14: Evolution of the domain's temperature profile (left), where times are indicated from the start of the simulation in milliseconds. End-gas temperature ($T_{E.G.}$), reaction front speed (S_{Front}) and maximum temperature gradient (dT/dx_{max}) as a function of time (right). The figures are for Case 4 T_u = 907.7 K, p = 17.4 bar, Φ = 0.45.

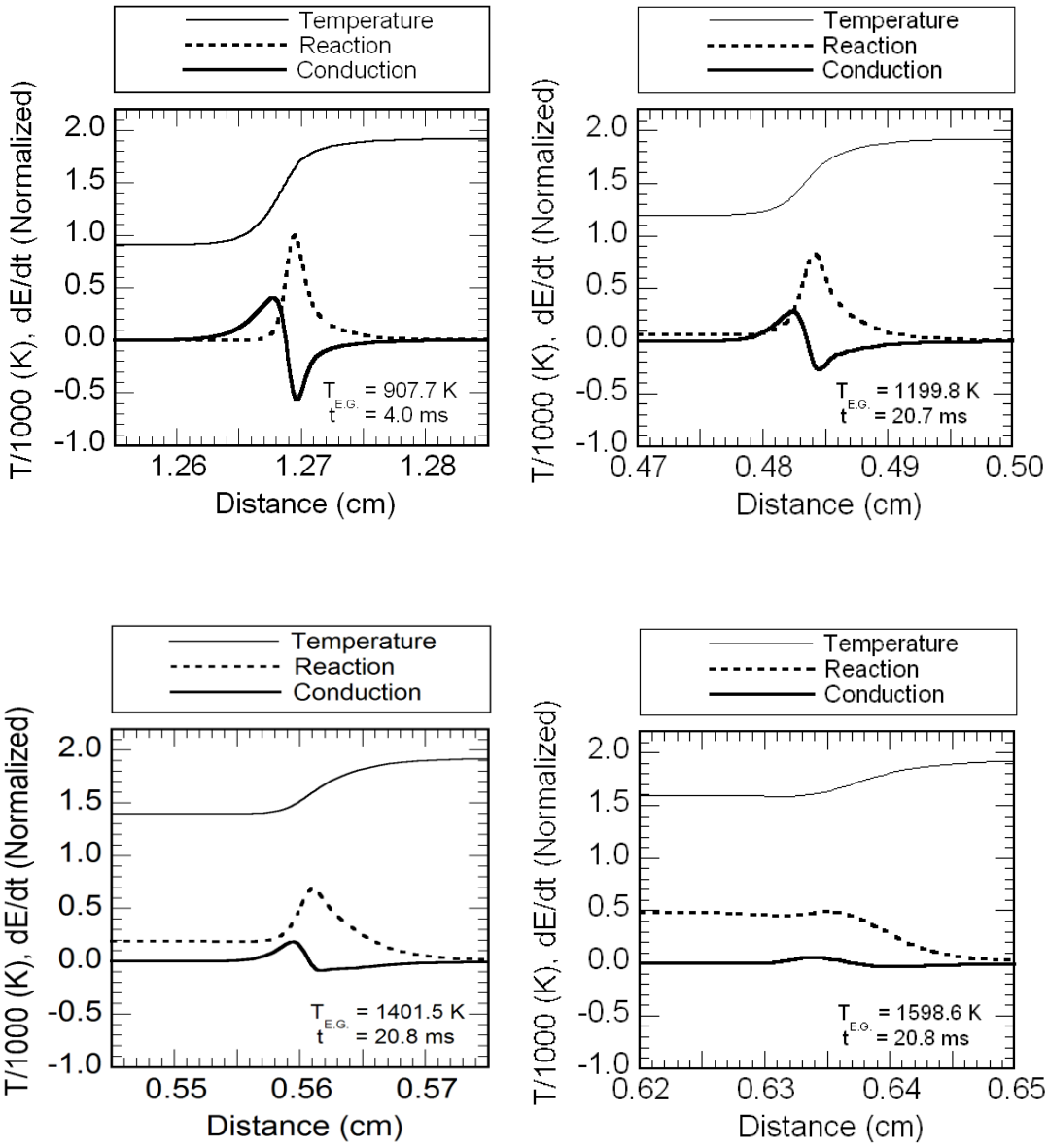

Figure 2.15: Evolution of temperature and rate of sensible energy change due to reaction and heat conduction in proximity to the reaction front for Case 4 at T_u = 907.7 K, p = 17.4 bar, Φ = 0.45 at $T_{E.G.}$ of 907.7 K (upper left), 1199.8 K (upper right), 1401.5 K (lower left) and 1598.6 K (lower right). The rates of energy change are normalized by a factor of 1.5E12 erg/cm^3-s.

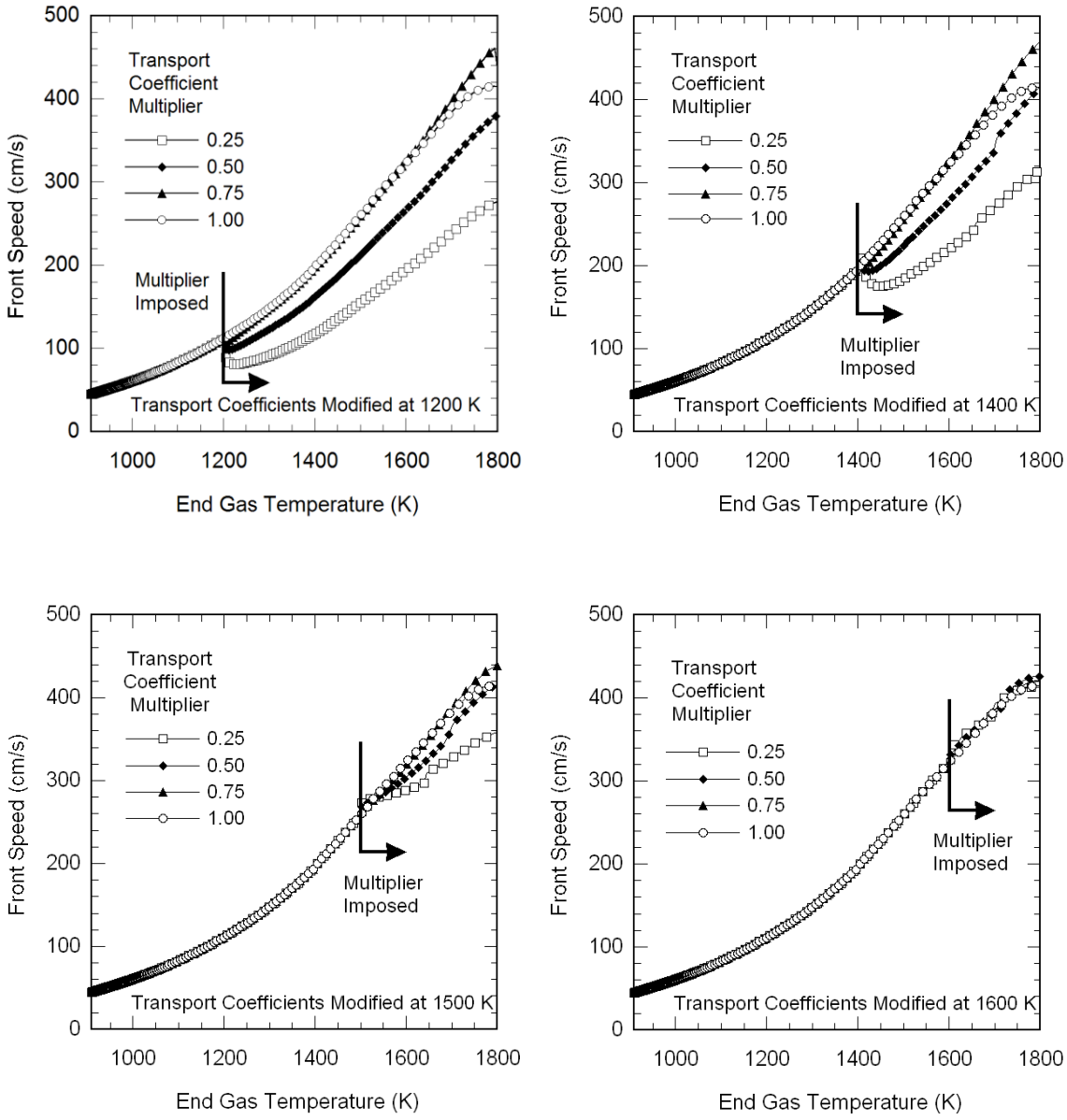

Figure 2.16: Transport coefficient parametric study results for Case 4 at T_u = 907.7 K, p = 17.4 bar, Φ = 0.45, where the transport coefficients are modified at $T_{E.G.}$ of 1200 K (upper left), 1400 K (upper right), 1500 K (lower left) and 1600 K (lower right).

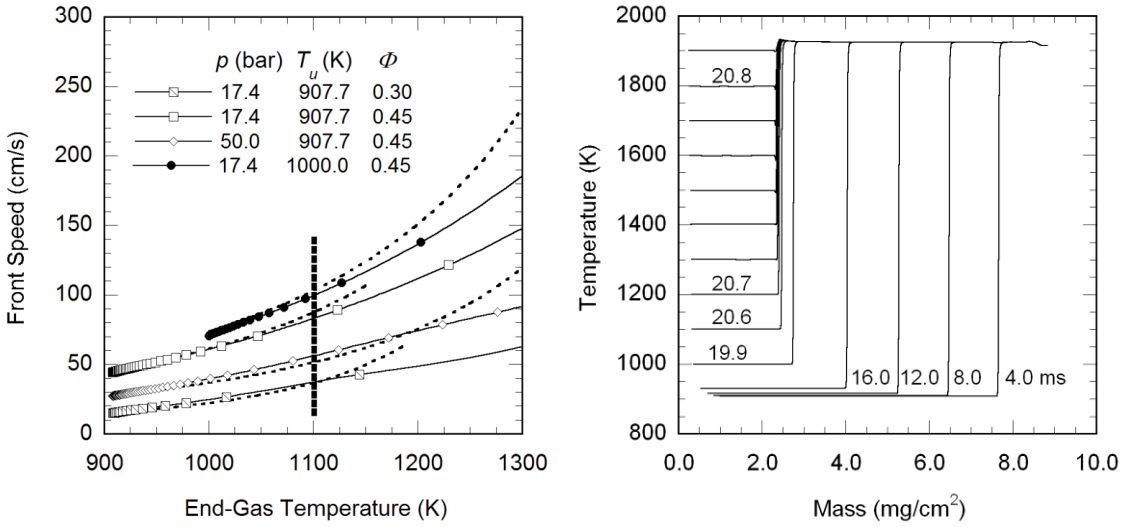

Figure 2.17: Reaction front speed vs. end-gas temperature for various T_u, p and Φ (left), where the solid lines are from the HCT burning velocity simulations, while the dashed lines are predictions from Equations (2.1) through (2.3). Temperature vs. mass per unit area for Case 4 at T_u = 907.7 K, p = 17.4 bar, Φ = 0.45 (right), with times indicated from the start of the simulation in milliseconds.

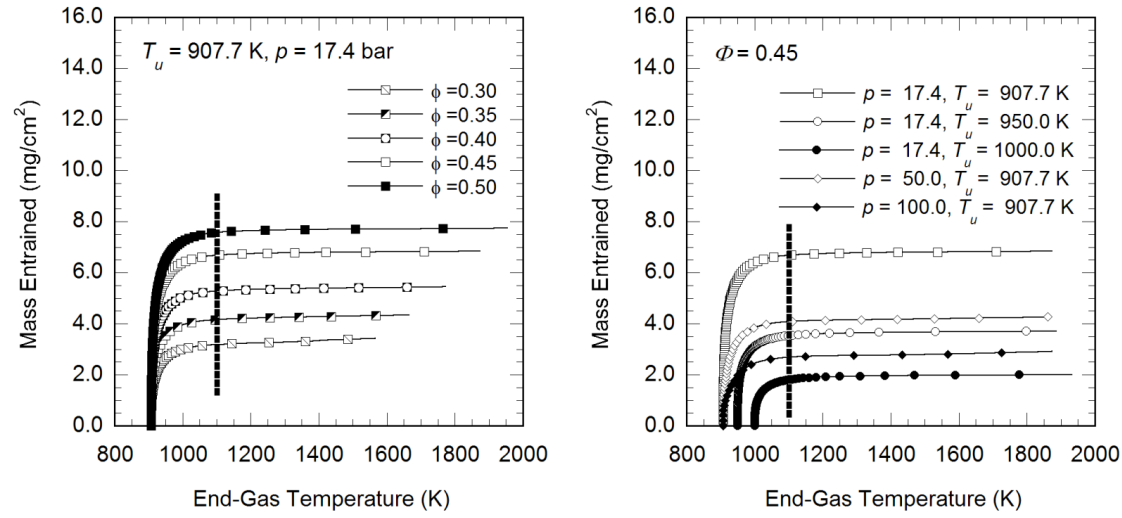

Figure 2.18: Mass entrained by the reaction front vs. end-gas temperature for various Φ at T_u = 907.7 K, p = 17.4 bar (left), and for various T_u and p at Φ = 0.45 (right).

2.8 References

1. Lavoie, G., Martz, J., Wooldridge, M., and Assanis, D., "A Multi-Mode Combustion Diagram for Spark Assisted Compression Ignition," *Combustion and Flame*, Vol. 157: 1106-1110, 2010.

2. Sjöberg, M. and Dec, J.E., "An Investigation Into Lowest Acceptable Combustion Temperatures for Hydrocarbon Fuels in HCCI Engines," *Proceedings of the Combustion Institute* 30: 2719-2726, 2005.

3. Flynn, P.F., Hunter, G.L., Durrett, R.P., Farrell, L.A., and Akinyemi, W.C., "Minimum Engine Flame Temperature Impacts on Diesel and Spark-Ignition Engine NOx Production," SAE Paper 2000-01-1177, 2000.

4. Lavoie, G.L. and Blumberg, P.N., "Measurements of NO Emissions From a Stratified Charge Engine: Comparison of Theory and Experiment," *Combustion, Science and Technology*, Vol. 8 (1 & 2): 25-37, 1973.

5. Martz, J.B., Middleton, R.J., Lavoie, G.A., Babajimopoulos, A., and Assanis, D.N., "A Computational Study and Correlation of Premixed Isooctane-Air Laminar Flame Properties under Spark Ignited and Spark Assisted Compression Ignition Engine Condition," *Accepted Combustion and Flame*, 2010.

6. He, X., Donovan, M., Zigler, B., Palmer, T., Walton, S., Wooldridge, M., and Atreya, A., "An Experimental and Modeling Study of Iso-Octane Ignition Delay Times Under Homogeneous Charge Compression Ignition Condition," *Combustion and Flame*, Vol. 142: 266-275, 2005.

7. Babajimopoulos, A., Lavoie, G.A., and Assanis, D.N., "On the Role of Top Dead Center Conditions in the Combustion Phasing of Homogeneous Charge Compression Ignition Engines," *Combustion Science and Technology*, Vol. 179(9): 2039-2063, 2007.

8. Sjöberg, M. and Dec, J.E., "Influence of Fuel Autoignition Reactivity on the High-Load Limits of HCCI Engine," SAE Paper 2008-01-0054, 2008.

9. Huang, Y., Sung, C., and Eng, J.A., "Dilution Limits of n-Butane/Air Mixtures Under Conditions Relevant to HCCI Combustion," *Combustion and Flame*, Vol 136: 457-466, 2004.

10. Persson, H., Agrell, M., Olsson, J.O., and Strom, H., "The Effect of Intake Temperature on HCCI Operation Using Negative Valve Overlap," SAE Paper 2004-01-0944, 2004.

11. Persson, H., Pfeiffer, R., Hultquvist, A., Johansson, B., and Strom, H., "Cylinder-to-Cylinder and Cycle-to-Cycle Variations at HCCI Operation With Trapped Residuals," SAE Paper 2005-01-0130, 2005.

12. Wagner, R.M., Edward, K.D., Daw, C.S., Green Jr., J.B., and Bunting, B.G., "On the Nature of Cyclic Dispersion in Spark Assisted HCCI Combustion," SAE Paper 2006-01-0418, 2006.

13. Zigler, B., Walton, S., He, X., Wiswall, J., Wooldridge, M., and Wooldridge, S., "Crank-Angle Resolved Imaging of Homogeneous Charge Compression Ignition Phenomena in a Single-Cylinder Research Engine," *Proceedings of the 2006 Technical Meeting of the Central States Section of The Combustion Institute*, Cleveland, OH, 2006.

14. Zigler, B.T., Walton, S.M., Karwat, D.M., Assanis, D., Wooldridge, M.S., and Wooldridge, S.T., "A Multi-Axis Imaging Study of Spark-Assisted Homogeneous Charge Compression Ignition Phenomena in a Single-Cylinder Research Engine," *ASME ICE Division 2007 Fall Technical Conference*, Charleston, SC, 2007.

15. Meneveau, C. and Poinsot, T., "Stretching and Quenching of Flamelets in Premixed Turbulent Combustion," *Combustion and Flame*, Vol. 86: 311-332, 1991.

16. Veynante, D. and Vervisch, L., "Turbulent Combustion Modeling," Progress in Energy and Combustion Science, Vol. 28: 192-266, 2002.

17. Jerzembeck, S., Peters, N., Pepiot-Desjardins, P., and Pitsch, H., "Laminar Burning Velocities at High Pressure for Primary Reference Fuels and Gasoline: Experimental and Numerical Investigation," *Combustion and Flame*, Vol. 156: 292-301, 2009.

18. Metghalchi, M. and Keck, J., "Burning Velocities of Mixtures of Air with Methanol, Isooctane, and Indolene at High Pressure and Temperature," *Combustion and Flame*, Vol 48: 191-210, 1982.

19. Ryan, T. and Lestz, S., "The Laminar Burning Velocity of Isooctane, N-Heptane, Methanol, Methane, and Propane at Elevated Temperature and Pressure in the Presence of a Diluent," SAE Paper 800103, 1980.

20. Bradley, D., Hicks, R., Lawes, M., Sheppard, C., and Woolley, R., "The Measurement of Laminar Burning Velocities and Markstein Numbers for Iso-octane-Air and Iso-octane-n-Heptane-Air Mixtures at Elevated Temperatures and Pressures in an Explosion Bomb," *Combustion and Flame*, Vol. 115: 126-144, 1998.

21. Göttgens, J., Mauss, F., and Peters, N., "Analytic Approximations of Burning Velocities and Flame Thicknesses of Lean Hydrogen, Methane, Ethylene, Ethane, Acetylene, and Propane Flames," *Proceedings of the Twenty-Fourth International Symposium on Combustion:* 129-135, 1992.

22. Müller, U.C., Bollig, M., and Peters, N., "Approximations for Burning Velocities and Markstein Numbers for Lean Hydrocarbon and Methanol Flames," *Combustion and Flame*, Vol. 108: 349-356, 1997.

23. Persson, H., Hultqvist, A., Johansson, B., and Remon, A., "Investigation of the Early Flame Development in Spark-Assisted HCCI Combustion Using High-Speed Chemiluminescence Imaging," SAE Paper 2007-01-0212, 2007.

24. Reuss, D.L., Kuo, T., Silvas, G., Natarajan, V., and Sick, V., "Experimental Metrics for Identifying Origins of Combustion Variability During Spark-Assisted Compression Ignition," *International Journal of Engine Research*, Vol. 9: 409-434, 2008.

25. Zigler, B., *An Experimental Investigation of the Properties of Low Temperature Combustion in an Optical Engine*, Ph.D. Thesis University of Michigan, Ann Arbor (2008).

26. Lund, C., "HCT: A General Computer Program for Calculating Time-Dependent Phenomena Involving One-Dimensional Hydrodynamics, Transport, and Detailed Chemical Kinetics," Lawrence Livermore National Laboratory Report UCRL-52504, 1978.

27. Westbrook, C.K. and Dryer, F., "Prediction of Laminar Flame Properties of Methanol-Air Mixtures," *Combustion and Flame*, Vol. 37: 171-192, 1980.

28. Westbrook, C.K. and Dryer, F., "Simplified Reaction Mechanisms for the Oxidation of Hydrocarbons," *Combustion Science and Technology*, Vol. 27: 31-43, 1981.

29. Westbrook, C.K., Adamczyk, A.A., and Lavoie, G.A., "A Numerical Study of Laminar Flame Wall Quenching," *Combustion and Flame*, Vol. 40: 81-99, 1981.

30. Westbrook, C.K., Dryer, F.L., and Schug, K.P., "Numerical Modeling of Ethylene Oxidation in Laminar Flames," *Combustion and Flame*, Vol. 52: 299-313, 1983.

31. Curran, H., Gaffuri, P., Pitz, W., and Westbrook, C.K., "A Comprehensive Modeling Study of n-Heptane Oxidation," *Combustion and Flame*, Vol. 114: 149-177, 1998.

32. Corre, C., Dryer, F.L., Pitz, W.J., and Westbrook, C.K., "Two-Stage N-Butane Flame: A Comparison Between Experimental Measurements and Modeling Results," *Proceedings of the Twenty-Fourth International Symposium on Combustion:* 843-850, 1992.

33. Curran, H.J., Dunphy, M.P., Simmie, J.M., Westbrook, C.K., and Pitz, W.J., "Shock Tube Ignition of Ethanol, Isobutene and MTBE: Experiments and Modeling," *Proceedings of the Twenty-Fourth International Symposium on Combustion:*769-776, 1992.

34. Wang, S., Miller, D., Cernansky, N., Curran, H., Pitz, W.J., and Westbrook, C.K., "A Flow Reactor Study of Neopentane Oxidation at 8 Atmospheres: Experiments and Modeling," *Combustion and Flame*, Vol. 118: 415-430, 1999.

35. Curran, H., Gaffuri, P., Pitz, W.J., and Westbrook, C.K., "A Comprehensive Modeling Study of iso-Octane Oxidation," *Combustion and Flame*, Vol. 129: 253-280, 2004.

36. Lutz, A., Kee, R., and Miller, J., "SENKIN: A Fortran Program for Predicting Homogeneous Gas Phase Chemical Kinetics with Sensitivity Analysis," Sandia National Laboratory Report SAND87-8240, 1988.

37. Kee, R., Grcar, J., Smooke, M., and Miller, J., "A Fortran Program for Modeling Steady Laminar One-Dimensional Premixed Flames," Sandia National Laboratory Report SAND85-8240, 1985.

38. Tham, Y., Bisetti, F., and Chen, J.Y., "Development of a Highly Reduced Mechanism for Iso-Octane HCCI Combustion with Targeted Search Algorithm," *ASME Journal of Engineering for Gas Turbines and Power*, Vol. 130, 2008.

39. Kee, R., Dixon-Lewis, G., Warnatz, J., Coltrin, M.E., and Miller, J.A., "A Fortran Computer Code Package for the Evaluation of Gas-Phase Multicomponent Transport Properties," Sandia National Laboratory Report SAND86-8246, 1986.

40. Davidson, D.F., Gauthier, B.M., and Hanson, R.K., "Shock tube ignition measurements of iso-octane/air and toluene/air at high pressures," *Proceedings of the Combustion Institute* 30: 1175-1182, 2005.

41. Vasu, S.S., Davidson, D.F., and Hanson, R.K., "Shock Tube Measurements and Modeling of Ignition Delay Time in Lean Iso-octane/Air," *Proceedings of the 25th International Symposium on Shock Waves*, Bangalore, India, 2005.

42. Shen, H.-P., Vanderover, J., and Oehlschlaeger, M., "A shock tube study of iso-octane ignition at elevated pressures: The influence of diluent gases," *Combustion and Flame*, Vol. 155: 739-755, 2008.

43. Davis, S.G. and Law, C.K., "Determination of and Fuel Structure Effects on Laminar Flame Speeds of C1 to C8 Hydrocarbons," *Combustion, Science and Technology*, Vol. 140: 427-449, 1998.

44. Kumar, K., Freeh, J.E., Sung, C.J., and Huang, Y., "Laminar Flame Speeds of Preheated iso-Octane/O2/N2 and n-Heptane/O2/N2 Mixtures," *Journal of Propulsion and Power*, Vol. 23 (2): 428-436, 2007.

45. Law, C., 2006, *Combustion Physics*. Cambridge University Press, New York.

46. Hultquvist, A., Christensen, M., Johansson, B., Richter, M., Nygren, J., Hult, J., and Alden, M., "The HCCI Combustion Process in a Single Cycle - High-Speed Fuel Tracer LIF and Chemiluminescence Imaging," SAE Paper 2002-01-0424, 2002.

47. Schiessl, R., Dreizler, A., Maas, U., Grant, A., and Ewart, P., "Double-Pulse PLIF Imaging of Self-Ignition Centers in an SI Engine," SAE Paper 2001-01-1925, 2001.

48. Konig, G., Maly, R.R., Bradley, D., Lau, A.K.C., and Sheppard, C.G.W., "Role of Exothermic Centres on Knock Initiation and Knock Damage," SAE Paper 902136, 1990.

49. Zel'dovich, Y., "Regime Classification of an Exothermic Reaction with Nonuniform Initial Conditions," *Combustion and Flame*, Vol. 39: 211-214, 1980.

50. Pitz, W.J., and Westbrook, C.K. "Interactions Between a Laminar Flame and End Gas Autoignition," in J.R. Bowen, J.C. Leyer and R.I. Soloukhin (Eds.), *Dynamics of Reactive Systems Part II: Modeling and Heterogeneous Combustion, Progress in Astronautics and Aeronautics series*, Vol. 105, 1986.

51. Gu, X.J., Bradley, D., and Emerson, D.R., "Modes of Reaction Front Propagation from Hot Spots," *Combustion and Flame*, Vol. 133: 63-74, 2003.

52. Sankaran, R., Im, H.G., Hawkes, E.R.,, and Chen, J.H, "The Effects of Non-Uniform Temperature Distribution on the Ignition of a Lean Homogeneous Hydrogen-Air Mixture," *Proceedings of the Combustion Institute* 30: 875-882, 2005.

53. Chen, J.H., Hawkes, E.R., Sankaran, R., Mason, S.D., and Im, H.G., "Direct numerical simulation of ignition front propagation in a constant volume with temperature inhomogeneities I. Fundamental analysis and diagnostics," *Combustion and Flame*, Vol. 145: 128-144, 2006.

54. Bansal, G. and Im, H.G., "Direct Numerical Simulation of Auto-ignition and Front Propagation in Hydrogen-Air Mixture with Thermal and Compositional Inhomogeneities," *Proceedings of the 6th US National Combustion Meeting*, Ann Arbor, MI, 2009.

55. Eckert, P., Kong, S.C., and Reitz, R.D., "Modelling Autoignition and Engine Knock Under Spark Ignition Conditions," SAE Paper 2003-01-0011, 2003.

56. Liang, L., Reitz, R., Iyer, C., and Yi, J., "Modeling Knock in Spark-Ignition Engines Using a G-Equation Combustion Model Incorporating Detailed Chemical Kinetics," SAE Paper 2007-01-0165, 2007.

57. Yang, S. and Reitz, R.D., "Improved combustion submodels for modeling gasoline engines with the level set G equation and detailed chemical kinetics," *Proceedings of the Institution of Mechanical Engineers, Part D, Journal of Automobile Engineering*, Vol.223 (5): 703-726, 2009.

58. Held, T. and Dryer, F., "An Experimental and Computational Study of Methanol Oxidation in the Intermediate- and High-Temperature Regimes," *Proceedings of the Twenty-Fifth International Symposium on Combustion:* 901-908, 1994.

59. Westbrook, C.K., "Chemical Kinetics of Hydrocarbon Ignition in Practical Combustion Systems," *Proceedings of the Combustion Institute* 28: 1563-1577, 2000.

60. Kelly-Zion, P.L. and Dec, J.E., "A Computational Study of the Effect of Fuel Type on Ignition Time in HCCI Engines," *Proceedings of the Combustion Institute* 28: 1187-1194, 2000.

61. Martz, J.B., Kwak, H., Im, H.G., Lavoie, G.A., and Assanis, D.N., "Combustion Regime of a Reacting Front Propagating into an Auto-Igniting Mixture," *Proceedings of the Combustion Institute* 33 *(In Press)*, 2010.

CHAPTER 3

CFMZ MODEL FORMULATION

3.1 The Regimes of SACI Combustion

SACI combustion combines premixed combustion modes ranging from turbulent reaction front propagation to homogeneous explosion [1]. From combustion images [2-4], it is apparent that SACI may be dominated by a single mode or may involve multiple modes, such as reaction front propagation with concurrent end-gas auto-ignition distributed throughout the combustion chamber.

From the previously mentioned imaging studies, it is generally accepted that HCCI combustion is chemically controlled [5-7]. Images of combusting SACI end-gasses [2-4, 8] closely resemble those from HCCI engines. Considering this resemblance and the similarity of SACI to knocking SI combustion [9], the combustion mode of the SACI end-gas can also be considered chemically dominated upon reaching the conditions required for volumetric ignition.

Under conventional SI combustion conditions, the premixed reaction fronts observed during the initial stages of SACI [2-4] are typically modeled as flamelets [10]. The flamelet is often treated as a laminar flame which is wrinkled by the surrounding turbulent flow field, propagating at a consumption speed that is similar to the laminar flame speed [11]. The main effect of the flame front wrinkling process is the accompanying increase in flame surface area and the associated enhanced mass burning rate [12, 13]. Flamelet theory has recently been supported by the direct simulations of

turbulent methane-air flames by Bell et al. [14] and Hawkes and Chen [15], which show that flame front wrinkling and the resulting increase in the flame surface area are the dominant cause for the increase in fuel consumption rates within the turbulent flame.

Contrary to the Broadened Preheat Zone/Thin Reaction Zone flamelet concept [16] where the small scales of the turbulent flow modify the preheat zone structure of the laminar flame, the flamelet concept appears to remain valid even in situations where the Karlovitz number, *Ka* [10], is elevated:

$$Ka = \frac{\tau_c}{\tau_k} = \left(\delta / l_k\right)^2 \tag{3.1}$$

Where τ_c and τ_k are chemical and turbulent timescales, δ is the laminar flame thickness and l_k is the Kolmogorov length scale. In his review of preheat and reaction zone imaging studies, Driscoll notes that while the preheat zone thickness of turbulent premixed flames ranges from 0.4 to 3.0 times that of a corresponding un-stretched laminar flames, there has been no direct experimental evidence linking this thickening to small eddy interaction with the preheat zone of the flame [12]. Instead, it is argued the observed thickening could be result of strain effects or a variety of other factors complicating the flame thickness measurements, including laser sheet misalignment, inadequate spatial resolution of the measurement technique or flamelet merging, where the merging of several flame fronts gives the appearance of a single, much thicker flame [12].

The thickening of the laminar flame due to strain/curvature effects can be understood through the Lewis number, *Le*, which is defined according to Equation (3.2):

$$Le = \frac{\alpha}{D_i} = \frac{\lambda}{\rho c_p D_i} \tag{3.2}$$

Where α and λ are the mixture thermal diffusivity and conductivity, D_i is the diffusivity of the deficient reactant species *i* into the mixture, and ρ and c_p are the mixture density

and heat capacity. Counterflow flame studies with near unity Lewis numbers have shown that strain has a minimal effect on the structure of experimental and computed flames [17]. This is in stark contrast to strained non-unity Lewis number flames, where imbalances in heat and mass diffusion may affect the flame temperature, while differential diffusion may alter the local concentration of reactants entering the wrinkled flame. For differential diffusion, consider a reactant stream approaching a wrinkled flame surface where the *Le* defined with respect to the deficient reactant species (large fuel molecules in lean mixtures) is elevated. *Le* is elevated because the fuel molecule has high molecular weight/lower diffusivity relative to the oxidizer, which has a diffusivity of D_j. Because of differential diffusion, where the diffusion velocity of the oxidizer species, D_j, is greater than D_i, the equivalence ratio of the mixture approaching a positively stretched cusp of the flame becomes leaner, effectively decreasing the burning velocity while increasing the thickness of the flame [18]. As a result, the mixture approaching a neighboring negatively stretched cusp of the flame becomes richer. As the consumption speed varies linearly with flame front curvature [19] and the PDF of the curvature within a turbulent flame is approximately symmetric about zero, these highly localized, non-unity Lewis number effects associated with curvature are essentially mutually offsetting when examined on a more global basis across the flame front [19, 20]. Therefore, within RANS flamelet models, where the cell dimensions are significantly larger than those of the wrinkled flame front, the scaling of S_L with stretch correction factors, I_0, is typically not performed [21], and the use of un-stretched laminar flame speeds is appropriate for prediction of bulk phenomena such as the mass burning rate within the computational cell [19]. Poinsot et al. note that the key issue associated with flamelet modeling therefore is the accurate prediction of the flame surface density [22].

Even with partial flame front quenching, the flamelet assumption is assumed to remain valid as long as the growth rate of the flame surface outpaces that of the quenched zones [11]. In addition, it is postulated that the general lack of local extinction sites in

turbulent flame imaging experiments with elevated *Ka* likely results from the re-ignition of the quenched zones by neighboring burned gases [12].

The boundary of the flamelet combustion regime is noted at the onset of complete flamelet quenching, where quenching is induced by processes such as turbulent strain or external heat loss. This quenching process has been observed in both direct simulation [23] and experiments, where the process was found to depend on *Le* [24]. Previously, it has been proposed that the flamelet regime transitions to the distributed combustion regime when the turbulent eddies are small enough to react with the reaction zone of the flame, causing a sharp drop in flame temperature and flame extinction [25]. However, the existence of the distributed combustion regime, where reaction zones with thicknesses much greater than that of a laminar flame are created through rapid turbulent mixing has not been directly confirmed [12]. Rather, it has been proposed that this regime is better represented by chemically controlled combustion processes such as HCCI, where instead of generating distributed reaction zones through quenching and rapid mixing, the reactant mixture is compression heated to the point of ignition [12].

3.2 Modeling SACI Combustion in KIVA-3V

Because of its ability to spatially resolve the combustion chamber to capture detailed flow field effects, direct injection events and the resulting compositional and thermal stratification, KIVA-3V was selected as the simulation platform for the modeling of SACI combustion in the current work. In KIVA-3V, combustion within a turbulent flow is modeled through chemical source terms in the species density ($\dot{\rho}_m^C$) and internal energy ($\dot{Q}^C$) transport equations, Equations (3.3) and (3.4) respectively.

$$\frac{\partial \rho Y_m}{\partial t} + \frac{\partial \rho u_k Y_m}{\partial x_k} = \frac{\partial}{\partial x_k}\left(\frac{\mu_t}{\sigma_m}\frac{\partial Y_m}{\partial x_k}\right) + \dot{\rho}_m^C + \dot{\rho}^S \delta_{ml} \tag{3.3}$$

$$\frac{\partial \rho I}{\partial t} + \frac{\partial \rho u_k I}{\partial x_k} = -p\frac{\partial u_k}{\partial x_k} + \frac{\partial}{\partial x_k}\left(\lambda \frac{\partial T}{\partial x_k}\right) + \frac{\partial}{\partial x_k}\left[\frac{\mu_t}{\sigma}\sum_i h_i \frac{\partial Y_i}{\partial x_k}\right] + \rho\varepsilon + \dot{Q}^C + \dot{Q}^W \qquad (3.4)$$

Where in Equation (3.3), ρ is the mean density, Y_m is the mass fraction of species m, u_k is the cell velocity in the direction of repeated index k, μ_t and σ_m are the dynamic turbulent viscosity and Schmidt number, where σ_m is set equal to 1.0, $\dot{\rho}^S$ is the spray source term for species m and δ is the Dirac delta function. While in Equation (3.4), I is the specific internal energy, p is the fluid pressure, λ is the mixture thermal conductivity, T is the mixture temperature, h_m is the specific enthalpy of species m, summed over the index i, where $i = 1, \ldots nsp$, where nsp is the total number of species in the chemical mechanism, while ε is the dissipation rate of the turbulent kinetic energy and $\dot{Q}^W$ is an external heat loss rate term given by the Law of the Wall.

The reaction front cannot be resolved by KIVA-3V as the dimensions of the computational cell are significantly greater than that of the front. Therefore, a sub grid model is required to predict the contributions of the reaction front and chemically controlled combustion to the chemical source terms in Equations (3.3) and (3.4). A generalized sub-grid model for SI, SACI and HCCI combustion is developed in the current work for the purposes of calculating these source terms. The sub-grid model divides a KIVA-3V computational cell into a maximum of three zones, as shown in Figure 3.1, which is physically consistent with images of SACI and HCCI combustion [2-4]. These zones include:

- A Reactant Zone (u), located upstream of the Reaction Front, accounting for heat release due to auto-ignition. This zone is treated as a homogeneous reactor.
- A Reaction Front, which is treated as a flamelet, separating the Reactant and Product Zones.

- A Product Zone (b), located downstream of the reaction front, accounting for chemistry in the burned gasses produced by the Reaction Front. This zone is also treated as a homogeneous reactor.

The current sub-grid modeling approach modifies and combines an existing implementation [26, 27] of the Coherent Flamelet model [11, 28, 29] for the treatment of the reaction front with the fully coupled Multi-Zone approach [27, 30] for the simulation of detailed chemical kinetics within the Reactant and Product Zones. These models are described in more detail below in Sections 3.3 and 3.4.

3.3 Reaction Front Modeling with the Coherent Flamelet Model

For the current work, reaction front propagation during SACI combustion will be simulated in KIVA-3V with the Coherent Flamelet model [11, 28, 29], given this model's physical treatment of flame stretch and its ability to accurately describe the Reactant Zone state. The information required to determine the state of the Reactant Zone is obtained in part through the solution of an additional *nsp* species density transport equations for the species within the Reactant Zone [26, 29], Equation (3.5). In addition, a sensible enthalpy transport equation is also introduced for the Reactant Zone, Equation (3.11) [26, 29]. The solution of these equations, in addition to the assumption of uniform pressure between the computational cell and its associated Reactant Zone fixes the Reactant Zone state. The Product Zone state is then obtained through mass and energy balances with information from the Reactant Zone and KIVA computational cell solutions, described further in Section 3.7.

The Reactant Zone transport equations are now discussed in detail. The species densities of the Reactant Zone are obtained by the solution of Equation (3.5):

$$\frac{\partial \rho Y_{m,u}}{\partial t} + \frac{\partial \rho u_k Y_{m,u}}{\partial x_k} = \frac{\partial}{\partial x_k}\left(\frac{\mu_t}{\sigma_m}\frac{\partial Y_{m,u}}{\partial x_k}\right) + \dot{\rho}^C_{m,u,RF} + \dot{\rho}^C_{m,u,AI} \tag{3.5}$$

This equation has been previously used by Baritaud et al. for the modeling of SI combustion with a non-reacting end-gas [29]. Where $\dot{\rho}^C_{m,u,RF}$ is a sink term due to reaction front consumption, while an additional chemical source term, $\dot{\rho}^C_{m,u,AI}$, has been added within the current work to account for auto-ignition within the Reactant Zone.

Equation (3.5) has been formulated so that the resulting mass fractions for the mass of species *m* within the Reactant zone, *m,u*, are calculated relative to the mass of the computational cell, m_{cell}, where from Equation (3.6):

$$Y_{m,u} = \frac{m_{m,u}}{m_{cell}} \tag{3.6}$$

The resulting species density within Equation (3.5) has units of mass of Reactant Zone species *m*, $m_{m,u}$, per unit cell volume, *V*:

$$\rho Y_{m,u} = \frac{m_{cell}}{V}\frac{m_{m,u}}{m_{cell}} \tag{3.7}$$

The mass of the individual Reactant Zone species, $m_{m,u}$, is found through Equation (3.8), where:

$$m_{m,u} = \rho Y_{m,u} V \tag{3.8}$$

In turn, the mass of the Reactant Zone, m_u, is obtained through Equation (3.9):

$$m_u = \sum_i m_{i,u} \tag{3.9}$$

Finally, the mass fraction of the Reactant Zone species relative to the Reactant Zone mass, Y^u_m, is found with Equation (3.10):

$$Y^u_m = \frac{m_{m,u}}{m_u} \tag{3.10}$$

The specific enthalpy of the Reactant Zone, h_u, is determined through the solution of Equation (3.11), also previously used by Baritaud et al. [29] for modeling of SI combustion with non-reacting end-gasses:

$$\frac{\partial \rho h_u}{\partial t} + \frac{\partial \rho u_k h_u}{\partial x_k} = \frac{\partial}{\partial x_k}\left(\frac{\mu_t}{Pr}\frac{\partial h_u}{\partial x_k}\right) + \rho\varepsilon + \frac{\rho}{\rho_u}\frac{\partial p}{\partial t} + \dot{Q}_{w,u} + \dot{Q}^C_{u,AI} \tag{3.11}$$

Where Pr is the Prandtl number, set to 1.0, and where ρ_u is the density of the Reactant Zone, relative to the Reactant Zone mass and volume. Previous studies have adopted Equation (3.11) over an internal energy transport equation because of its simplified treatment of the Reactant Zone compression resulting from heat release within the rate of pressure change term in Equation (3.11) [29]. It is assumed that the specific dissipation rate of the turbulent kinetic energy, ε, is uniform between the Reactant Zone and computational cell, while the treatment of external heat losses for the boundary cells, $\dot{Q}_{w,u}$, is handled by the Law of the Wall with parameters from the Reactant Zone state. In the current work, a chemical source term, $\dot{Q}^C_{u,AI}$, has also been added to account for auto-ignition within the Reactant Zone.

The Reactant Zone specific enthalpy can be found by considering the zone as a mixture of ideal gasses, where the enthalpy of each species is a function of the Reactant Zone temperature:

$$h_u = \frac{H_u}{m_u} = \sum_i Y_i^u h_{i,u} \tag{3.12}$$

In addition, a transport equation for the flame surface density Σ, the flame surface area per computational cell volume, is required for the calculation of the reaction front mass burning flux. The flame surface density is obtained through the solution of Equation (3.13) [29]:

$$\frac{\partial \rho \Sigma}{\partial t} + \frac{\partial \rho u_k \Sigma}{\partial x_k} = \frac{\partial}{\partial x_k}\left(\frac{\nu_t}{\sigma_\Sigma}\frac{\partial \rho \Sigma}{\partial x_k}\right) + \rho\left(S_1 + S_2 + S_3\right)\Sigma - \rho D \tag{3.13}$$

The two source terms in Equation (3.13) account for the flame surface density production through flame stretch induced by the mean flow (S_1) and aerodynamic straining of the reaction front by the eddies within the turbulent flow field (S_2). An additional source term S_3 is provided for spark ignition. This term is discussed further in Section 3.8. As with previous engine simulations, S_1 has been neglected in this work [26, 28, 29, 31], while S_2 is provided by the phenomenological Intermittent Turbulence Net Flame Stretch (ITNFS) model of Meneveau and Poinsot [11], which is frequently referred to as the CFM2 model [32].

The ITNFS model was developed through two-dimensional direct simulation of an initially laminar flame interacting with a flow through vortex pair. For a control volume proportional to the size of the vortex pair, the increase in heat release rate observed during the flame-vortex interaction was assumed to result from the surface area increase of the flame front produced by aerodynamic straining; this increase typically occurred in a near linear fashion with time. As a result, flame stretch was found by non-dimensionalizing the rate of change of the heat release rate with the initial, un-stretched value within the control volume. It was found that vortex pairs at the Kolmogorov scale, with their elevated levels of strain rate, had little effect on the surface area of the flame front because of their destruction by viscous dissipation during eddy turnover. A stretch efficiency function was developed to account for the fact that eddy strain was not always converted into flame stretch, especially at the smaller eddy length scales. Given that a range of length scales exist within a turbulent flow field, the average hydrodynamic flame stretch $\langle K \rangle$ was found by integrating over the range of turbulent length scales expected within the flow field, which was determined in part through turbulent flow measurements.

In addition, the ITNFS model includes a quenching model to replicate the quenching observed in the DNS. For sufficiently long eddy residence times, quenching was especially prevalent when thick flames propagated into conditions representative of

elevated turbulent intensity. The resulting quench times were noted to be comparable to the flame time, regardless of the eddy strain. The quench fraction of the flame front surface area was determined with the probability of successive eddies of the appropriate configuration interacting with a given location within the flame front over the quenching time.

Finally, Equation (3.13) includes a flame surface density destruction term, *D*. This term accounts for the destruction of flame surface area either by reactant consumption within the cell or through the merging/annihilation of adjacent flame fronts [32] observed in direct simulations [33].

The integration of Equations (3.5), (3.11) and (3.13) is performed with the standard KIVA-3V solution methodology, where the equations are discretized with respect to time and space and the contribution of each physical process to the scalar evolution is determined individually through operator splitting. The chemical source terms in Equation (3.3) - (3.5) and (3.11) and the external heat losses in Equations (3.4) and (3.11) are all calculated in Phase A. The effect of species mass and energy diffusion and boundary work is calculated in Phase B, while advection calculations are performed in Phase C. The transport equation solution approach described below builds upon the original formulation reported in [26], which was originally performed for non-reacting end and product gasses.

3.4 Homogeneous Reactor Modeling with the Multi-Zone Approach

Detailed chemical kinetics have been simulated with chemically controlled, homogeneous reactor models ranging from zero dimensional, single zone reactors to three dimensional CFD with detailed chemistry in each computational cell [34-38]. The detailed chemical mechanisms used in these simulations typically utilize hundreds to thousands of species with a similar number of reactions; it is well known that these

calculations are computationally expensive, especially when applied to large meshes [39]. A fully coupled Multi-Zone CFD model has been developed to reduce the expense of these computations by decreasing the number of chemical kinetic calculations without sacrificing accuracy [30].

In the current work, chemical kinetic calculations within a homogeneous reactor are performed using the fully coupled Multi-Zone approach [27, 30]. The essence of the Multi-Zone approach is the grouping of the computational cells, numbering in the thousands, into approximately 100 zones with similar thermodynamic states where the chemical kinetic calculations are performed. These zones differ from and are not to be confused with the Reactant and Product Zones. Each zone is treated as a constant volume homogeneous reactor initialized with information from the KIVA cells. The chemical kinetic calculations are performed within the reactor over the time step. At the end of the time step, the updated composition is passed from the reactor back to the respective KIVA computational cells during the remapping process. The cost savings of the multi-zone approach are realized by performing the kinetic calculations within the zones rather than the computational cells.

Within the original Multi-Zone formulation of Babajimopoulos [27], the computational cells are sorted and then grouped into zones based upon temperature and progress equivalence ratio, φ, defined in Equation (3.14).

$$\varphi = \frac{2C^{\#}_{-CO_2} + \frac{H^{\#}_{-H_2O}}{2} - \frac{zC^{\#}_{-CO_2}}{x}}{O^{\#}_{-CO_2-H_2O} - \frac{zC^{\#}_{-CO_2}}{x}} \tag{3.14}$$

Where $C^{\#}_{-CO_2}$, $H^{\#}_{-H_2O}$, and $O^{\#}_{-CO_2-H_2O}$ are the number of carbon, hydrogen and oxygen atoms within the cell, excluding the atoms in CO_2 and H_2O as indicated by the index, while *z/x* is the ratio of oxygen to carbon atoms within the fuel molecule, which is zero for non-oxygenated fuels. For lean mixtures, the progress equivalence ratio provides a

measure of reaction progress, ranging from the global equivalence ratio for no combustion, to zero for complete combustion.

The total number of carbon, hydrogen and oxygen atoms ($C^{\#}$, $H^{\#}$, and $O^{\#}$) in the computational cell are provided by Equations (3.15) - (3.17), where n_{tot} is the total number of molecules in the cell, m is the species index, c_m, h_m, o_m and n_m are the number of carbon, hydrogen, oxygen and nitrogen atoms in a molecule of species m, while x_m is the mole fraction of species m within the computational cell:

$$C^{\#} = n_{tot} \sum_i x_i c_i \tag{3.15}$$

$$H^{\#} = n_{tot} \sum_i x_i h_i \tag{3.16}$$

$$O^{\#} = n_{tot} \sum_i x_i o_i \tag{3.17}$$

The original Multi-Zone formulation was intended for lean mixtures only. Kodavasal noted that in some cases φ can overlap for mixtures with significantly different Φ, which is expected in systems employing stratification, such as Gasoline Direct Injection (GDI) engines [40]. In addition, it was noted that φ is invariant for stoichiometric mixtures, which are expected for both conventional SI and SACI engines diluted with EGR. To rectify these issues, the mass average internal energy of formation, u_f, was added by Kodavasal [40] as an additional level of reaction progress to the computational cell sorting and zoning routines.

With the new approach [40], the sorting of the computational cells into zones begins by arranging the computational cells from the lowest to highest temperature into temperature zones. The temperature zones are further divided so that the maximum temperature difference within the zone does not exceed 100 K, while the range of φ in the zone cannot exceed 0.05, and the range of $\log|u_f|$ within the zone cannot exceed 5% of

the total range of log| u_f | within the cylinder [40]. Zones containing more than 1% of the cylinder mass are further divided so that each zone contains a maximum of 1% of the cylinder's mass.

Using the average pressure, temperature and composition of the computational cells within the zone, chemical kinetic calculations are performed over the time step. At the end of the time step, the compositional change is remapped from the zone back to the computational cells in part through the variable *ch*, which represents the number of C and H atoms in a cell or zone, excluding CO_2 and H_2O:

$$ch = 2C^{\#}_{-CO_2} + \frac{H^{\#}_{-H_2O}}{2} \tag{3.18}$$

Aside from O_2, N_2 CO_2 and H_2O, the updated mass of species *m* within the computational cell is obtained through remapping with *ch*:

$$m_m = \frac{ch_{cell}}{ch_{zone}} m_{m,zone} \tag{3.19}$$

The updated O_2, N_2 CO_2 and H_2O masses are subsequently obtained from atom balances within the computational cell, ensuring that overall mass, elemental mass and atom conservation occurs within the cell. Further details on the multi-zone approach are provided in [27] and [40].

3.5 KIVA-3V Phase A SACI Combustion Model Derivation

The formulation of the sub-grid model for the combustion source terms in Equations (3.3)-(3.5) and (3.11) is now shown. The mass of species *m* within a KIVA-3V cell, m_m, is split into the Reactant and Product Zone masses, $m_{m,u}$ and $m_{m,b}$, with Equation (3.20) where the reaction front is assumed to be infinitely thin and of a negligible mass.

$$m_m = m_{m,u} + m_{m,b} \tag{3.20}$$

The species masses within the computational cell, Reactant Zone and Product Zones are found with Equations (3.21) – (3.23), where ρ_m^u and ρ_m^b are the Reactant and Product Zone species densities relative to their respective Reactant and Product Zone volumes, V_u and V_b:

$$m_m = \rho_m V \tag{3.21}$$

$$m_{m,u} = \rho_m^u V_u \tag{3.22}$$

$$m_{m,b} = \rho_m^b V_b \tag{3.23}$$

Differentiating Equation (3.20) with respect to time, the rate of change of the mass of species *m* within the computational cell is given by Equation (3.24), where:

$$\dot{m}_m = \dot{m}_{m,u} + \dot{m}_{m,b} \tag{3.24}$$

Applying the chain rule to Equations (3.21) – (3.23):

$$\dot{m}_m = \dot{\rho}_m V + \rho_m \dot{V} \tag{3.25}$$

$$\dot{m}_{m,u} = \dot{\rho}_m^u V_u + \rho_m^u \dot{V}_u \tag{3.26}$$

$$\dot{m}_{m,b} = \dot{\rho}_m^b V_b + \rho_m^b \dot{V}_b \tag{3.27}$$

Over the time step, the reaction front consumes a given mass of the Reactant Zone while producing an equivalent mass of the Product Zone within the computational cell. Assuming quasi-steady reaction front propagation, the rate of Reactant Zone mass consumption and corresponding Product Zone mass production is found with the mass burning flux, $\rho_u S_L$ and the surface area of the reaction front, ΣV, through Equation (3.28):

$$\dot{m}_b = -\dot{m}_u = \rho_u S_L \Sigma V \tag{3.28}$$

From Equation (3.28), the rate of change of the mass of species *m* within the Reactant and Product Zones due to reaction front propagation is given by Equations (3.29) and (3.30):

$$\rho_m^u \dot{V}_u = Y_m^u \dot{m}_u = -\rho_u Y_m^u S_L \Sigma V \tag{3.29}$$

$$\rho_m^b \dot{V}_b = Y_m^b \dot{m}_b = \rho_u Y_m^b S_L \Sigma V \tag{3.30}$$

Equation (3.31) is developed by substituting Equations (3.25) – (3.27) and (3.29) - (3.30) into Equation (3.24) while noting that the computational cell volume is constant during Phase A ($\dot{V} = 0$):

$$\dot{\rho}_m = \dot{\rho}_m^u \frac{V_u}{V} + \rho_u \left(Y_m^b - Y_m^u \right) S_L \Sigma + \dot{\rho}_m^b \frac{V_b}{V} \tag{3.31}$$

Applying the species density definition given by Equation (3.7) to the first and third terms on the RHS of Equation (3.31) yields Equation (3.32), where the superscript *C* (for chemistry) is included for consistency with KIVA-3V notation:

$$\dot{\rho}_m^C = \dot{\rho}_{m,u}^C + \rho_u \left(Y_m^b - Y_m^u \right) S_L \Sigma + \dot{\rho}_{m,b}^C \tag{3.32}$$

From Equation (3.31), it is clear that for cells containing reaction fronts, the chemistry update is performed for two constant volume, homogeneous reactors, where the first and third terms, $\dot{\rho}_{m,u}^C$ and $\dot{\rho}_{m,b}^C$, on the RHS are for the rate of species change within the Reactant and Product Zones. The middle term in the RHS of Equation (3.32) corresponds to the species consumed/produced by the reaction front, where:

$$\dot{\rho}_{m,RF}^C = \rho_u \left(Y_m^b - Y_m^u \right) S_L \Sigma \tag{3.33}$$

The resulting equation for the species change due to reaction front propagation, Equation (3.33), is of the same form as that initially proposed by Haworth et al. [41], and subsequently proposed by Tan and Reitz [42, 43].

In addition, a sink term is required for Equation (3.5) since the mass of the Reactant Zone is only consumed by the reaction front:

$$\dot{\rho}^{C}_{m,u,RF} = -\rho_u Y^u_m S_L \Sigma \tag{3.34}$$

3.6 KIVA-3V Phase A Chemistry Calculations

The flow diagram for the major CFMZ calculations is shown in Figure 3.2 with relative chapter sections highlighted in bold. As mentioned above, the chemistry, transport and convection calculations are performed separately through operator splitting in KIVA-3V.

The species density chemical source term of Equation (3.3), $\dot{\rho}^{C}_{m}$, is expanded in Equation (3.35) to include the contribution of the Reactant and Product Zones and the reaction front, $\dot{\rho}^{C}_{m,u}$, $\dot{\rho}^{C}_{m,b}$, and $\dot{\rho}^{C}_{m,RF}$, respectively, where:

$$\dot{\rho}^{C}_{m} = \dot{\rho}^{C}_{m,u} + \dot{\rho}^{C}_{m,RF} + \dot{\rho}^{C}_{m,b} \tag{3.35}$$

In the current approach, the KIVA-3V Phase A chemistry calculations can be performed within the Reactant Zone, the Product Zone and the reaction front. The compositional change within the computational cell from each chemistry calculation is subsequently applied to the computational cell. Those cells that have not been entrained by the reaction front only evaluate the $\dot{\rho}^{C}_{m,u}$ source term, while fully burned cells only evaluate the $\dot{\rho}^{C}_{m,b}$ source. Cells with reaction fronts evaluate all of the source terms in Equation (3.35).

In Phase A, the production and destruction of species through chemistry to Equation (3.3) is provided by Equation (3.36):

$$\left.\frac{d\rho Y_m}{dt}\right|_A = \dot{\rho}^{C}_{m} \tag{3.36}$$

In addition, the combustion source term, $\dot{Q}^C$, appearing in Equation (3.4) is expanded for the contribution of the zones and the reaction front:

$$\dot{Q}^C = \dot{Q}_u^C + \dot{Q}_{RF}^C + \dot{Q}_b^C \tag{3.37}$$

The contribution of chemistry in Phase A to the internal energy of the computational cell in Equation (3.4) is given by Equation (3.38):

$$\left.\frac{d\rho I}{dt}\right|_A = \dot{Q}^C \tag{3.38}$$

With the evaluation of the appropriate chemical source terms, the Phase A species densities of the computational cell, ρ_m^A, and internal energy, I^A, are effectively provided by time integration of the discretized forms of Equation (3.36) and (3.38).

From Figure 3.1, it is apparent that for those cells containing reaction fronts, that reaction front propagation conceptually begins at the border of the Product zone. As a result, the Product Zone species density source terms, $\dot{\rho}_{m,b}^C$, are first evaluated for burned gas chemistry with the Multi-Zone routine. The reaction front is then allowed to propagate in a quasi-steady manner into the Reactant Zone, consuming Reactant Zone and producing Product Zone species. The species density source terms for reaction front propagation are then determined for both the computational cell $\dot{\rho}_{m,RF}^C$ and the Reactant Zone, $\dot{\rho}_{m,u,RF}^C$. Finally, the source terms for the computational cell and the Reactant Zone due to auto-ignition within the Reactant Zone, $\dot{\rho}_{m,u}^C$ and $\dot{\rho}_{m,u,AI}^C$ respectively, are provided through an additional call to the Multi-Zone routine.

3.6.1 Application of the Multi-Zone Model to the Product Zone

The source term for the compositional change within the Product Zone in Equation (3.35), $\dot{\rho}_{m,b}^C$, is calculated with the Multi Zone model. During its evaluation in Phase A, the Product Zone is a control mass within the computational cell, therefore, the

rate of change in species mass within the computational cell is equivalent to that within the Product Zone, Equation (3.39):

$$\dot{\rho}_{m,b}^{C} = \frac{m_b}{V}\left(\frac{Y_m^{b,A} - Y_m^{b,n}}{\Delta t}\right) \tag{3.39}$$

Where $Y_m^{b,n}$ is the initial Product Zone mass fraction of species *m* from time step *n*, while $Y_m^{b,A}$ is the updated mass fraction of the Product Zone for Phase A returned from the Multi-Zone solution.

The Product Zone chemical source term for Equation (3.37) is obtained with the change in the internal energy of formation of the computational cell, where u_m^0 is the internal energy of formation of species *m* while the superscript *b,A* represents the provisionally updated computational cell state at the end of the Product Zone calculations:

$$\dot{Q}_b^C = -\rho\frac{\left(\sum_m Y_m u_m^0\right)^{b,A} - \left(\sum_m Y_m u_m^0\right)^{n}}{\Delta t} \tag{3.40}$$

The Product Zone calculations are performed only for those cells with $\bar{c}_1$ > 5%; this issue will be further discussed in Section 3.7. The progress variable $\bar{c}_1$ is calculated with Equation (3.41), which is a measure of the mass of the computational cell consumed by the reaction front:

$$\bar{c}_1 = \left(1 - \frac{m_u}{m_{cell}}\right) \tag{3.41}$$

A second reaction progress variable, $\bar{c}_2$, is defined according to Equation (3.42):

$$\bar{c}_2 = \left(\frac{h^0 - h_R^0}{h_P^0 - h_R^0}\right) \tag{3.42}$$

This progress variable uses the relative change in the enthalpy of formation of the computational cell, where h^0 is the current enthalpy of formation of the computational

cell, while the enthalpy of formation of the major product and reactant species, h_P^0 and h_R^0, are obtained from stoichiometry. These progress variables differ in that $\bar{c}_1$ is a measure of fraction of the computational cell mass consumed by the reaction front, while $\bar{c}_2$ is a measure of the total reaction progress within the cell. These progress variables are functionally equivalent when combustion occurs only by reaction front propagation but take on different meaning when auto-ignition occurs within the cell.

3.6.2 Reaction Front Modeling

The source term in Equation (3.35) for the production/destruction of species *m* within the computational cell due to reaction front propagation is given by Equation (3.43):

$$\dot{\rho}_{m,RF}^C = \rho_u \left(Y_m^{EQ} - Y_m^u \right) S_L \Sigma \tag{3.43}$$

The product species in Equation (3.43), (see also Equation (3.33)), Y_m^b, are modeled as constant pressure equilibrium products, Y_m^{EQ}, determined from calls to EQUIL using state information from the Reactant zone. The reaction front model is applied only to those cells where $\rho\Sigma$ is greater than 1.0e-10; below this value, the contribution of the front to the heat release within the cell was found to be negligible.

The change in the specific internal energy of the computational cell due to heat release from the reaction front, $\dot{Q}_{RF}^C$, in Equation (3.37) is given by Equation (3.44):

$$\dot{Q}_{RF}^C = -\rho \frac{\left(\sum_m Y_m u_m^0 \right)^{RF,A} - \left(\sum_m Y_m u_m^0 \right)^{b,A}}{\Delta t} \tag{3.44}$$

Where the superscript *RF,A* represents the provisionally updated computational cell state at the end of the Reaction Front calculations. Within the Reactant Zone, the specific enthalpy change due to compression from boundary work or heat release is

handled in Phase B by Equation (3.64); the cell pressure and h_u are assumed to remain constant during the quasi-steady front propagation process.

As mentioned above, given that the reaction front only consumes the Reactant Zone species, there is no species production by the front within this zone. The Reactant Zone species density destruction term for Equation (3.5) is provided by Equation (3.45) (See also Equation (3.34)):

$$\dot{\rho}^{C}_{m,u,RF} = -\rho_u Y^u_m S_L \Sigma \tag{3.45}$$

Equations (3.43) and (3.45) require the laminar burning velocity, S_L, which is calculated for an isooctane-air mixture with Equations (3.46) through (3.48) (Repeated from Chapter 2) using the constants given in [44], where:

$$S_L = F\left(Y^u_f\right)^M \exp\left(-G/T^0\right)\left(\frac{T_u}{T^0}\right)\left(\frac{T_b - T^0}{T_b - T_u}\right)^n \tag{3.46}$$

Equation (3.46) includes terms for Y^u_f, the fuel mass fraction in the Reactant Zone and the inner layer temperature, T^0, which is provided by Equation (3.47):

$$T^0 = \left(\frac{-E}{\ln\left(p/B\right)}\right)\left(Y^u_f + C_7\right)^{C_8} + C_9 T_u + a_1 p^{a_3}\left(\left(Y^u_f\right)^{a_2} - Y^{a_2}_{f,stoich}\right) \tag{3.47}$$

The adiabatic flame temperature, T_b, required by Equation (3.46) is calculated with Equation (3.48):

$$T_b = T_u + \Phi\left(c + d\Phi + e\Phi^2 + fT_u + gp\right) \tag{3.48}$$

Equation (3.48) does not include a reaction progress dependency; therefore, it is not appropriate for cases in which the Reactant Zone is undergoing auto-ignition. In this instance, Equation (3.48) is replaced with the adiabatic flame temperature obtained from EQUIL. During end-gas knock, the Reactant Zone fuel mass fraction, Y^u_f, which appears in Equation (3.46) and (3.47), rapidly approaches zero. The transient reaction front simulations in Chapter 2 showed that the fuel mass fraction term provides the burning

velocity's sensitivity to equivalence ratio, and that reasonable fronts speeds could be predicted by fixing this variable to that of a cold end-gas, for end-gas temperatures up to approximately 1100 K. During auto-ignition, Y_f^u is reconstructed to its initial, unburned value via stoichiometry. Beyond end-gas temperatures of 1100 K, however, the predicted burning velocities significantly exceeded those observed in the reaction front simulations. To prevent the over-prediction of front speeds while still capturing the effect of front propagation, Equation (3.46) uses the smaller of T_u or 1100 K.

The final term appearing in Equations (3.43) and (3.45) is the flame surface density, Σ. The methodology for updating the flame surface density during Phase A is largely unchanged from [26], where the flame surface density transport equation, Equation (3.49) includes source terms for stretch, S, and a sink term for flame surface destruction due to flamelet merging/annihilation, D.

$$\frac{d\rho\Sigma}{dt} = \rho\left(S_1 + S_2 + S_3\right)\Sigma - \rho D \tag{3.49}$$

As mentioned previously, the two source terms in Equation (3.49), S_1 and S_2, model flame surface density production by stretch induced by the mean flow (S_1) and by the aerodynamic straining of the reaction front by the turbulent flow field (S_2). S_1 has been neglected in this work, while S_2 is provided by the Intermittent Turbulence Net Flame Stretch (ITNFS) model of Meneveau and Poinsot [11]. Consistent with Vanzieleghem [26], the source and destruction terms S_2 and D of Equation (3.49) are calculated once the ignition kernel has reached the size where it is wrinkled by the turbulent flow field. Prior to this point, during the spark ignition event and laminar flame kernel development, the flame surface density production in the ignition cell is modeled with S_3, which represents the laminar growth of the ignition kernel. The transition from the laminar ignition model (S_3) to the turbulent flame model (S_2 and D)is described in more detail in Section 3.8.

To determine S_2 resulting from the net flame stretch, $\bar{K}$, the phenomenological ITNFS model uses the turbulent dissipation rate, ε, the turbulent kinetic energy, k, the RMS turbulent velocity, u', the laminar flame speed S_L, the integral length scale, L, and the laminar flame thickness, δ:

$$\frac{\bar{K}}{\varepsilon / k} = f\left(\frac{u'}{S_L}, \frac{L}{\delta}\right) \tag{3.50}$$

Where the RMS turbulent velocity, u', is given by Equation (3.51):

$$u' = \left(\frac{2k}{3}\right)^{1/2} \tag{3.51}$$

The integral length scale is provided by Equation (3.52), where C_D is a model constant ranging from 0.380 to 0.393 for the k-epsilon and RNG k-epsilon models, respectively:

$$L = C_D \frac{k^{3/2}}{\varepsilon} \tag{3.52}$$

The flame thickness, δ, required by Equation (3.50) is provided by Equation (3.53), using the fit parameters from [44] and T_b, T^0 and S_L, determined from Equations (3.46) - (3.48). Equation (3.53) includes l_F, given by Equation (3.54), and an expression for the ratio of mixture thermal conductivity to heat capacity, given by Equation (3.55).

$$\delta = c_f \frac{T_b - T_u}{T^0 - T_u} l_F \tag{3.53}$$

$$l_F = \frac{\left(\lambda / c_p\right)\Big|_{T^0}}{\rho_u S_L} \tag{3.54}$$

$$\lambda / c_p = 2.58 \times 10^{-5} \left(T / 298\ K\right)^{0.7}\ kg/m-s \tag{3.55}$$

The non-dimensionalized net flame stretch, $\Gamma_{\bar{K}}$ is provided by the ITNFS model, Equation (3.56), while the full set of equations for this model is provided in [32].

$$\Gamma_{\bar{K}} = \frac{\bar{K}}{\varepsilon / k} = \frac{\langle K \rangle}{\varepsilon / k} - \frac{3}{2}\left(\frac{L}{\delta}\right)\left(\frac{S_L}{u'}\right)\ln\left(\frac{1}{1-P_q}\right) \tag{3.56}$$

The non-dimensionalization of $\bar{K}$ in Equation (3.56) is performed with the large scale eddy strain, ε / k. The first term on the R.H.S. of Equation (3.56) is for the total aerodynamic stretch, $\langle K \rangle$, while the second term represents the effect of flame quenching, which attenuates the net flame stretch.

Finally, the flame surface density source term for the net aerodynamic flame stretch, S_2, is calculated with Equation (3.57), where α_0 is an adjustable constant:

$$S_2 = \alpha_0 \Gamma_{\bar{K}} \frac{\varepsilon}{k} \tag{3.57}$$

The flame surface density destruction terms in Equation (3.49) can either be provided by the CFM-2a model, Equation (3.58) or CFM-2b model, Equation (3.59):

$$D = \beta_0 \frac{S_L + Ck^{1/2}}{1-\bar{c}} \Sigma^2 \tag{3.58}$$

$$D = \beta_0 \frac{S_L + Ck^{1/2}}{\bar{c}\left(1-\bar{c}\right)} \Sigma^2 \tag{3.59}$$

Where β_0 and C are model constants and $\bar{c}$ is reaction progress from either Equation (3.41) or (3.42).

To improve upon the predictions made with the original Reactant zone transport equations, a small mass of each Reactant zone species is left in the computational cell by preventing the complete consumption of the Reactant Zone by the reaction front. This step prevents significant Reactant Zone state errors while facilitating accurate predictions in the event that Reactant Zone species advect back into a given computational cell. Trace reactant zone species are maintained by adjusting the time steps of Equations (3.43) and (3.45) so that the reaction progress predicted by Equation (3.41) does not exceed 0.999.

3.6.3 Application of the Multi-Zone Model to the Reactant Zone

After modeling the reaction front propagation and updating the Reactant Zone mass in part through Equation (3.45), the compositional change within the computational cell due to auto-ignition within the Reactant Zone is calculated with the updated Reactant Zone state returned from the Multi-Zone code, given that the Reactant Zone is a control mass within the computational cell during Phase A. As a result, the change in species mass *m* within the computational cell is equivalent to that within the Reactant Zone. The final species density source term for Equation (3.35), representing the species change within the Reactant Zone, $\dot{\rho}_{m,u}^{C}$, is obtained from Equation (3.60):

$$\dot{\rho}_{m,u}^{C} = \frac{m_u}{V}\left(\frac{Y_m^{u,A} - Y_m^{u,n}}{\Delta t}\right) \tag{3.60}$$

Where $Y_m^{u,A}$ and $Y_m^{u,n}$ are the mass fraction of species *m* within the Reactant Zone, relative to the Reactant Zone mass, at the end of the Reactant Zone Phase A and from the previous time step *n*. This last provisional update of the computational cell provides the cell's final Phase A composition. The final specific internal energy source term in Equation (3.37) is provided by the compositional change within the Reactant Zone, Equation (3.61):

$$\dot{Q}_u^C = -\rho\frac{\left(\sum_m Y_m u_m^0\right)^A - \left(\sum_m Y_m u_m^0\right)^{RF,A}}{\Delta t} \tag{3.61}$$

The Reactant Zone species density chemical source term in Equation (3.5), $\dot{\rho}_{m,u,AI}^{C}$, is provided from the updated Reactant Zone mass fractions returned from the Multi-Zone model. The Reactant Zone enthalpy is updated for the heat release due to auto-ignition through time integration of Equation (3.62), where the chemical source term, $\dot{Q}_{u,AI}^{C}$, is calculated in part with the enthalpy of formation for species m, h_m^0 with Equation (3.63):

$$\frac{d\rho h_u}{dt} = \dot{Q}^C_{u,AI} \tag{3.62}$$

$$\dot{Q}^C_{u,AI} = -\rho \frac{\left(\sum_m Y^u_m h^0_m\right)^A - \left(\sum_m Y^u_m h^0_m\right)^n}{\Delta t} \tag{3.63}$$

Where Y^u_m are the mass fractions of species *m* within the Reactant Zone, calculated relative to the Reactant Zone mass, while the superscript *A* refers to information from the end of the current time step, while *n* refers to information from the previous time step.

3.7 KIVA-3V Phase B and Phase C Calculations

Phase B calculations are performed at the conclusion of Phase A. In Phase B, turbulent transport is modeled according to Fick's Law with a turbulent diffusivity. The transport terms in Equations (3.5), (3.11) and (3.13) are solved accordingly, using the standard KIVA-3V Phase B algorithm.

Similar to the specific internal energy of the computational cell, the Reactant Zone enthalpy is updated for the pressure changes resulting from boundary work and heat release at the end of Phase B with Equation (3.64):

$$\frac{dh_u}{dt} = \frac{1}{\rho_u}\frac{dp}{dt} \tag{3.64}$$

Given that h_u and ρ_u are intensive properties and that the composition and pressure of the Reactant Zone have been updated in Phase B, h^B_u, the Reactant Zone enthalpy at the end of Phase B, is obtained by discretizing Equation (3.64), substituting the equation of state arranged for ρ_u, Equation (3.65), and inverting Equation (3.66) for T_u, where:

$$\rho_u = \frac{p}{R_u T_u} \tag{3.65}$$

$$h_u^B = h_u^n + \left(\frac{R_u T_u}{p} \right)^B \left(p^B - p^n \right) \tag{3.66}$$

The Reactant Zone species densities, enthalpy and the flame surface density are then updated for advection in Phase C. At the end of Phase C, the Reactant Zone temperature is obtained again by inverting the enthalpy equation using the standard KIVA-3V approach. This state serves as the initial Reactant Zone state for the Phase A chemistry update at the next time step.

With the computational cell and Reactant Zone states fixed at the end of Phase C, the state of the Product Zone is determined. A separate set of transport equations is not required for the Product Zone as this state is obtained directly through mass and energy balances. As the mass of species *m* within the computational cell and Reactant Zone are known, the mass of species *m* within the Product Zone, $m_{m,b}$, is obtained through continuity, assuming that the flamelet is infinitely thin:

$$m_{m,b} = m_m - m_{m,u} \tag{3.67}$$

The mass of the Product Zone is obtained with Equation (3.68):

$$m_b = \sum_i m_{i,b} \tag{3.68}$$

The specific internal energy of the Product zone, u_b, is then obtained through manipulation of the cell and zone properties with Equation (3.69):

$$u_b = \frac{mu \; - m_u u_u}{m_b} \tag{3.69}$$

With its composition and energy now known, the temperature of the Product Zone is determined. To prevent stability issues for cells with near zero Product Zone masses, the temperature update and Phase A Product Zone chemistry is only performed when reaction progress ($_1$) given by Equation (3.41) is greater than 5%.

3.8 Spark-Ignition Modeling

Prior to the spark-ignition event, there are no reaction fronts present within the combustion chamber and only the Reactant zone combustion model is active for the end-gas chemistry. At the specified time of spark ignition, the ignition model is called to initialize the Σ transport equation. The original ignition model in [26] has been modified to include the effect of the spark energy deposition on the initial ignition kernel growth rate.

From observations in optical engine experiments [45], the ignition kernel is assumed to be spherical and laminar, with an initial radius of 0.5 mm. The kernel radius, r_k, grows spherically at the combination of the laminar flame speed and the effective plasma velocity, S_p, where:

$$\frac{dr_k}{dt} = \frac{\rho_u}{\rho_b}\left(S_L + S_p\right) \tag{3.70}$$

The effective plasma velocity, S_p, is calculated with a thermodynamic model from [43] using Equation (3.71):

$$S_p = \frac{\dot{Q}_{spk}\eta_{eff}}{4\pi r_k^2\left[\rho_u\left(u_b - h_u\right) + p\frac{\rho_u}{\rho_b}\right]} \tag{3.71}$$

This equation requires the instantaneous electrical power input into the spark plug, $\dot{Q}_{spk}$, which is assumed to be applied uniformly to the kernel over the span of the spark energy deposition period. The efficiency of the ignition energy transfer to the gas within the ignition cell, η_{eff}, is assumed to be 30%, while the specific internal energy of the burned gasses within the ignition kernel, u_b, is evaluated at the adiabatic flame temperature.

During ignition, Equation (3.70) is integrated in time to provide the updated spark kernel radius. In turn, the flame surface density source term of the ignition cell, S_3, is calculated with Equation (3.72), where:

$$S_3 = \frac{4\pi r_k^2}{V} \tag{3.72}$$

During ignition, the only source term applied to Equation (3.49) is from Equation (3.72); the source term S_1 and destruction term D are only applied after the ignition kernel reaches a size when it is affected by turbulent flow field. The laminar ignition model and source term S_3 are kept active up to the point in the cycle when the flame kernel radius exceeds 2 mm. This is consistent with the Coherent Flamelet ignition model of Falfari and Bianchi [46] and with the experimental observations of Herweg and Maly [45], where the ignition kernel becomes wrinkled by the turbulent flow field once its radius is approximately 2 mm [45]. Beyond this radius, the transition is made to the turbulent flame stretch model, updating Equation (3.49) with both S_1 and D. The transition to the turbulent combustion model may also occur when the ignition cell is completely burned or when the ignition kernel radius is on the order of the integral length scale [26, 43].

3.9 Flame Surface Density Wall Functions

Flame wall interaction is modeled with the Flame Interacting with Surface and Turbulence (FIST) approach of Poinsot et al. [47]. This is a modification of the original flame surface density implementation in [26], which was modeled using the approach of Duclos et al. [31].

The FIST model was developed to correct the elevated, non-physical flame surface densities observed near the combustion chamber boundaries during SI combustion simulations with the Coherent Flamelet model [47]. The FIST model was formulated by examining the effects of flame-wall distance on the local and global flame structure with turbulent, two dimensional direct simulation. Two effects are included

within the model, flame quenching resulting from heat losses to the combustion chamber boundaries and flame laminarization as the turbulent flame approaches the wall.

The flame quench model was formulated based upon the flame quenching observed within the direct simulations, which occurred only when the flame was in close proximity to the wall, in an area called the influence zone. Within the influence zone, which is on the order of a laminar flame thickness, the flame was noted to quench once the residence time within this zone exceeded two laminar flame times.

The flame laminarization model was proposed for the inhibition zone, where turbulence is attenuated by viscous forces and the flame takes on a laminar structure. This model is not based upon the DNS results but rather on the fact that viscous forces dominate flows near the wall. An inhibition zone thickness estimate of 50 laminar flame thicknesses provided reasonable flame surface density behavior near the wall from simulations with the FIST model implemented in KIVA-3V.

The flame surface density transport equation of the wall cells is updated with Equation (3.73), where the first term on the RHS represents the flame surface density destruction due to thermal quenching, while the second term on the RHS represents the flame surface density destruction due to laminarization within the inhibition zone.

$$\frac{d\Sigma}{dt} = -\frac{\delta_T}{\Delta y}\left(\frac{a_Q}{a_Q+1}\right)\frac{\Sigma}{t_Q} + S\left(1-\frac{y_{in}}{\Delta y}\right) \tag{3.73}$$

The influence zone thickness, δ_T, is given by Equation (3.74):

$$\delta_T = (Pe)\,\delta \tag{3.74}$$

Where *Pe* is the Peclet number, assumed to be 10 in this case, δ is the un-stretched laminar flame thickness, Δy is the cell thickness, normal to the wall, *S* is the flame surface density production rate due to turbulent stretch and y_{in} is the inhibition zone thickness, taken as 50 flame thicknesses. The term a_Q is given by Equation (3.75):

$$a_Q = E \frac{\nu_T}{Sc} \frac{t_Q}{\delta_T^{\,2}} \tag{3.75}$$

Where E is a modeling constant, set to 1, v_T is the turbulent diffusivity, Sc is the turbulent Schmidt number, and t_Q is the quenching timescale, modeled as two flame times for a laminar flame.

3.10 Blowby Model

Blowby can have a significant effect on the trapped mass within an engine cylinder, especially for optical engines where ring sealing can be problematic. Therefore, a simple blowby model was implemented into KIVA-3V, where the blowby cells are defined as those cells with boundaries at both the piston crown and cylinder wall.

From Equation (3.76), the model assumes choked flow through an effective throat area when calculating the blowby mass flowrate, $\dot{m}_{bb}$:

$$\dot{m}_{bb} = \frac{A_{eff}\, p_0}{\sqrt{RT_0}} \gamma^{1/2} \left(\frac{2}{\gamma+1} \right)^{\frac{\gamma+1}{2(\gamma-1)}} \tag{3.76}$$

Where A_{eff} is the effective blowby area per computational cell, p_0 and T_0 are the stagnation pressure and temperature and γ is the ratio of specific heats. The stagnation temperature and pressure are obtained for an isentropic, sonic flow with Equations (3.77) and (3.78):

$$T_0 = T\left(1+\frac{\gamma-1}{2}\right) \tag{3.77}$$

$$p_0 = p\left(1+\frac{\gamma-1}{2}\right)^{\frac{\gamma}{\gamma-1}} \tag{3.78}$$

The effective area per blowby cell is calculated from the total effective blowby area using the ratio of the cell volume to the total volume of the blowby cells. The total effective

area is a tunable constant which can be obtained by matching experimental motoring pressure traces.

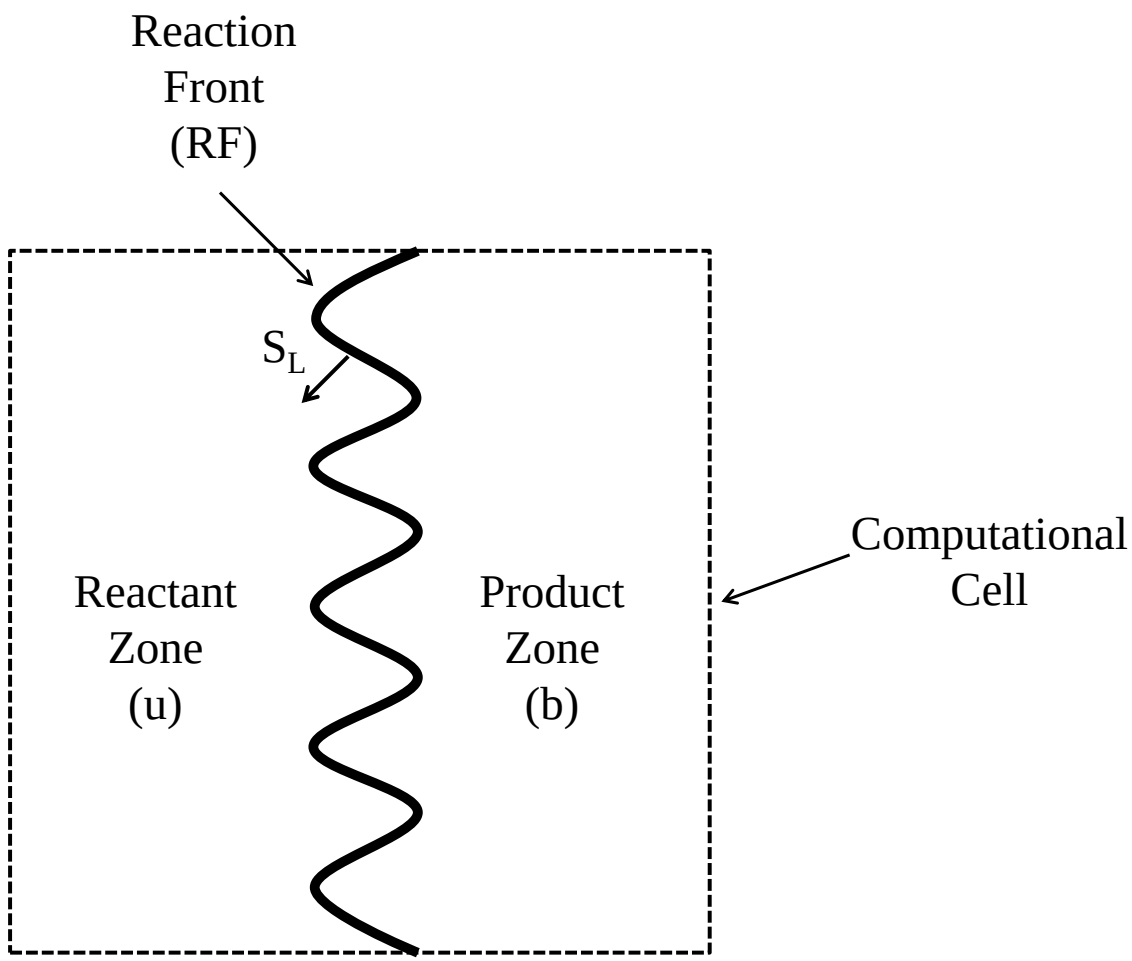

Figure 3.1: Conceptual CFMZ Model

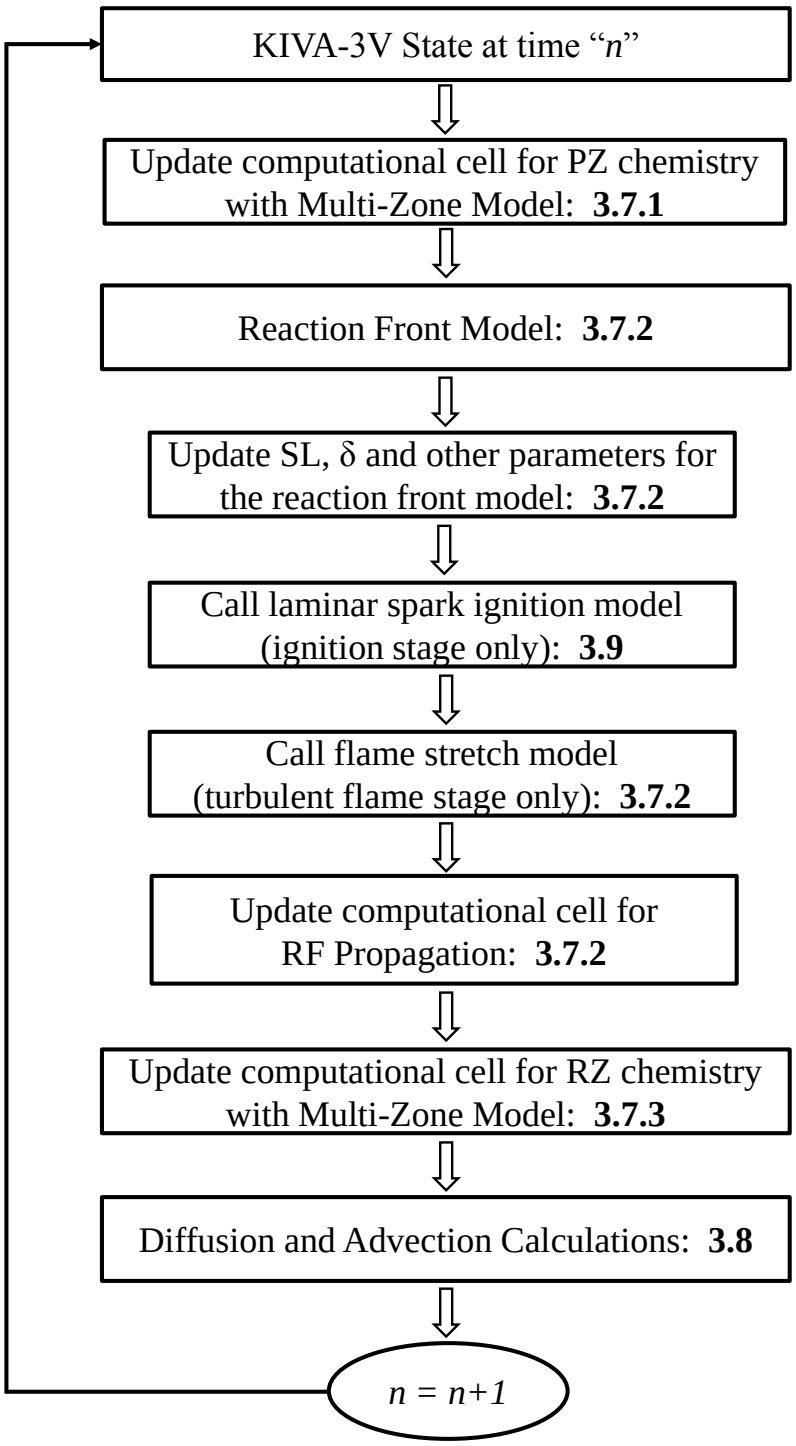

Figure 3.2: Flow Diagram for Major CFMZ Calculations, with discussion location in bold.

3.11 References

1. Lavoie, G., Martz, J., Wooldridge, M., and Assanis, D., "A Multi-Mode Combustion Diagram for Spark Assisted Compression Ignition," *Combustion and Flame,* Vol. 157: 1106-1110, 2010.

2. Persson, H., Hultqvist, A., Johansson, B., and Remon, A., "Investigation of the Early Flame Development in Spark-Assisted HCCI Combustion Using High-Speed Chemiluminescence Imaging," SAE Paper 2007-01-0212, 2007.

3. Reuss, D.L., Kuo, T., Silvas, G., Natarajan, V., and Sick, V., "Experimental Metrics for Identifying Origins of Combustion Variability During Spark-Assisted Compression Ignition," *International Journal of Engine Research,* Vol. 9: 409-434, 2008.

4. Zigler, B., *An Experimental Investigation of the Properties of Low Temperature Combustion in an Optical Engine,* Ph.D. Thesis University of Michigan, Ann Arbor (2008).

5. Noguchi, M., Tanaka, Y., Tanaka, T., and Takeuchi, Y., "A Study on Gasoline Engine Combustion by Observation of Intermediate Reactive Products during Combustion," SAE Paper 790840, 1979.

6. Onishi, S., Jo, S.H., Shoda, K., Jo, P.D., and Kato, S., "Active Thermo-Atmosphere Combustion (ATAC) - A New Combustion Process for Internal Combustion Engines," SAE Paper 790501, 1979.

7. Hultquvist, A., Christensen, M., Johansson, B., Richter, M., Nygren, J., Hult, J., and Alden, M., "The HCCI Combustion Process in a Single Cycle - High-Speed Fuel Tracer LIF and Chemiluminescence Imaging," SAE Paper 2002-01-0424, 2002.

8. Zigler, B., Walton, S., He, X., Wiswall, J., Wooldridge, M., and Wooldridge, S., "Crank-Angle Resolved Imaging of Homogeneous Charge Compression Ignition Phenomena in a Single-Cylinder Research Engine," *Proceedings of the 2006 Technical Meeting of the Central States Section of The Combustion Institute,* Cleveland, OH, 2006.

9. Schiessl, R., Dreizler, A., Maas, U., Grant, A., and Ewart, P., "Double-Pulse PLIF Imaging of Self-Ignition Centers in an SI Engine," SAE Paper 2001-01-1925, 2001.

10. Veynante, D. and Vervisch, L., "Turbulent Combustion Modeling," Progress in Energy and Combustion Science, Vol. 28: 192-266, 2002.

11. Meneveau, C. and Poinsot, T., "Stretching and Quenching of Flamelets in Premixed Turbulent Combustion," *Combustion and Flame*, Vol. 86: 311-332, 1991.

12. Driscoll, J., "Turbulent Premixed Combustion: Flamelet Structure and Its Effect on Turbulent Burning Velocities," *Progress in Energy and Combustion Science*, Vol. 34: 91-134, 2008.

13. Law, C., 2006. *Combustion Physics*. Cambridge University Press, New York.

14. Bell, J.B., Day, M.S., and Grcar, J.F., "Numerical Simulation of Premixed Turbulent Methane Combustion," *Proceedings of the Combustion Institute 29*: 1987-1993, 2002.

15. Hawkes, E.R., and Chen, J.H., "Comparison of Direct Numerical Simulation of Lean Premixed Methane-Air Flames with Strained Laminar Flame Calculations," *Combustion and Flame*, Vol. 144: 112-125, 2006.

16. Peters, N., "The Turbulent Burning Velocity for Large-Scale and Small-Scale Turbulence," *Journal of Fluid Mechanics*, Vol. 384: 107-132, 1999.

17. Law, C.K., Sung, C.J., Yu, G., and Axelbaum, R.L., "On the Structural Sensitivity of Purely Strained Planar Premixed Flames to Strain Rate Variations," *Combustion and Flame*, Vol. 98: 139-154, 1994.

18. Law, C.K., and Sung, C.J., "Structure, Aerodynamics, and Geometry of Premixed Flamelets," *Progress in Energy and Combustion Science*, Vol. 26: 459-505, 2000.

19. Rutland, C.J., and Trouve, A., "Direct Simulations of Premixed Turbulent Flames with Nonunity Lewis Numbers," *Combustion and Flame*, Vol. 94: 41-57, 1992.

20. Lipatnikov, A.N. and Chomiak, J., "Molecular Transport Effects on Turbulent Flame Propagation and Structure," *Progress in Energy and Combustion Science*, Vol. 31: 1-73, 2005.

21. Abu-Orf, G.M., and Cant, R.S., "A Turbulent Reaction Rate Model for Premixed Turbulent Combustion in Spark-Ignition Engines," *Combustion and Flame*, Vol. 122: 233-252, 2000.

22. Poinsot, T., Candel, S., and Trouve, A., "Applications of Direct Numerical Simulation to Premixed Turbulent Combustion," *Progress in Energy and Combustion Science*, Vol. 21: 531-576, 1996.

23. Poinsot, T., Veynante, D., and Candel, S., "Quenching Processes and Premixed Turbulent Combustion Diagrams," *Journal of Fluid Mechanics*, Vol. 228: 561-606, 1991.

24. Roberts, W., Driscoll, J., Drake, M., and Goss, L., "Images of the Quenching of a Flame by a Vortex - To Quantify Regimes of Turbulent Combustion," *Combustion and Flame*, Vol. 94: 58-69, 1993.

25. Peters, N., *Turbulent Combustion*, 2000. Cambridge University Press, New York.

26. Vanzieleghem, B.V., *Combustion Modeling for Gasoline Direct Injection Engines Using KIVA-3V*, Ph.D. Thesis University of Michigan, Ann Arbor (2004).

27. Babajimopoulos, A., *Development of Sequential and Fully Integrated CFD/Multi-Zone Models with Detailed Chemical Kinetics for the Simulation of HCCI Engines*, Ph.D. Thesis University of Michigan, Ann Arbor (2005).

28. Boudier, P., Henriot, S., Poinsot, T., and Baritaud, T., "A Model for Turbulent Flame Ignition and Propagation in Spark Ignition Engines," *Proceedings of the Twenty-Fourth International Symposium on Combustion:* 503-510, 1992.

29. Baritaud, T., Duclos, J., and Fusco, A., "Modeling Turbulent Combustion and Pollutant Formation in Stratified Charge Engines," *Proceedings of the Twenty-Sixth International Symposium on Combustion*: 2627-2635, 1996.

30. Babajimopoulos, A., Assanis, D., Flowers, D., and Hessel, R., "A Fully Coupled Computational Fluid Dynamics and Multi-Zone Model with Detailed Chemical Kinetics for the Simulation of Premixed Charge Compression Ignition Engines," *International Journal of Engine Research*, Vol. 6: 497-512, 2005.

31. Duclos, J.M., Bruneaux, G., and Baritaud, T.A., "3D Modeling of Combustion and Pollutants in a 4-Valve SI Engine; Effect of Fuel and Residuals Distribution and Spark Location," SAE Paper 961964, 1996.

32. Duclos, J., Veynante, D., and Poinsot, T., "A Comparison of Flamelet Models for Premixed Turbulent Combustion," *Combustion and Flame*, Vol. 95: 101-117, 1993.

33. Filatyev, S.A., Driscoll, J.F., Carter, C.D., and Donbar, J.M., "Measured Properties of Turbulent Premixed Flames for Model Assessment, Including Burning Velocities, Stretch Rates, and Surface Densities," *Combustion and Flame*, Vol. 141: 1-21, 2005.

34. Fiveland, S.B. and Assanis, D., "Development of a Two-Zone HCCI Combustion Model Accounting for Boundary Layer Effects," SAE Paper 2001-01-1028, 2001.

35. Fiveland, S.B. and Assanis, D.N., "Development and Validation of a Quasi-Dimensional Model for HCCI Engine Performance and Emissions Studies Under Turbocharged Conditions," SAE Paper 2002-01-1757, 2002.

36. Agarwal, A. and Assanis, D., "Multi-Dimensional Modeling of Natural Gas Ignition Under Compression Ignition Conditions Using Detailed Chemistry," SAE Paper 980136, 1998.

37. Agarwal, A. and Assanis, D., "Multi-Dimensional Modeling of Natural Gas Autoignition Using Detailed Chemical Kinetics," *Combustion Science and Technology*, Vol. 163: 177-210, 2001.

38. Ogink, R. and Golovichev, V., "Gasoline HCCI Modeling: Computer Program Combining Detailed Chemistry and Gas Exchange Processes," SAE Paper 2001-01-3614, 2001.

39. Aceves, S., Martinez-Frias, J., Flowers, D., Smith, J.R., Dibble, R., and Chen, J., "A Computer Generated Reduced Iso-Octane Chemical Kinetic Mechanism Applied to Simulation of HCCI Combustion," SAE Paper 2002-01-2870, 2002.

40. Kodavasal, J., *An Improved Multi-Zone Combustion Model for PCCI Simulation*, M.S. Thesis University of Michigan, Ann Arbor (2010).

41. Haworth, D.C. and Poinsot, T.J., "Numerical Simulations of Lewis Number Effects in Turbulent Premixed Flames," *Journal of Fluid Mechanics*, Vol. 244: 405-436, 1992.

42. Tan, Z. and Reitz, R.D., "Modeling Ignition and Combustion in Spark-Ignition Engines Using a Level Set Method," SAE Paper 2003-01-0722, 2003.

43. Tan, Z. and Reitz, R.D., "An Ignition and Combustion Model Based on the Level-Set Method for Spark Ignition Engine Multidimensional Modeling," *Combustion and Flame*, Vol. 145: 1-15, 2006.

44. Martz, J.B., Middleton, R.J., Lavoie, G.A., Babajimopoulos, A., and Assanis, D.N., "A Computational Study and Correlation of Premixed Isooctane-Air Laminar Flame Properties under Spark Ignited and Spark Assisted Compression Ignition Engine Condition," *Accepted Combustion and Flame*, 2010.

45. Herweg, R., and Maly, R.R., "A Fundamental Model for Flame Kernel Formation in S.I. Engines," SAE Paper 922243, 1992.

46. Falfari, S., and Bianchi, G.M., "Development of an Ignition Model for S.I. Engines Simulation," SAE Paper 2007-01-0148, 2007.

47. Poinsot, T.J., Haworth, D.C., and Bruneaux, G., "Direct Simulation and Modeling of Flame-Wall Interaction for Premixed Turbulent Combustion," *Combustion and Flame*, Vol. 95: 118-132, 1993.

CHAPTER 4

COMPARISON OF THE KIVA-CFMZ MODEL WITH ENGINE EXPERIMENTS

Two different sets of experimental SI and SACI data were used to evaluate the performance of the KIVA-CFMZ model. This evaluation serves as a first test for the sub-grid model formulation from Chapter 3 and the laminar reaction front simulation correlations described in Chapter 2. In the following sections, the particulars of the experimental setups modeled with KIVA-CFMZ are described. Then, KIVA-CFMZ is compared to SI data in order to establish the flame model constants and to gauge the model's predictive capabilities against relatively mature, high temperature combustion concepts. Finally, KIVA-CFMZ simulation results are compared to optical SACI engine data to assess the model's capability under low temperature combustion conditions. Additional insight into SACI combustion is then developed through analysis of the model results.

4.1 Metal SI Engine Experimental Setup

KIVA-CFMZ was compared to SI combustion data from the metal engine experiments of Bohac [1] in part to provide a baseline comparison relative to well established, current production combustion processes. The engine used in these experiments was a 1998 model year 2.5 L, six cylinder Ford Duratec port fuel injected (PFI) SI engine, with a four valve, pent-roof cylinder head and a centrally mounted spark plug. Key engine parameters are provided in Table 4.1. To increase swirl and turbulence

levels within the cylinder at low engine speeds, one of each cylinder's twin intake runners was equipped with a butterfly valve which was closed at engine speeds below 3500 RPM. These valves were closed under all of the conditions modeled in this work.

4.2 Optical SACI Engine Experimental Setup

KIVA-CFMZ was also compared to images and data from the optical SACI engine experiments of Zigler [2]. These experiments were selected because of the fundamental, physical insight provided by the images, which show both reaction front propagation and auto-ignition during SACI combustion. These images provide a basis for judging the physicality of the KIVA-CFMZ model predictions.

Key engine design parameters of the PFI single cylinder optical engine are included in Table 4.2. The combustion chamber design of this engine includes a four valve, pent-roof 1.25L Ford Zetec-SE cylinder head with a centrally mounted spark plug. One cylinder of the four cylinder head is used with a steel cylinder liner and a flat top, Bowditch piston with Torlon rings and a 48.5 mm viewing window for line of sight imaging relative to the firing deck plane through the piston crown. The engine speed was held constant at 700 RPM with a hydraulic dynamometer capable of both motoring and absorbing load. The throttle position was held constant near wide open throttle (WOT), while intake air temperature (IMAT) was controlled with an electric heater. Equivalence ratio was measured with an ETAS LA4 lambda sensor and was maintained by varying the pulse width of the port fuel injector. Jacket water temperatures were maintained at 90° C, while lubricating oil temperatures were set at 60° C during the experiments. High speed, line of sight photographs of unfiltered, visible chemiluminescence were obtained through the piston crown viewport for the images used in this work. The observed blue chemiluminescence was attributed to either CH or C_2 radical species formed within high

temperature reaction zones, as the camera's spectral response made carbon monoxide imaging unlikely [2].

4.3 The Computational Mesh

The exact geometry of both engine combustion chambers was not available at the time of this study. Representative meshes with the same key features of both engines, including complex pent roof shapes and flat top pistons, were therefore adopted. Closed cycle CFMZ simulations were performed with the approximately 90000 cell mesh, shown configured for the optical engine in

Figure 4.1. The bore and stroke of an existing KIVA-3V pentroof mesh was scaled so that the bore and stroke of the adopted mesh were identical to those of the experiments, while the experimental compression ratio was maintained by adjusting the squish height of the adopted mesh. Initial simulations of the optical engine predicted peak, non-firing cylinder pressures in excess of those measured in the experiments. The blowby model given by Equations 3.76 through 3.78 was used in the optical engine simulations to attenuate simulated peak cylinder pressures to levels in line with those observed from the experiments.

4.4 Comparison of Simulated and Experimental SI Results

The SI combustion cases simulated with KIVA-CFMZ are listed in Table 4.3. These conditions include engine speed, equivalence ratio and timing sweeps at different engine loads. The closed cycle KIVA-CFMZ simulations of these cases were initialized with the experimental cylinder pressure at IVC, while the temperature at IVC was calculated with the equation of state using the measured trapped mass. The piston, wall and head temperatures were comparable to those used by Bohac for quasi-dimensional SI modeling of this engine [1].

The main tuning constant of the Coherent Flamelet model, α_0 in Equation 3.57, was set to 1.9 based upon the initial KIVA-CFMZ SI simulation results. This value closely corresponds to the values of 1.6 [3], 1.8 [4] to 2.1 [5] reported from previous engine studies. Consistent with the form reported in previous studies [3, 4, 6], the CFM-2a flame surface density destruction term, Equation 3.58, was adopted for this work, while reaction progress appearing in the destruction term was calculated from Equation 3.42. In addition, the terms β_0 and C appearing in Equation 3.58 have been typically assigned values of unity [3, 5] and 0 [3, 4], respectively; these values were maintained throughout the KIVA-CFMZ simulations. Key input values used for the simulations are included in Table 4.4. A 10 species iso-octane equilibrium mechanism was used to obtain the compositional change across the reaction front and for the simulation of the product gasses for these runs. The energy input to the spark plug was assumed to be 61 mJ, with 30% of the energy input deposited to the ignition cell gas mixture over a spark duration of 1.5 ms. These values are in line with those used in the optical engine ignition studies of Herweg and Maly [7]. The RNG k-epsilon model was used for closure of the Reynold's stress and flux terms appearing in the RANS transport equations, while the swirl number was set to 1.5, consistent with previous quasi-dimensional modeling of this engine [1]. Consistent with the magnitudes used in previous simulation work [8], the initial fraction of turbulent kinetic energy to the mean kinetic energy of the flow field, based on the mean piston speed, was set to 0.75 for both SI and SACI simulations.

Figure 4.2 compares the KIVA-CFMZ cylinder pressure predictions to those from the experiment for a speed sweep at WOT operation, while the results of an equivalence ratio sweep at part load with constant spark timing are shown in Figure 4.3. From the figures, it is evident that the model over-estimates peak cylinder pressure and pressure rise rates for some, but not all of the modeled conditions. Additional simulations of a spark timing sweep are shown in Figure 4.4. It is evident from Figure 4.2 through Figure

4.4 that while the model does not make completely quantitative predictions, it does render excellent trend-wise agreement across a broad range of conditions with a constant set of tuning parameters.

4.5 Comparison of Simulated and Experimental SACI Results

With the tuning parameters established from the SI combustion cases, KIVA-CFMZ is applied to SACI combustion cases, with the model input parameters given in Table 4.5, and model constants, α_0, β_0 and C fixed at the values established in the Duratec simulations, while the swirl number was set to 1.0. Chemical kinetic calculations were performed with the 215 species skeletal isooctane mechanism of Tham et al. [9]. Piston, wall and head temperatures were assumed to be in proximity to the jacket water temperature of the engine, which was roughly 390 K.

The reported experimental IMAT is expected to vary from the temperature of the trapped mixture mass at intake valve closing, because of intake manifold heat loss resulting from the elevated IMAT, fuel vaporization and trapped residual fraction from the previous cycle. Due to the absence of experimental fuel and air flow rate data, an alternative approach was required to obtain the IVC temperatures needed for the initialization of the simulation. To find this temperature, a parametric study of IVC temperature was performed with KIVA-CFMZ operating in HCCI mode to determine an offset between the simulation's IVC temperature and the experimental IMAT for HCCI data from Zigler at Φ = 0.45, IMAT = 592 K [2]. Lowering the simulated IVC temperature by 20 - 30 K relative to the experimental IMAT resulted in an ignition timing prediction in line with that observed for the experimental case [2]. The IVC temperature of all subsequent SACI simulations was obtained by reducing the experimental IMAT by approximately 25 K.

Figure 4.5 shows the averaged experimental SACI cylinder pressure traces for spark timings of 70° and 20° BTDC. An additional case without spark timing, representative of misfiring HCCI, is also shown. The KIVA-CFMZ cylinder pressure predictions in Figure 4.5 (right) display trend-wise agreement with those from the experiments. It can be observed that the peak cylinder pressure of the 70° BTDC simulation case is higher than that of the experiment, while the simulated 20° BTDC case displays extremely late combustion relative to the corresponding experimental timing case. The advance of the simulated spark timing by 7° to 27° BTDC provides a more reasonable pressure trace agreement. Consistent with the experimental trends, earlier spark timings advance the combustion phasing, while both no spark cases are shown to misfire.

An IMAT sweep is shown in Figure 4.6 for a simulated spark timing of 27° BTDC and an experimental spark timing of 20° BTDC. The simulation trends are consistent with those of the experiments, where increasing IMAT advances the overall combustion phasing. While the cylinder pressure trends are consistent, a noticeable over-prediction of peak cylinder pressure occurs for the simulation results.

The propagation of a flame surface density iso-volume for the 27° BTDC spark ignition timing case from Figure 4.5 is shown in Figure 4.7. The iso-volume is defined by shading flame surface densities from 1 to 5 cm^{-1} with a constant color scale of dark grey. This range of flame surface density was selected to define regions within the domain where significant flame surface density was present, with maximum values typically ranging from 3 to 6 cm^{-1} for the SACI simulations. The flamelet combustion model, Equations 3.33 and 3.34, is active in regions wherever flame surface density is present, meaning that the iso-volume evolution is representative of a propagating, turbulent reaction front. In these images, the crank angle corresponding to TDC combustion is 720°. Several features are noticeable in the first image from Figure 4.7 at 695° (25° BTDC). The mesh is slanted slightly upwards, with the intake and exhaust

valve faces clearly visible, while the piston crown surface is denoted by the slightly dark shading at the bottom of the image. The initial flame surface density iso-volume is visible in the image as the dark grey hemispherical region in proximity to the ignition cell, approximately centered between the valves. The reaction front is noted to grow almost spherically in time, eventually making contact with the piston crown at 715° (5° BTDC). At 725°, the wall cells at the piston crown are consumed by the reaction front, opening a hole in the flame surface density iso-volume. From the images at 730° and 735° (10° and 15° ATDC), it is apparent that the iso-volume is largely a hollow shell. The thickness of the iso-volume evident at the piston crown surface is dictated in part by the relatively coarse mesh typical of RANS simulations. By 735° and 740° (15° and 20° ATDC), the destruction of the flame surface density due to auto-ignition is evident. This destruction is primarily a result of the sensitivity of the flame surface density destruction term in Equation 3.58 to reaction progress.

The simulated flame surface density iso-volume is overlaid on a semi-transparent *z*-clip plane at 7.7 cm, as shown in Figure 4.8, along with a *y*-clip plane discussed later. These planes are configured to display the temperature of the computational cell. To provide a measure of end-gas ignition, the plane is shaded to display temperatures between 900 and 1100 K, where light grey shading corresponds to temperatures of 900 K and below and black shading corresponds to temperatures of 1100 K and above. These temperatures were selected to show the transition of the end-gas to the beginning of thermal runaway, which begins around 1100 K [10]. The simulated flame surface density iso-volume and clip plane temperature images are then compared to experimental chemiluminescence images in Figure 4.9 and Figure 4.10.

The comparison in Figure 4.9 and Figure 4.10 is performed for the cases with similar cylinder pressure profiles shown in Figure 4.5, where the experimental results are for a spark timing of 20° BTDC and the simulation results are for a spark timing of 27° BTDC. Crank angles were assigned to the experimental images based upon the image

time stamp. Referring the crank angle labels on the RHS of the figures, reaction front propagation is visible in the chemiluminescence and the flame surface density images from 695° to 720° (25° to 0° BTDC). In addition, the simulation's clip plane darkens as the temperature within the end-gas upstream of the front begins to exceed 900 K. This darkening is due primarily to piston compression as the reaction progress defined according to Equation 3.42 remains at near zero levels within the end-gas of the clip plane. By 715°-720° (5° to 0° BTDC), the corresponding experimental luminescence images appear black within the center of the reaction front, most likely due to quenching as the reaction front contacts the optical window of the piston. Similar trends are shown during this timeframe as the flame surface density iso-volume flattens as it contacts the piston crown. By a crank angle of 725° (5° ATDC), a hole is also clearly evident in the iso-volume. The clip plane within this newly opened iso-volume hole is also shaded black, showing that the temperatures are elevated, while reaction progress defined by Equation 3.42 is near unity. The transition to end-gas knock in the optical engine is apparent by 720° (TDC), as thick luminous zones begin to appear upstream of the reaction front. Given that the experimental images are for a single cycle, the later model transition to auto-ignition is not entirely unexpected, due to the thermal sensitivity of HCCI. The simulated cases show signs of end-gas reaction progress due to auto-ignition within the clip plane around 730° (10° ATDC), and are rapidly combusting by 735° (15° ATDC, not shown in figure). It is clear from the images that the transition to chemically dominated combustion corresponds with the rapid pressure increases occurring shortly after TDC.

4.6 Additional Insight into SACI Combustion from KIVA-CFMZ

Figure 4.11 and Figure 4.12 show additional images of the flame surface density iso-volume overlaid on a clip plane through y = 0 mm and the z clip plane used above at

spark timings of 27° and 70° BTDC, respectively. The trends shown in both images are similar to those discussed above. The flame surface density appears shortly after the time of spark, while the initial portion of the combustion process is dominated by reaction front propagation. The compression heating of the end-gas resulting from the heat release and piston motion are noticeable in the figures. The transition to knock upstream of the reaction front is clearly shown in Figure 4.11 at 735° (15° ATDC). It is also apparent that the enflamed volume for the 70° BTDC spark ignition timing case in Figure 4.12 just prior to knock (710°, 10° BTDC) is greater than that of the 27° BTDC ignition timing case, where the enflamed volume at the onset of knock at 735° (15° ATDC) is shown in Figure 4.11.

Figure 4.13 shows the mass fraction burned (MFB) profiles of the ignition timing study discussed in Figure 4.5. For the 70° BTDC spark timing case (Figure 4.13, upper left), nearly all of the initial heat release is due to reaction front propagation (RF). Around 8° BTDC (352° in the figure), the transition to end-gas auto-ignition (AI) occurs, with a significantly faster heat release rate. The flat lining of the RF contribution at the start of end-gas heat release shows an abrupt transition in combustion modes from reaction front propagation to AI type combustion. A nearly 50/50 split is shown in the mass consumed by AI and RF. Retarding the ignition timing to 27° BTDC (Figure 4.13, upper right), the RF heat release drops to approximately 30% of the total, while the rate of AI heat release is noticeably lower due to the competing effects of end-gas compression via the heat release and piston expansion occurring during the late AI combustion phasing. This figure shows concurrent heat release due to the reaction front and auto-ignition between 10 and 15 ° ATDC.

Two limit cases are also presented in Figure 4.13. These cases include one with a spark timing of 20° BTDC (lower left) and one with no spark case (lower right). The 20° BTDC case is dominated by RF heat release, and while some AI heat release is noted to begin around TDC, this heat release ceases around 10° ATDC, while the cumulative

MFB for this partially burning case approaches 75% by exhaust valve opening. For the case with no spark, there is no AI heat release apparent within the figure. This case is representative of a total misfire and with the 70° and 27° BTDC spark timing cases discussed above, is a clear demonstration of the ability of SACI to influence the phasing of LTC combustion.

The mass averaged end-gas temperature profiles corresponding to the mass fraction burned plots of the 70° and 27° BTDC cases in Figure 4.13 are shown in Figure 4.14. Figure 4.14 overlays the end-gas temperature profiles with the overall and AI mass fraction burns. The average end-gas temperatures corresponding to 1% of the relative end-gas energy release are 1045 K for the 70° BTDC case (left) and 960 K for the 27° BTDC case (right). For the 70° BTDC case, the end-gas temperature increase is driven by the global pressure rise induced by heat release from the reaction front and piston compression, inducing auto-ignition before TDC. For the 27° BTDC case, the reaction front slightly increases and sustains the end-gas temperature at 960 K, even though expansion is occurring around this end-gas temperature. The end-gas temperature is essentially maintained by the heat release from the front until the onset of auto-ignition. From the end-gas temperatures shown in Figure 4.15 (left) and their close ups in Figure 4.15 (right), it is clear that the mass average end-gas temperature of the 20° BTDC case never exceeds 940 K, while the end-gas temperature of the no spark case never exceeds 936 K. This is in contrast to the 27° BTDC case that is compression heated to 960 K, almost isothermally for a span of 5° shortly after TDC, before clearly transitioning to thermal runaway.

Figure 4.16 shows the mass averaged flame surface density (left) and the total flame surface area calculated from the flame surface density (right). For the average flame surface density, the transition to the turbulent flame model for the 70° BTDC and 27° BTDC cases is apparent at 295° and 337° within the slight flame surface density jumps shown in the figures. The average flame surface density is shown to increase

rapidly in time, most likely through the continued stretching of the reaction front by the turbulent flow field, modeled with the flame stretch source term of the ITNFS model of Meneveau and Poinsot [11]. The positive growth rate of the flame surface density and the total flame surface area begins to decrease slightly around the time that the flame surface contacts the piston crown, around 340° and 355° for the 70° BTDC and 27° BTDC ignition timing cases. Significant reductions in the flame surface area and the flame surface density are noted around the onset of end-gas knock, beginning at 352° and 370° for the 70° BTDC and 27° BTDC ignition timing cases, respectively.

Assuming that the ITNFS flame stretch model and flame property correlations are valid under SACI conditions, the fact that significant levels of flame surface density are present during the front propagation portion of the simulations suggests the presence of turbulent deflagrations under SACI conditions. Therefore, although the mixture is ultra-dilute, the reaction front remains thin and within the flamelet regime under the high pre-heat temperature and pressure conditions of SACI combustion, consistent with the laminar flame thicknesses shown in Figure 2.15. If the flamelet concept were not valid under SACI conditions, then the flame surface area and density would have been destroyed by the flame stretch model, replicating the negative flame stretch imposed on the flame surface through eddy strain during bulk quenching.

The peak flame surface densities for the simulated 27° BTDC spark timing case were slightly greater than 5 cm^{-1}. This value is similar to the peak flame surface densities observed in previous computational engine studies, where maximum flame surface densities ranged from approximately 2.5 to 4.0 cm^{-1} with Φ ranging from 0.7 to 0.9 at an engine speed of 1200 RPM with a turbulent intensity around 2.4 m/s at a spark timing of 25° BTDC [5]. Additional LIF images of SI combustion in an optical engine at engine speeds between 600 and 1200 RPM showed peak flame surface densities ranging from 3.4 to 3.8 cm^{-1} [12].

The laminar flame speed calculated for the average end-gas conditions is shown in Figure 4.17. The increase in the flame speed throughout the cycle results from the increase in end-gas temperature, which is slightly offset by the accompanying increase in cylinder pressure throughout the compression event. The significant jump at 375° in the 27° BTDC timing case corresponds to the rapid end-gas temperature increase associated with the onset of rapid end-gas combustion through knock.

The approximate reaction front radius is shown as a function of crank angle for the 70° BTDC and 27° BTDC ignition timing cases in Figure 4.18 (left). This radius was calculated by tracking the line of sight radial growth of the leading edge of the flame surface density iso-volume in the nine o'clock direction in the *z* plane of Figure 4.7. The interval between points (every 10°) was selected so that the growth of the front radius was approximately three times the computational cell thickness. Expansion speed calculations made at half of the above crank angle interval did not show significant changes with the shorter front distances traveled. The front radius results are trend-wise similar with those shown in Beretta et al. [13]. Additional measures could be used to improve the accuracy of these measurements, including the measurement of the projected front area, or through the use of edge finding algorithms [14].

Finally, the apparent propagation speed of the flame surface density iso-volume shown in Figure 4.18 (right) is determined from the growth rate of the reaction front radius in Figure 4.18 (left). The speeds in the figure are shown to range from near zero values early in the front propagation process to up to 4 m/s towards the process's end. These propagation speed increases are observed to occur in conjunction with the increases in average flame surface density, Figure 4.16 (left) and laminar flame speed, Figure 4.17. The mean propagation speeds determined from the slope of the linear portion of the flame radius (the final four crank angles in the 70° BTDC case and all of the data in the 27° BTDC case) provide mean expansion speeds of 289 and 209 cm/s for the 70° BTDC and 27° BTDC cases, respectively.

4.7 Conclusions

The KIVA-CFMZ model was compared to experimental data sets originating from SI and SACI combustion experiments. The model was capable of providing trend-wise agreement to SI combustion data when using flame model constants with magnitudes similar to those reported in previous engine studies. With the flame model constants established in the SI engine study, optical SACI experiments were simulated to gauge the performance of the laminar reaction front simulation correlations described in Chapter 2 and the sub-grid combustion model formulation detailed in Chapter 3. While not quantitative, the trend-wise cylinder pressure agreement between the model and experiments was acceptable and clearly demonstrated the ability of reaction front propagation to influence the phasing of auto-ignition during SACI combustion. In addition, the reaction front propagation observed in the experimental chemiluminescence images was replicated by the flame surface density propagation occurring in the KIVA-CFMZ simulations. The diameter of the reaction front and the flame surface density iso-volume are shown to be of similar magnitudes at similar times during the front propagation portion of SACI combustion. The presence of the flame surface density also suggests that the reaction front remains thin and is not quenched by eddies within the surrounding flow field. The mechanism for transitioning from the reaction front propagation mode of SACI combustion to end-gas auto-ignition was found to be similar to end-gas knock in conventional spark-ignited engines, occurring when the end-gas compression heating due to piston motion and reaction front heat release combined to drive the end-gas to its ignition temperature.

Table 4.1: Duratec engine geometry and specifications

Compression Ratio	9.7:1
Bore (mm)	82.4
Stroke (mm)	79.5
Intake Valve Closing (ABDC)	50°
Exhaust Valve Opening (BBDC)	43°
Fuel	93 Octane Gasoline

Table 4.2: Optical engine geometry and specifications

Engine Speed (RPM)	700
Compression Ratio	10.0:1
Bore (mm)	71.9
Stroke (mm)	76.5
Intake Valve Closing (ABDC)	42°
Exhaust Valve Opening (BBDC)	34°
Crown Window Diameter (mm)	48.5
Fuel	Indolene

Table 4.3: Simulated Duratec cases

Case	1	2	3	4	5	6	7	8	9	10
Speed (RPM)	1500	2000	2000	2000	2000	2000	2000	2000	2000	2000
BMEP (bar)	9.04	9.55	3.32	3.35	3.34	3.31	3.36	3.35	3.33	3.30
Spark (°BTDC)	6	9	26	26	26	26	50	30	10	0
Φ	1.00	1.00	0.77	0.83	0.91	1.00	1.00	1.00	1.00	1.00

Table 4.4: CFMZ simulation details for the Duratec cases

α	1.9
β	1.0
$T_{cylinder}$ (K)	410
T_{head} (K)	454
T_{piston} (K)	500
Fuel	Iso-octane

Table 4.5: CFMZ simulation details for the optical engine cases

α_0	1.9
β_0	1.0
$T_{cylinder}$,T_{head},T_{piston} (K)	390.0
Fuel	Iso-octane

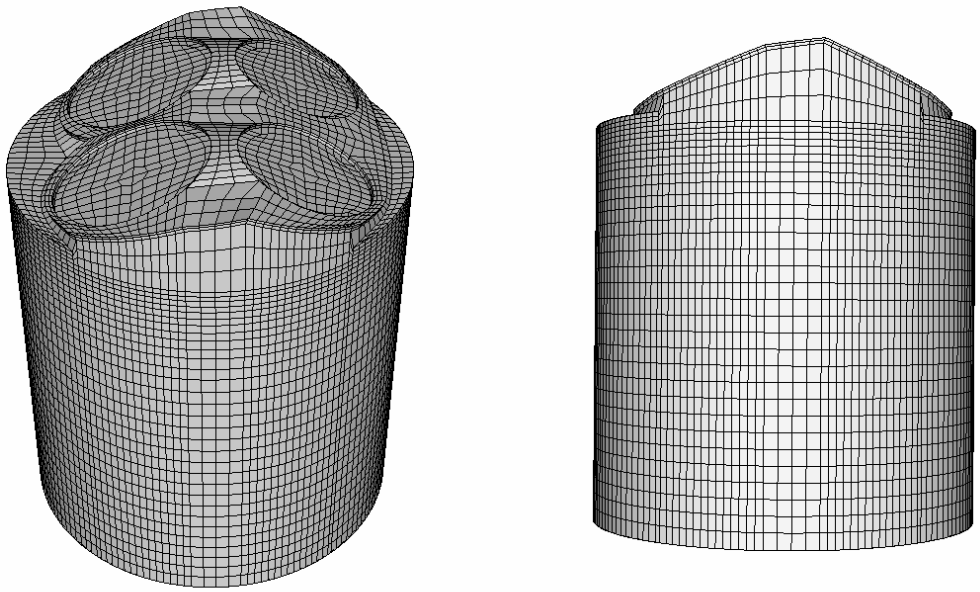

Figure 4.1: The computational mesh used for the optical SACI engine study.

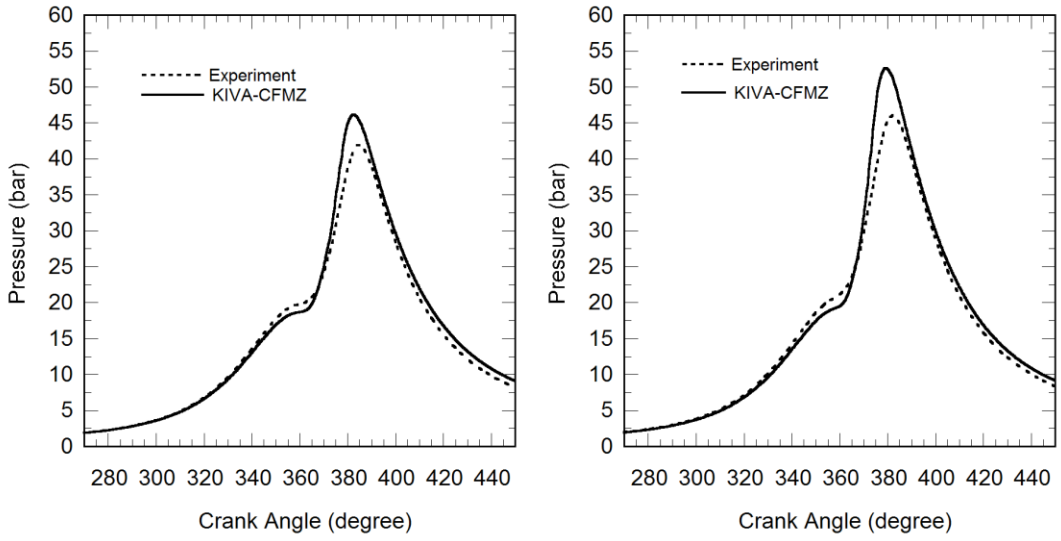

Figure 4.2: Cylinder pressure vs. crank angle for SI Case 1 (left) and Case 2 (right).

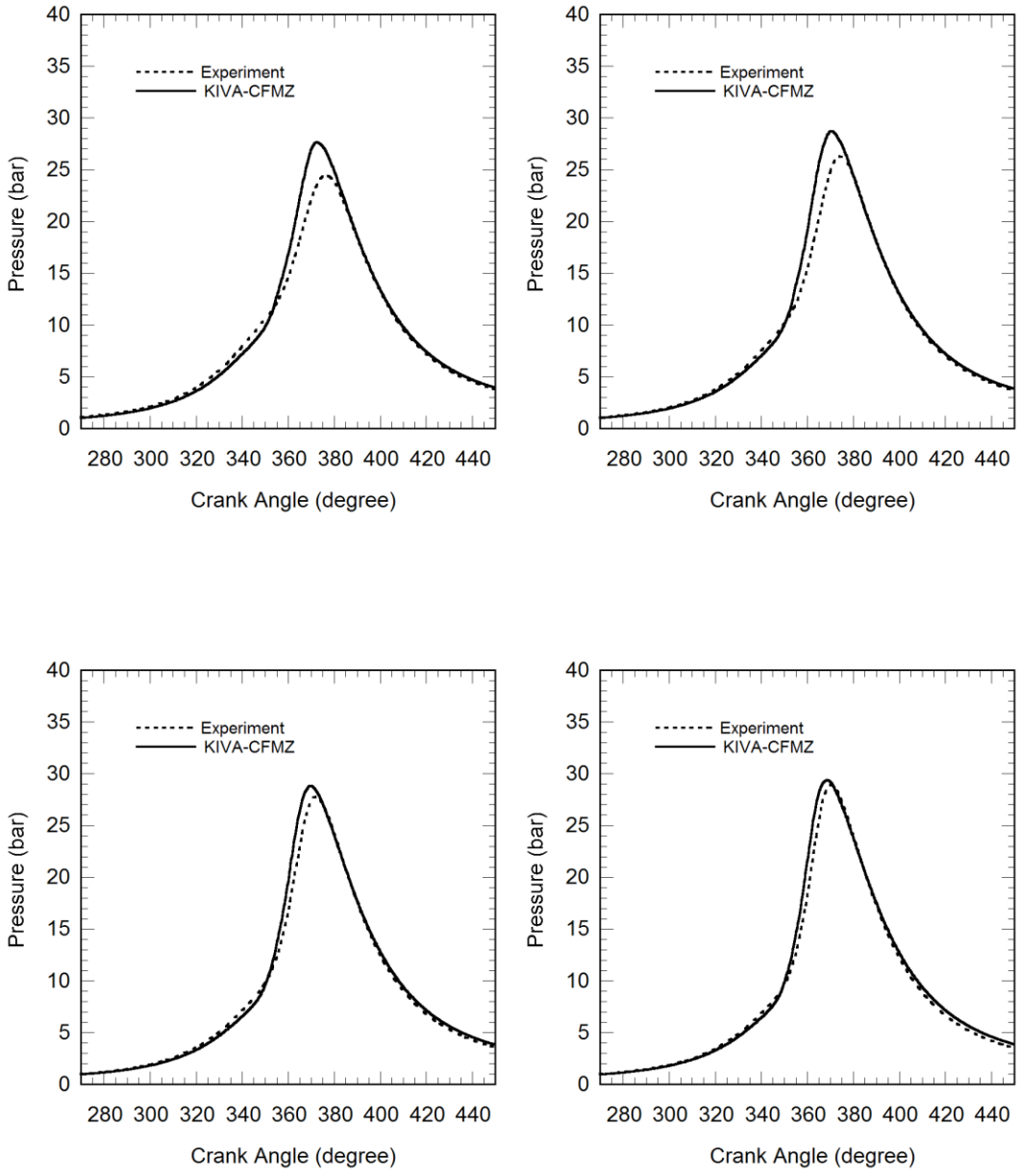

Figure 4.3: Cylinder pressure vs. crank angle for SI Case 3 (upper left), Case 4 (upper right), Case 5 (lower left) and Case 6 (lower right).

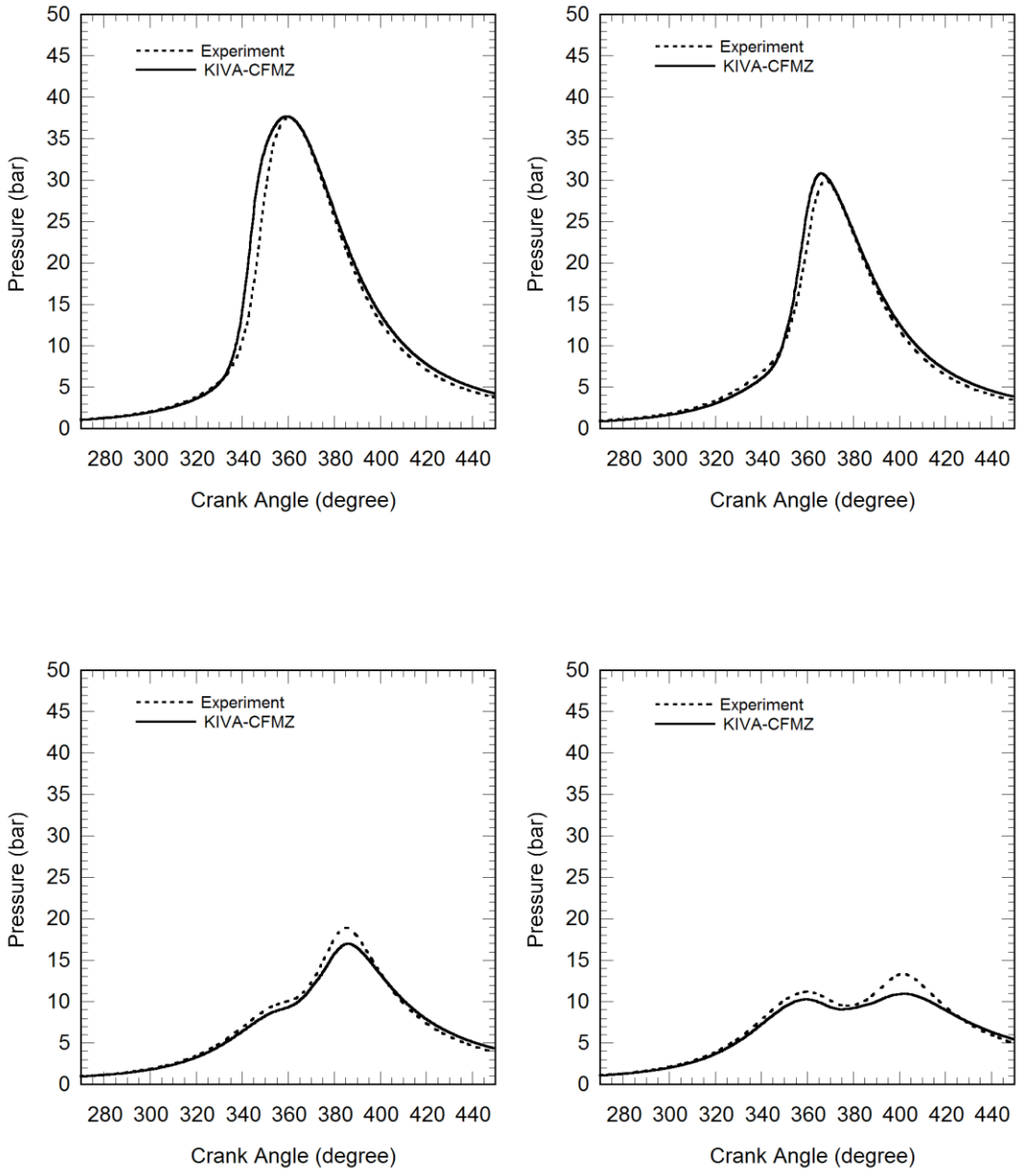

Figure 4.4: Cylinder pressure vs. crank angle for SI Case 7 (upper left), Case 8 (upper right), Case 9 (lower left) and Case 10 (lower left).

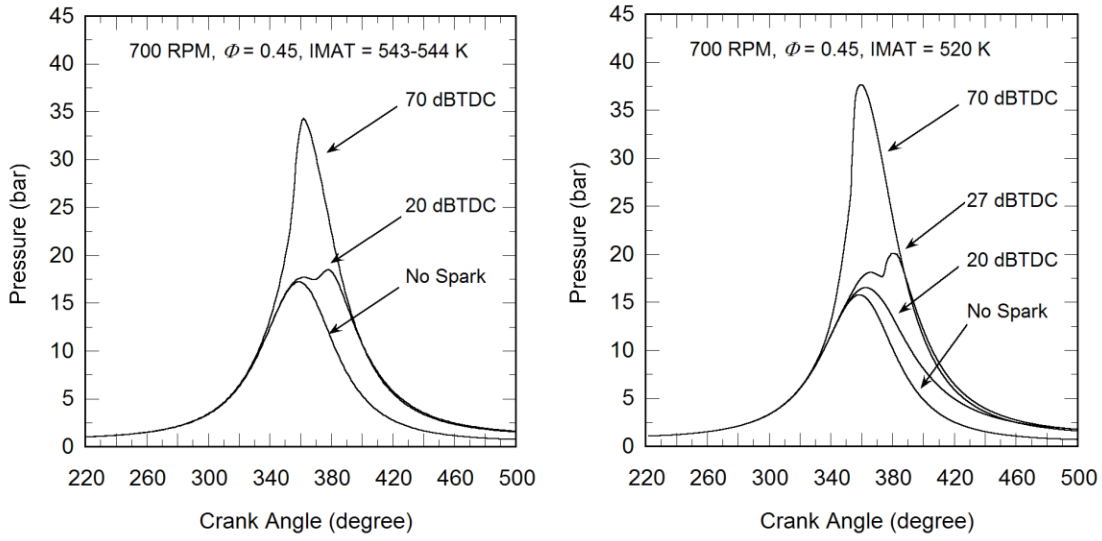

Figure 4.5: Cylinder pressure vs. crank angle at 700 RPM, Φ = 0.45. Averaged SACI experimental cylinder pressure data for three timings (left) vs. a simulation timing sweep (right).

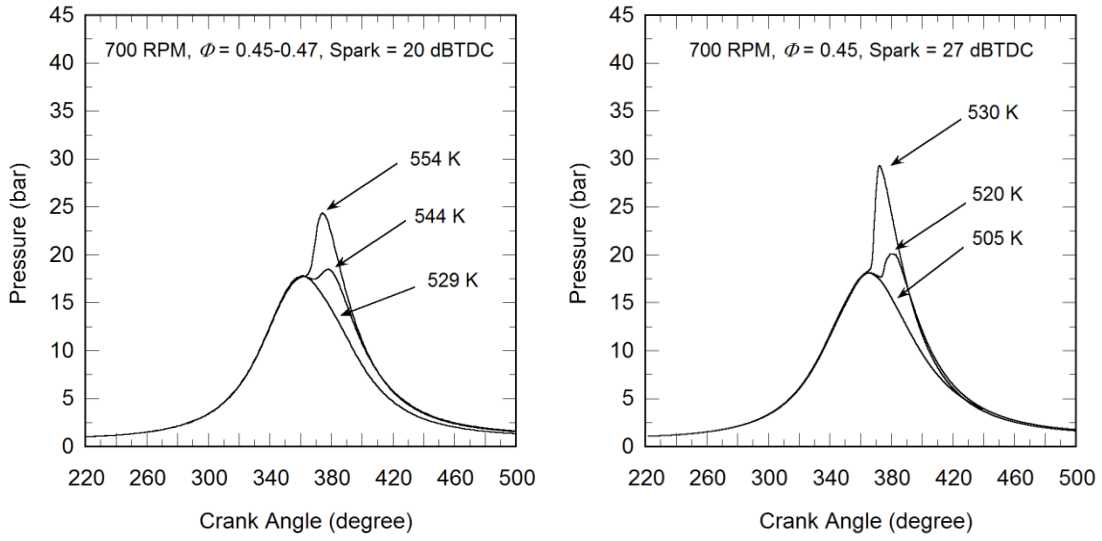

Figure 4.6: Cylinder pressure vs. crank angle at 700 RPM, Φ = 0.45. Averaged SACI experimental cylinder pressure data for three IMATs at 20° BTDC spark (left) vs. a simulation IMAT sweep at 27° BTDC spark (right).

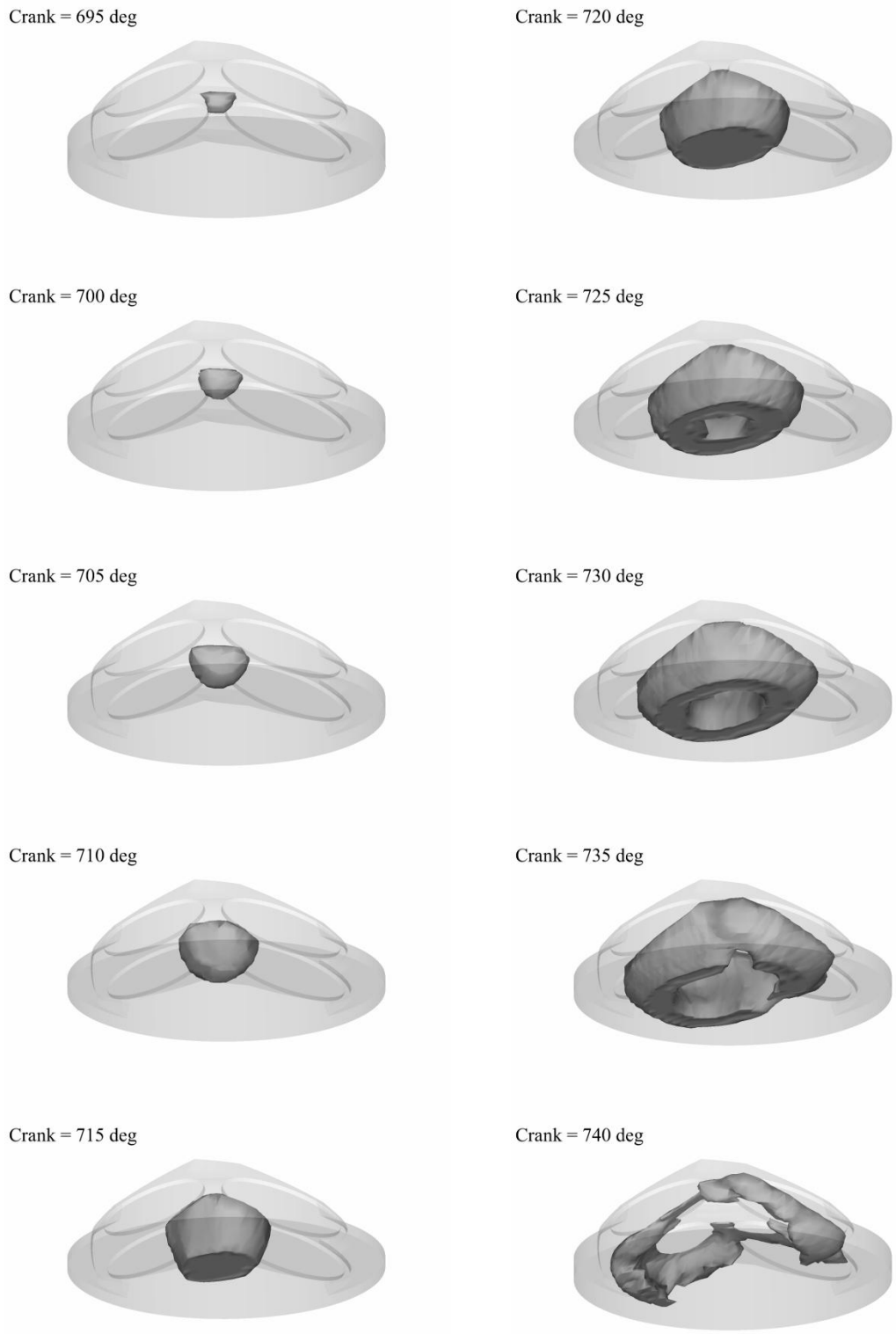

Figure 4.7: View of simulated flame surface density propagation at various crank angles for 700 RPM, Φ = 0.45, 27° BTDC spark timing.

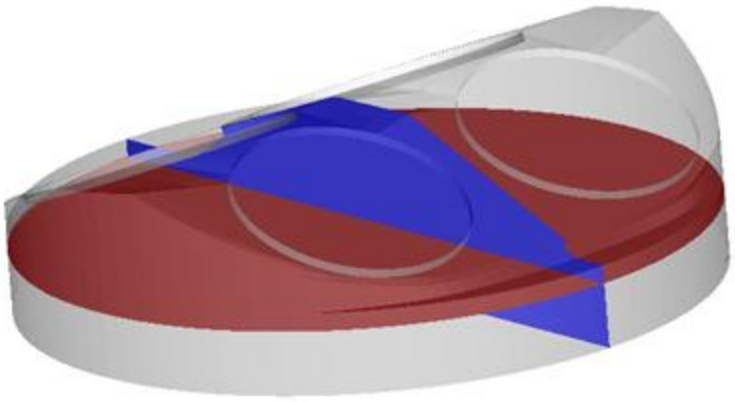

Figure 4.8: The Y and Z clip planes used for imaging the computational cell temperatures.

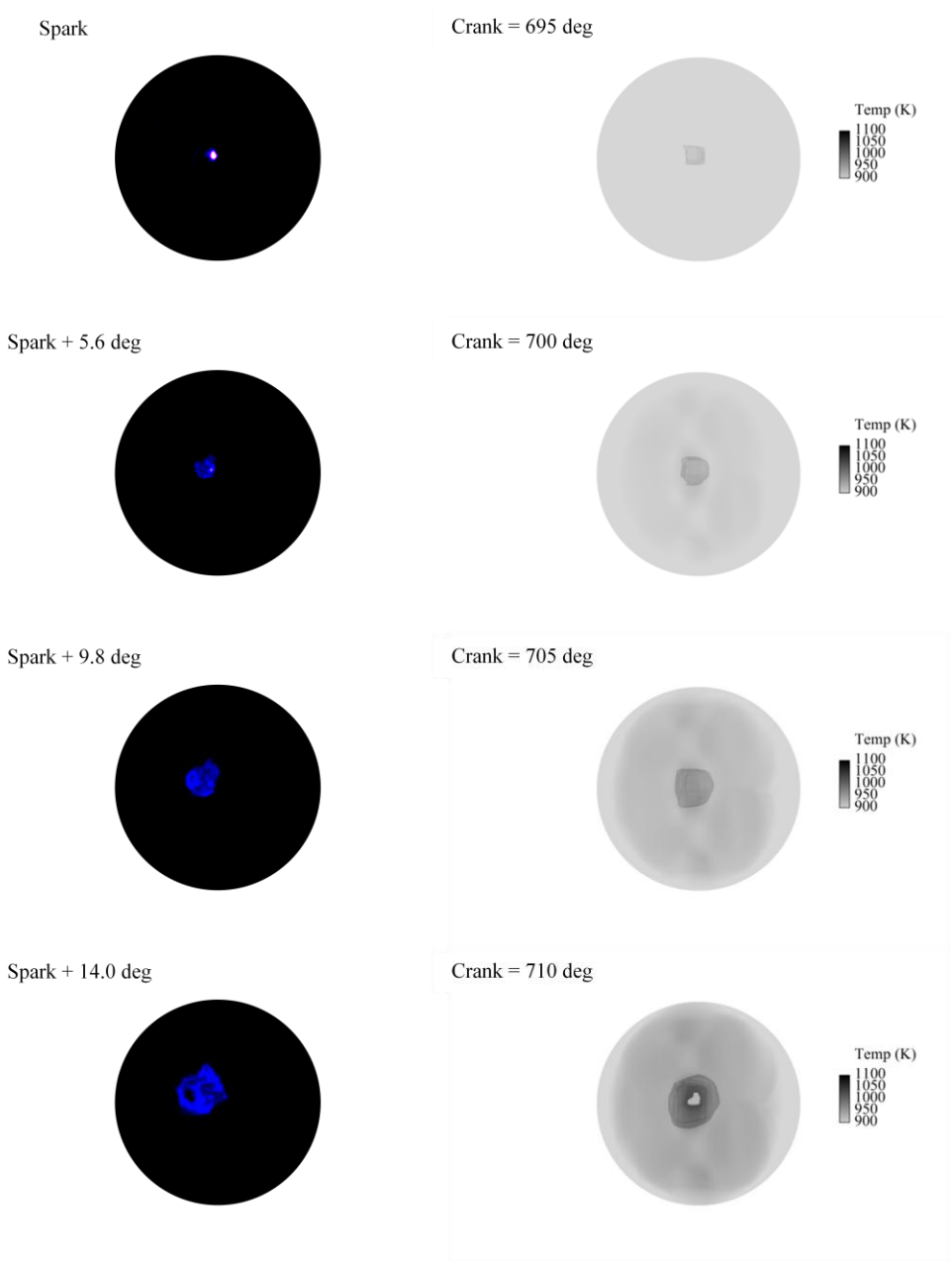

Figure 4.9: Early Z clip plane views of experimental chemiluminescence (left) at 20° BTDC spark timing and simulated flame surface density propagating into the end-gas temperature field at various crank angles for 700 RPM, $\Phi = 0.45$, 27° BTDC spark timing.

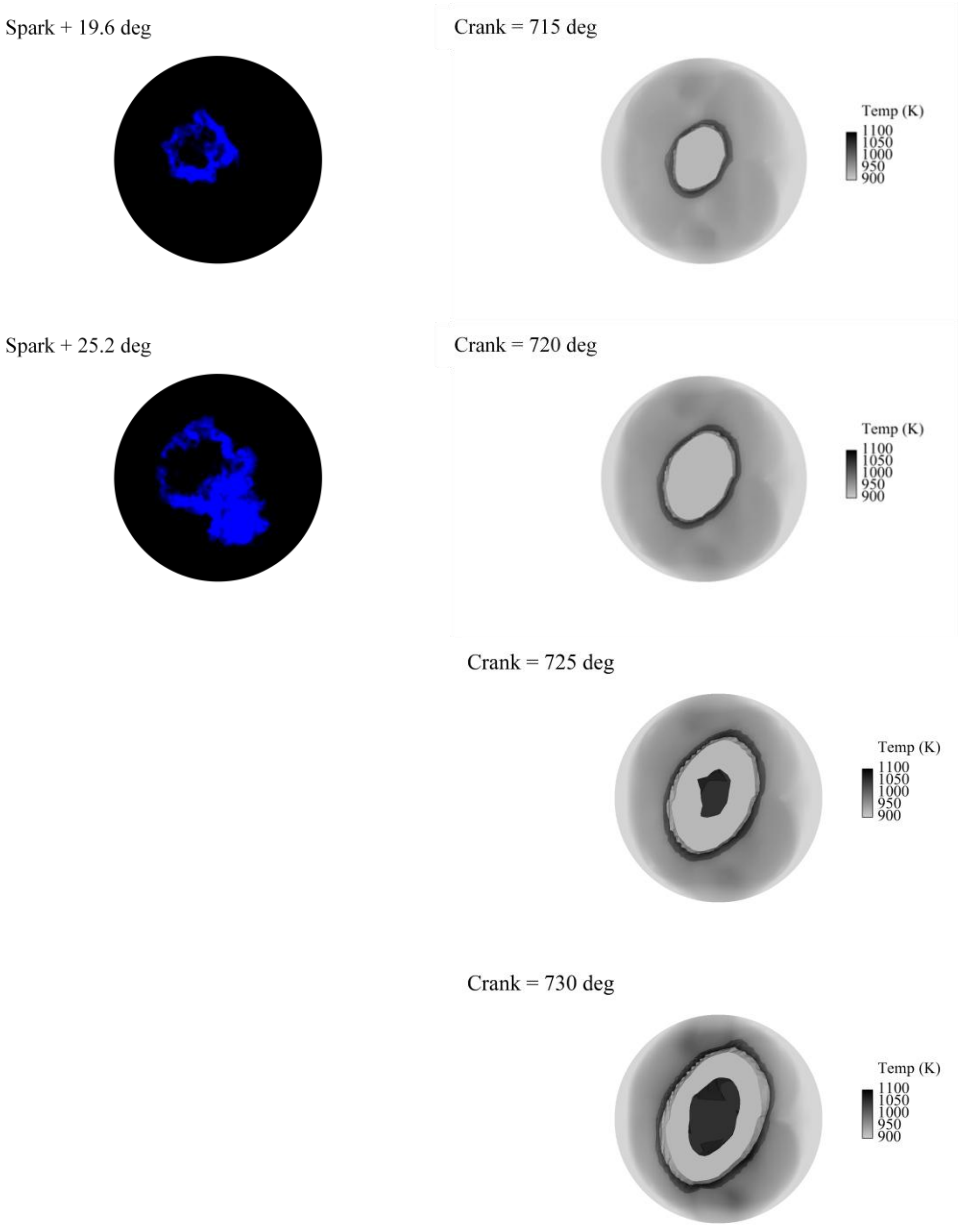

Figure 4.10: Later Z clip plane views of experimental chemiluminescence (left) at 20° BTDC spark timing and simulated flame surface density propagating into the end-gas temperature field at various crank angles for 700 RPM, $\Phi = 0.45$, 27° BTDC spark timing.

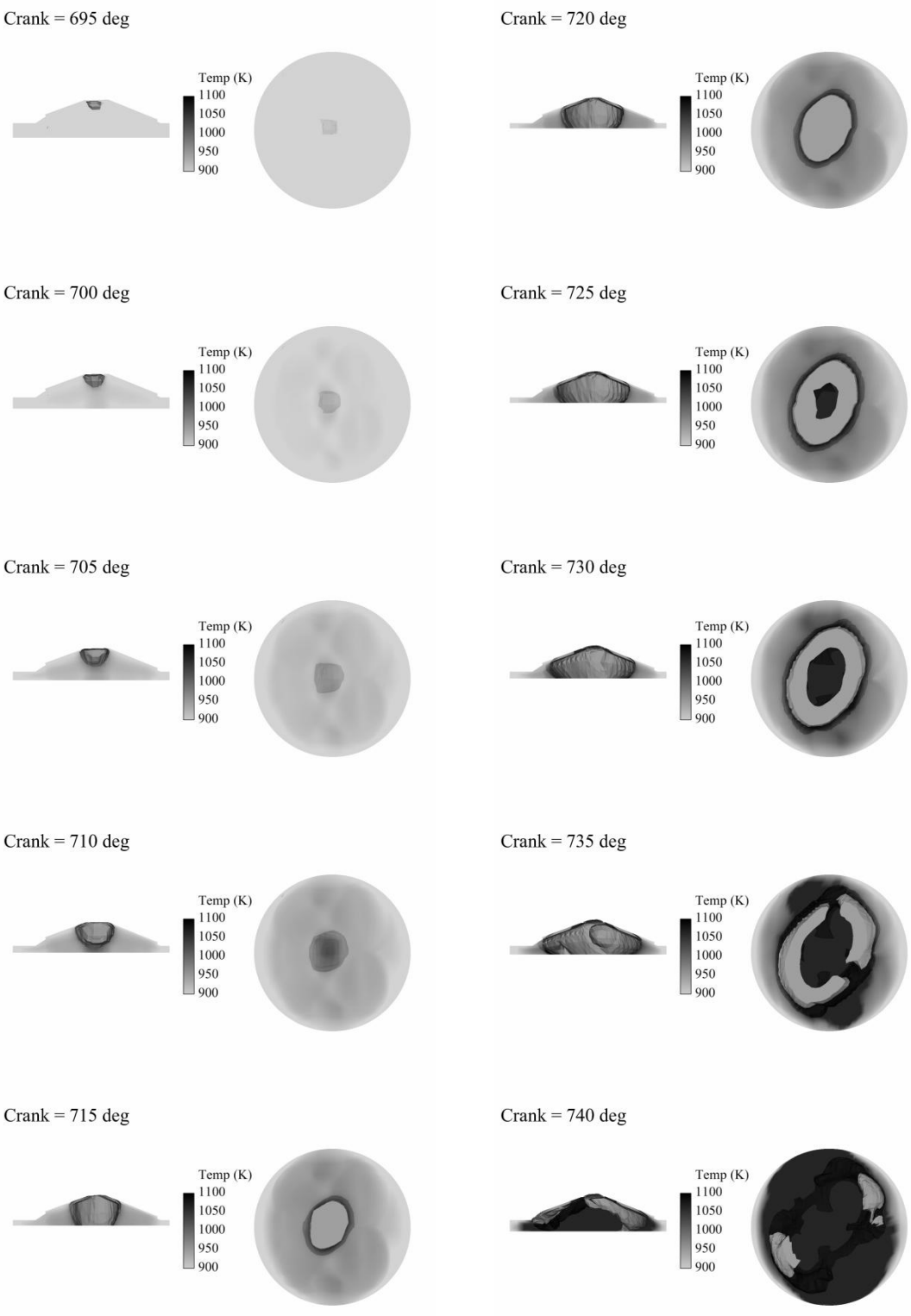

Figure 4.11: Y and Z clip plane views of simulated flame surface density propagation into the end-gas temperature field at various crank angles for 700 RPM, $\Phi = 0.45$, 27° BTDC spark timing.

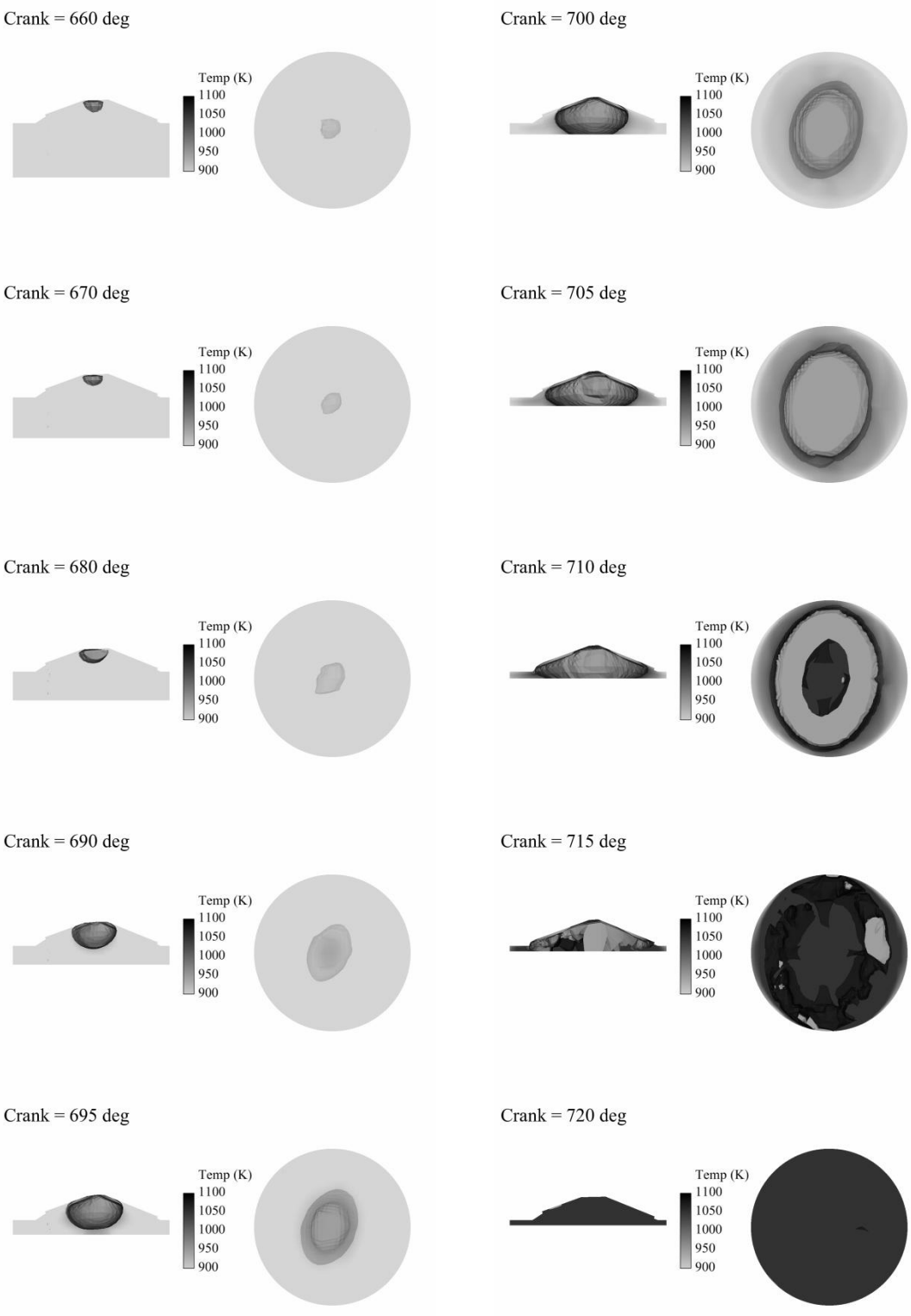

Figure 4.12: Y and Z clip plane views of simulated flame surface density propagation into the end-gas temperature field at various crank angles for 700 RPM, $\Phi = 0.45$, 70° BTDC spark timing.

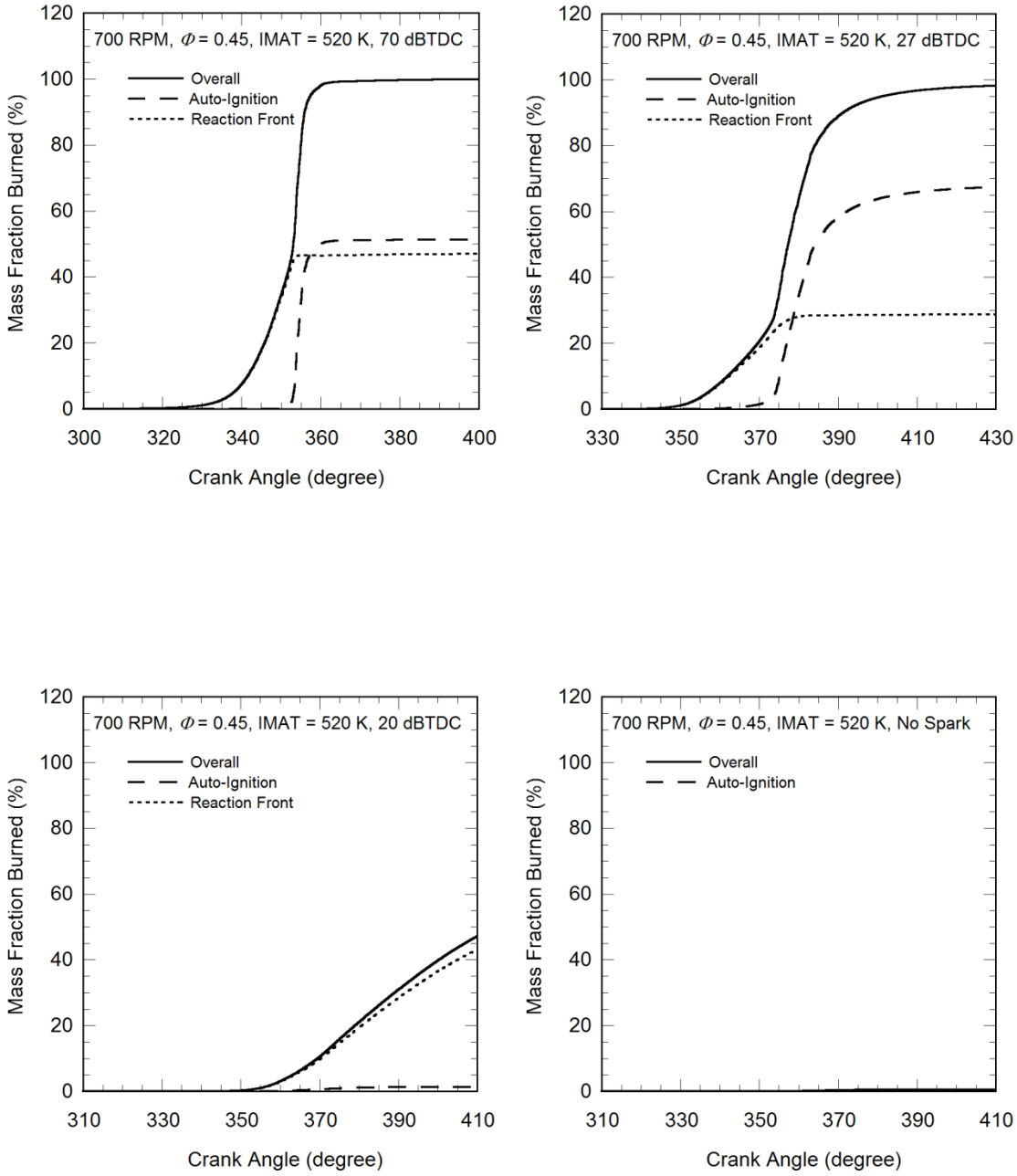

Figure 4.13: Simulated mass fraction burned vs. crank angle at 700 RPM, Φ = 0.45 at spark timings of 70° BTDC (upper left), 27° BTDC (upper right), 20° BTDC (lower left), and for no spark (lower right).

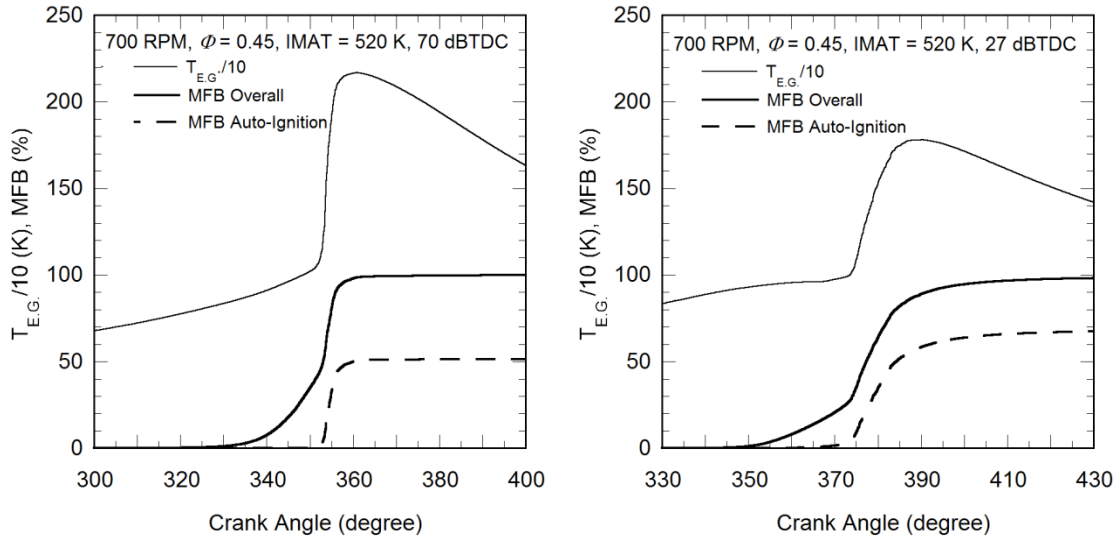

Figure 4.14: Simulated mass fraction burned and mass average end-gas temperature vs. crank angle at 700 RPM, Φ = 0.45 at spark timings of 70° BTDC (left), 27° BTDC (right).

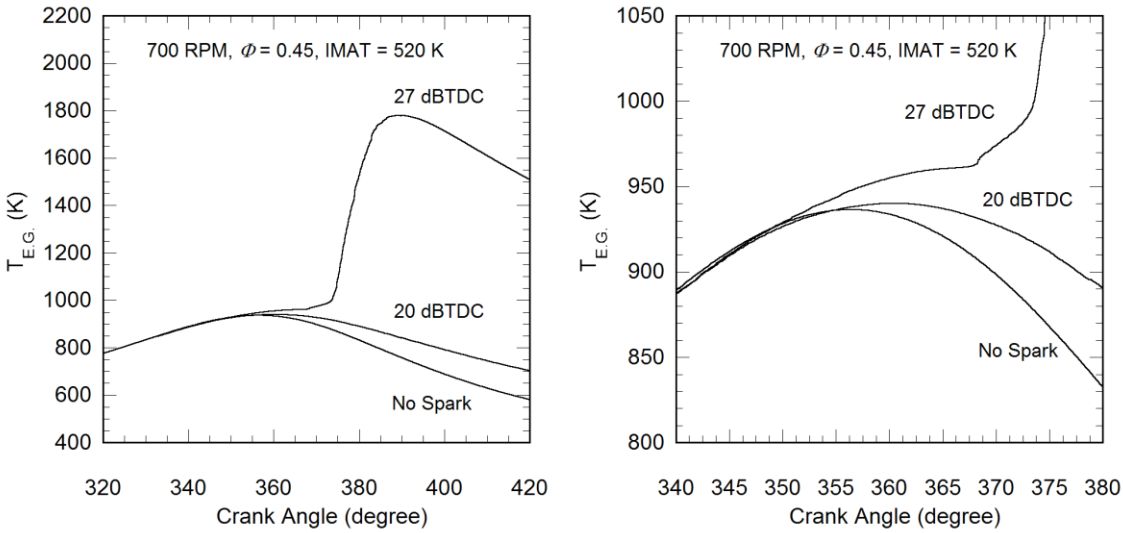

Figure 4.15: Simulated, mass average end-gas temperature vs. crank angle at 700 RPM, Φ = 0.45 at spark timings of 27° and 20° BTDC and with no spark (left). Closeup of the end-gas temperature profiles (right).

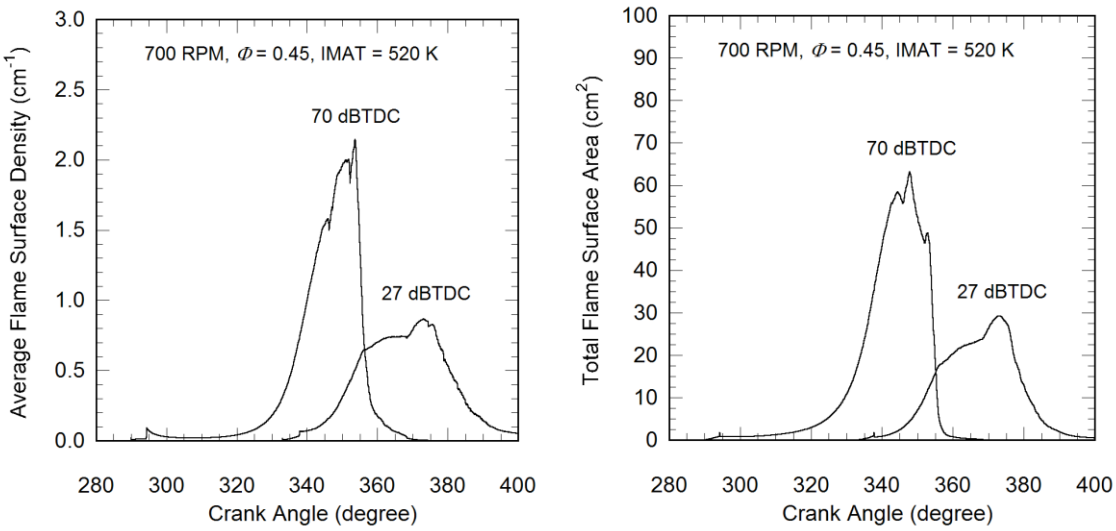

Figure 4.16: Average flame surface density (left) and the total flame surface area (right) vs. crank angle at 700 RPM, Φ = 0.45 for spark timings of 27° and 20° BTDC.

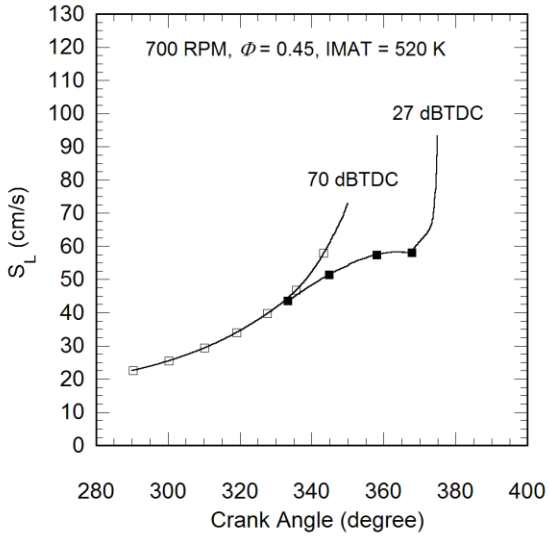

Figure 4.17: Laminar flame speed from the ignition timing up to the last times shown in Figure 4.18, calculated with the average properties from the reactant zone, with markers shown at every 1% of the data.

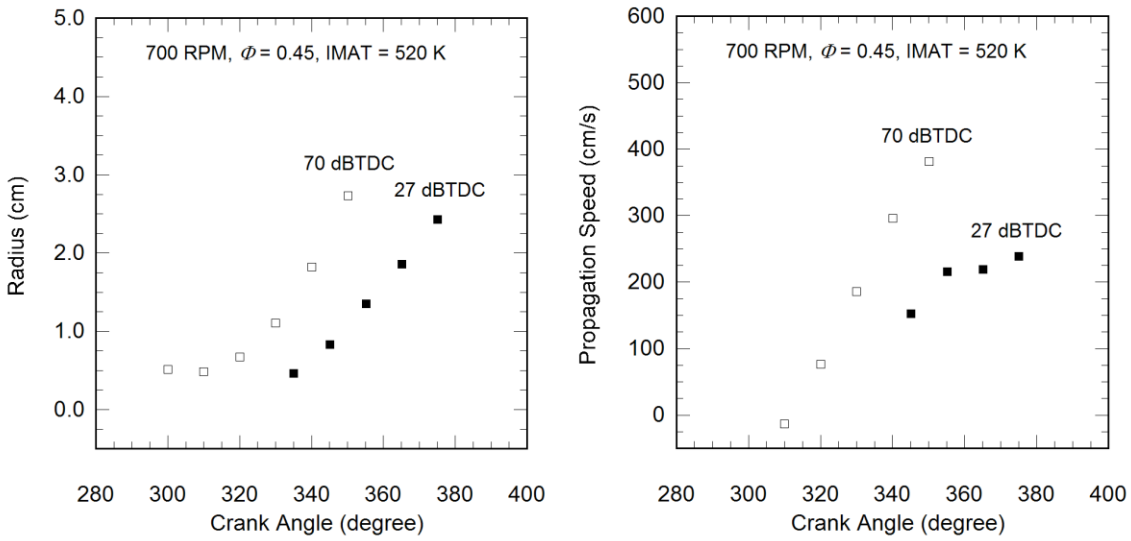

Figure 4.18: Simulated radius of the leading edge of the flame surface density iso-volume between 1 and 5 (cm^{-1}) vs. crank angle at 700 RPM, Φ = 0.45 at spark timings of 70° and 27° BTDC (left). Flame surface density propagation speed vs. crank angle at 700 RPM, Φ = 0.45 for spark timings of 27° and 20° BTDC (right).

4.8 References

1. Bohac, S.V., *Reduction of Spark-Ignition Engine Hydrocarbon Emissions and the Associated Local Ozone Production Through Variable Exhaust Valve Timing*, Ph.D. Thesis University of Michigan, Ann Arbor (2003)

2. Zigler, B., *An Experimental Investigation of the Properties of Low Temperature Combustion in an Optical Engine*, Ph.D. Thesis University of Michigan, Ann Arbor (2008).

3. Angelberger, C., "3D Modeling of Mixing, Ignition and Combustion Phenomena in Highly Stratified Gasoline Engines," *Oil and Gas Science and Technology-Rev. IFP*, Vol. 58 (1): 47-62, 2003.

4. Duclos, J.M., Bruneaux, G., and Baritaud, T.A., "3D Modeling of Combustion and Pollutants in a 4-Valve SI Engine; Effect of Fuel and Residuals Distribution and Spark Location," SAE Paper 961964, 1996.

5. Boudier, P., Henriot, S., Poinsot, T., and Baritaud, T., "A Model for Turbulent Flame Ignition and Propagation in Spark Ignition Engines," *Proceedings of the Twenty-Fourth International Symposium on Combustion:* 503-510, 1992.

6. Teraji, A., Tsuda, T., Noda, T., Kubo, M., and Itoh, T., "Development of a Three-Dimensional Knock Simulation Method Incorporating a High-Accuracy Flame Propagation Model," *International Journal of Engine Research* Vol. 6 (1): 73-83, 2005.

7. Herweg, R., and Maly, R.R., "A Fundamental Model for Flame Kernel Formation in S.I. Engines," SAE Paper 922243, 1992.

8. Sjöberg, M., Dec, J.E., Babajimopoulos, A., and Assanis, D., "Comparing Enhanced Natural Thermal Stratification Against Retarding Combustion Phasing for Smoothing of HCCI Heat-Release Rates," SAE Paper 2004-01-2994, 2004.

9. Tham, Y., Bisetti, F., and Chen, J.Y., "Development of a Highly Reduced Mechanism for Iso-Octane HCCI Combustion with Targeted Search Algorithm," *ASME Journal of Engineering for Gas Turbines and Power*, Vol. 130, 2008.

10. Kelly-Zion, P.L. and Dec, J.E., "A Computational Study of the Effect of Fuel Type on Ignition Time in HCCI Engines," *Proceedings of the Combustion Institute* 28: 1187-1194, 2000.

11. Meneveau, C. and Poinsot, T., "Stretching and Quenching of Flamelets in Premixed Turbulent Combustion," *Combustion and Flame*, Vol. 86: 311-332, 1991.

12. Deschamps, B.M., Smallwood, G.J., Prieur, J., Snelling, D.R., and Gülder, O.L., "Surface Density Measurements of Turbulent Premixed Flames in a Spark-Ignition Engine and a Bunsen-Type Burner Using Planar Laser-Induced Fluorescence," *Proceedings of the Twenty-Sixth International Symposium on Combustion*: 427-435, 1996.

13. Beretta, G.P., Rashidi, M., and Keck, J.C., "Turbulent Flame Propagation and Combustion in Spark Ignition Engines," *Combustion and Flame*, Vol. 52: 217-245, 1983.

14. Keros, P.E., Assanis, D., Schlectweg, J., and Wooldridge, M.S., "Fast Methods to Analyze High-Speed Images of HCCI and Spark-Assisted HCCI Ignition Events," *ASME Internal Combustion Engine Division 2010 Fall Technical Conference*, San Antonio, Texas, September 12-15, 2010.

CHAPTER 5

APPLICATION OF THE KIVA-CFMZ MODEL

From previous studies [1, 2], it has been shown that HCCI is plagued by combustion phasing and rate control issues and inherently low power densities. Recently SACI combustion studies have demonstrated the potential to rectify these issues [3].

Given that elevated compression ratios and their associated mechanical loadings are not a desirable feature for automotive engine applications, moderate compression ratios are employed in conjunction with elevated initial charge temperatures for the control of HCCI combustion phasing. Unfortunately, these elevated charge temperatures negatively affect the density and the resulting mass of air trapped at intake valve closing. The resulting limited chemical energy release constrains naturally aspirated HCCI engine loads to marginal values. While it is well known that the gross indicated efficiencies of HCCI are high, these efficiency gains are often offset by the low mechanical efficiency associated with the anemic IMEP of naturally aspirated HCCI operation [2].

To explore if SACI can be used in conjunction with lowered intake manifold temperature as a means for increasing engine load while maintaining acceptable engine performance and constraint compliance, a parametric study of intake manifold temperature (IMAT) is performed over a wide range of spark timings. To simplify the study, air-dilute mixtures are used with a fixed $\Phi = 0.45$. This Φ is roughly in line with the Φ's observed at the upper limit of air-dilute HCCI combustion, where ignition timings must be retarded close to the point of misfire in order to comply with peak

cylinder pressure, pressure rise rate and NO_x limitations [4]. By fixing Φ, fueling and load are allowed to vary with both IMAT and spark timing.

5.1 IMAT and Spark Timing Parametric Study

The engine modeled in the current chapter was configured with the geometry and conditions shown in Table 5.1. The engine geometry was selected to replicate the main features of the single-cylinder, Fully Flexible Variable Valve actuation (FFVA) engine currently used for the experimental investigation of HCCI and SACI combustion at the University of Michigan. To simplify the analysis of the model results, valve events were maintained at values typical of a conventional SI engine, while air dilution was used in place of the internal and external EGR typically used as diluents in this engine. The procedure adopted for the scaling of the computational mesh and the settings of the ignition system were maintained from those detailed in Chapter 4.

To establish the upper end of the IMAT range used in the spark ignited studies, HCCI simulations were run where ignition timing was controlled through IMAT, as shown in Figure 5.1 (left). The location of CA50 could be changed from 351 to 373º with IMAT ranging from 550 to 490 K. For IMAT below 490 K, the HCCI engine misfired. The range of spark-ignited IMAT's examined was subsequently varied from 490 to 350 K in increments of 20 K, while spark was varied from 80° to 0° BTDC, as shown in Table 5.2.

From Figure 5.1 (right), it is apparent that significant gains in fueling, from 12.9 to 18.1 mg/cycle, can be made as IMAT is lowered from 490 to 350 K. The range of spark timings examined for a given IMAT/fueling are also shown in the figure, where it is clear that the fueling is only a function IMAT, given that Φ is fixed and that trapped residual fraction was not used in this study.

The mean effective pressure for the closed portion of the cycle, $IMEP_{cc}$, is calculated with the indicated work from intake valve closing (IVC) to exhaust valve opening (EVO) timing, which are fixed during this study. The resulting indicated work of the closed cycle is divided by the difference between the maximum volume of the closed portion of the cycle, in this case the volume at IVC, and the minimum volume of the cycle, which occurs at TDC. While $IMEP_{cc}$ is not equivalent to the $IMEP_g$, which is calculated for the compression and expansion events over 360°, $IMEP_{cc}$ and $IMEP_g$ are anticipated to be comparable.

$IMEP_{cc}$ is shown as a function of the fuel delivery in Figure 5.2 (left), where it is clear that the peak $IMEP_{cc}$ increases with fuel delivery. A range of $IMEP_{cc}$ is shown to exist for a given fueling in Figure 5.2 (left), where the departure in $IMEP_{cc}$ from the maximum observed value results from overly advanced or late combustion. From Figure 5.2 (right), it is apparent that an elevated range of closed cycle efficiencies can be obtained at or slightly after a CA50 near TDC, falling within a window of roughly 15º in CA50 (between 355° and 370°). The observed CA50's for optimal closed cycle efficiency are similar to the approximate CA50 required for maximum brake torque (CA50 = 10º ATDC) operation in conventional SI engines [5]. The closed cycle efficiency is noted to drop as CA50 is either advanced or retarded away from the high efficiency region. In general, this efficiency decrease with the advance or retardation of the spark timings results from the increase in compression work and heat losses that occurs when combustion is phased too early, and the lower expansion pressures and work transfers that result when combustion is phased too late [5]. Combustion efficiency is also shown to have a slight effect on the closed cycle efficiency when CA50 is phased near TDC. For example, Figure 5.3 (left) shows that at a given CA50 near TDC, that a nearly 1 point reduction in combustion efficiency occurs when transitioning from an IMAT of 470 K to an IMAT of 350 K. This one point penalty may account for up to a 2.5% reduction in efficiency when closed cycle efficiencies are near 40%.

In general, CA50's corresponding to elevated closed cycle efficiencies could be found for the range of IMAT's examined in this study through variation of the spark timing, as shown in Figure 5.3 (right). It proved necessary to advance spark timing to 60º BTDC for the IMAT = 350 K case (the shaded triangles) in order to phase CA50 near TDC. To obtain similar CA50's for the IMAT = 470 K case (shaded squares), spark timing could be phased later, at 40º BTDC. For the IMAT = 490 K case, the retardation of spark timing beyond 345º does not influence the phasing of CA50, because combustion has transitioned entirely to HCCI for these later timings.

The total fraction of combustion by the reaction front (FCRF) is shown in Figure 5.4 for combustion efficiencies greater than 99%. Figure 5.4 (left) shows those cases with FCRF less than or equal to 90% for a given IMAT with CA50 at TDC. These cases are deemed to be SACI-like, while the heat release in the cases in Figure 5.4 (right) is dominated by deflagration combustion (FCRF > 90%), which are deemed to be SI-like. At a given CA50 for the SACI cases in Figure 5.4 (left), it is observed that increasing IMAT tends to increase the fraction of combustion due to auto-ignition, as the hotter mixtures are closer to the ignition temperature at the beginning of the cycle. For a given IMAT below 490 K and moving from advanced to retarded CA50, a gradual reduction is noted in the FCRF. This decreasing fraction of deflagration combustion is attributable in part to the more reactive mixture state at the initialization of the flame as CA50 retards, resulting in a greater fraction of compression ignition. The FCRF eventually reaches a minimum before increasing again at very late CA50's, likely because of the expanding cylinder volume and the additional time for end-gas heat loses, both of which affect end-gas temperatures. The 490 K IMAT case shows similar behavior to the cooler IMAT's, except for the spark timings beyond 345º (CA50 greater than 372°) where combustion is almost entirely due to auto-ignition.

Cylinder pressure and the non-dimensionalized rate of heat release are shown in Figure 5.5 for the SACI cases in Figure 5.4 (left) with CA50's between 362° and 364°.

The cylinder pressure plots are of the domain's average pressure, while the heat release rates are smoothed by simple averaging with the values from the four previous and four later time steps. The heat release is non-dimensionalized with the peak value for the 490 K IMAT case shown in Figure 5.5. The shape of the heat release rate profiles reveal the initially low rates of heat release associated with the reaction front, while the transition to auto-ignition dominated combustion is noticeable when heat release rates become elevated. From the figure, an advance in the phasing of the deflagrative heat release process is shown to occur as spark is advanced with lower IMAT. The duration of the deflagration event becomes longer with lower IMAT, consistent with the increased FCRF shown in Figure 5.4. The phasing of auto-ignition combustion is also shown to occur later into the cycle as FCRF is increased, while peak auto-ignition heat release rates are observed to decrease significantly as the FCRF is increased. By releasing more heat with the deflagration prior to auto-ignition, there is less end-gas chemical energy available to the auto-ignition event. In addition, the auto-ignition heat release is phased later into the expansion process as IMAT is lowered and the FCRF is increased. Due to the retardation of the auto-ignition event, there is additional time for heat losses to occur and for thermal stratification to develop, which will also tend to lower peak heat release rates.

The maximum rates of pressure rise with respect to crank angle are shown in Figure 5.6. Starting at retarded CA50's for the SACI points in Figure 5.6 (left), increases in pressure rise rate are observed with advances in CA50 timing. This behavior is similar to that of HCCI engines, where late combustion can proceed in conjunction with expansion and the later combustion phasing provides additional time for the development of thermal stratification. These effects tend to lower the overall rate of heat release, while extending the heat release duration [6]. However, as CA50 continues to be advanced in Figure 5.6 (left), a noticeable decrease in the pressure rise rate occurs for the three highest IMAT cases. This behavior can be attributed largely to the increase in

FCRF with advanced CA50's noted in Figure 5.4 (left). Consistent with the above discussion, releasing more heat with the deflagration prior to auto-ignition results in less end-gas chemical energy available for release during auto-ignition. Consequentially, the pressure rise during this near constant volume auto-ignition combustion process is reduced. The behavior for the SI-like cases in Figure 5.6 (right) results from the fact that pressure rise rates increase with the shorter burn durations that occur as combustion is phased closer to TDC.

Pressure discontinuities and their associated pressure waves can result in objectionable noise and structural damage to the engine. The intensity of these waves can be gauged with a ringing intensity correlation which uses the peak time rate of pressure rise [7]. The impact of the above lower overall rates of pressure rise on ringing intensity is apparent in Figure 5.7. Given the similarity of Figure 5.6 and Figure 5.7, it can be concluded that much of the ringing intensity behavior is associated with combustion's effect on the pressure rise rate. Using the ringing intensity limit of 5 MW/m^2 previously used for HCCI combustion [3, 8], it is apparent for the SACI cases shown in Figure 5.7 (left) that compliance with ringing limits may be maintained through operation with higher levels of FCRF enabled through lower IMAT operation. Additionally, for a given IMAT, the non-monotonic behavior of ringing intensity observed for most of the SACI cases shows that further reductions in ringing can be made by advancing spark ignition timing so that FCRF increases. Unfortunately, these timing advances locate CA50 in an area of lowered closed cycle efficiency. As a bounding example, an SI case is shown in Figure 5.7 (right). While the ringing intensities were elevated for advanced ignition timings, the ringing intensity limits for the SI-like cases were never violated.

The highest temperature observed within the KIVA domain for the entire cycle is shown in Figure 5.8. While NO_x chemistry was not simulated in this work, the maximum domain temperature observed over the engine cycle was used as a NO_x surrogate. This

temperature was used to evaluate the cycle's potential for NO_x formation, because in concepts with extended burn durations such as SACI, large temperature differences may exist between the early and late burning portions of the charge. The elevated peak temperatures will not be captured in variables such as the mean gas temperature.

Figure 5.8 (left) shows the additional benefit of lower IMAT operation. Considering a CA50 near TDC, where IMAT ranges from 350 to 470 K, it can be observed that peak temperatures are lowered by approximately 300 K with low IMAT operation. Also from Figure 5.8 (left), it is apparent that in order to comply with a peak burned gas temperature limit of 2000 K, that CA50 must be retarded to a non-optimal value shortly after 380°. Three IMAT points in proximity to the 2000 K temperature limit can be identified for IMAT ranging from 350-390 K. From Figure 5.8 (right), the resulting impact of the late combustion process on cycle efficiency is clear. Efficiencies between 33 and 37.5% were observed for these late 350-390 K IMAT points, showing that significant compromises in efficiency must be made for compliance with the NO_x emissions constraints under the current operating conditions.

5.2 Conclusions

A parametric study of spark timing and intake manifold temperature was performed to determine if SACI can be used as a means for increasing engine load while maintaining acceptable engine performance and while complying with ringing and peak burned gas temperature constraints. Under the conditions examined, significant gains in load were observed as the initial charge densities were increased through the lowering of intake manifold temperature. In many of the SACI cases, ringing was reduced by increasing the fraction of heat release due to deflagration. Combustion in many of the high load cycles was also dominated by the deflagrative combustion mode, however, peak flame temperatures remained elevated for these cases, limiting the maximum

achievable thermal efficiency. Sweeping conclusions regarding the utility of SACI should not be drawn based upon the results of this preliminary study, as changes to one of several variables not modified in the current work may significantly alter the simulation outcome.

Table 5.1: The engine geometry used in the current study.

Compression Ratio	12.4:1
Bore (mm)	86.0
Stroke (mm)	94.6
Intake Valve Closing (ABDC)	20°
Exhaust Valve Opening (BBDC)	40°
Fuel	Iso-octane

Table 5.2: The minimum range of individual parameters examined for the spark ignited cases in this study, at MAP = 1.05 bar and Φ= 0.45.

IMAT (K)	490	470	450	430	410	390	370	350
Spark (^{o} BTDC)	80	60	40	30	20	10	0	

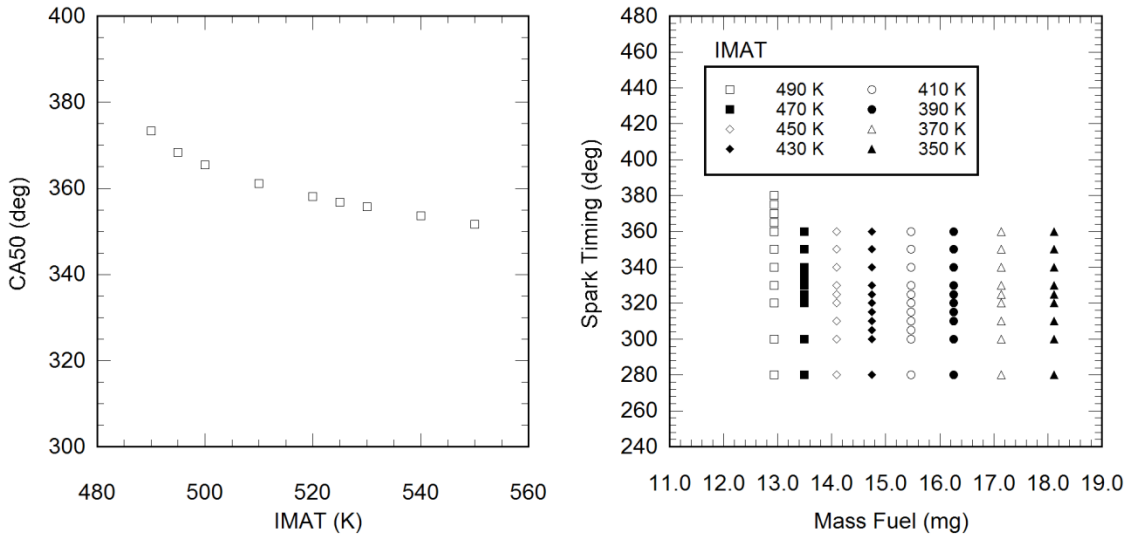

Figure 5.1: The CA50 obtained when sweeping IMAT for HCCI combustion (left) and the range of spark timings examined for a given fuel delivery/IMAT (right).

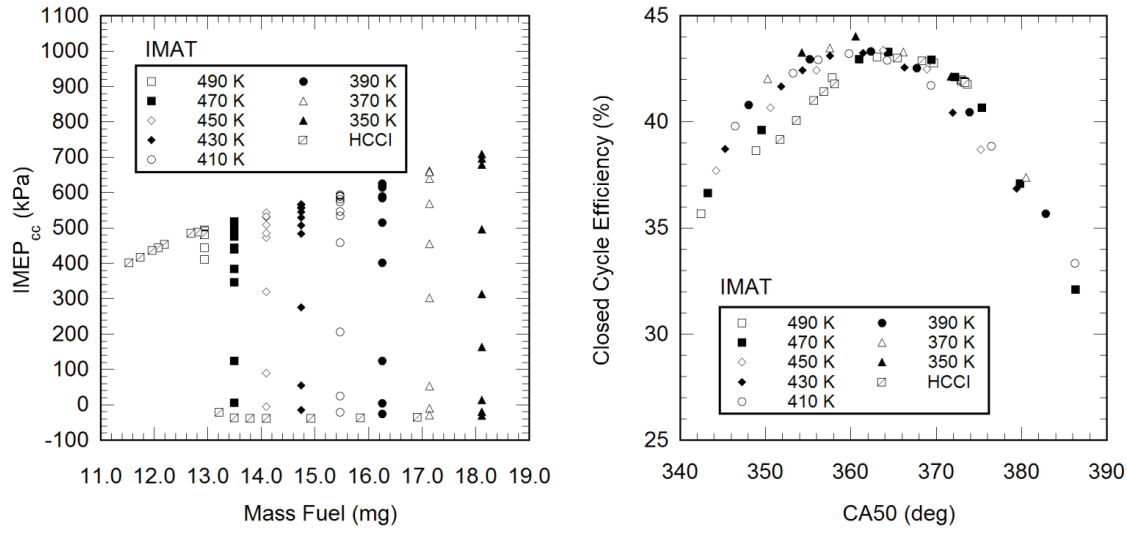

Figure 5.2: $IMEP_{cc}$ obtained for a given fuel delivery/IMAT and spark timing (left). The closed cycle indicated efficiency vs. CA50 (right).

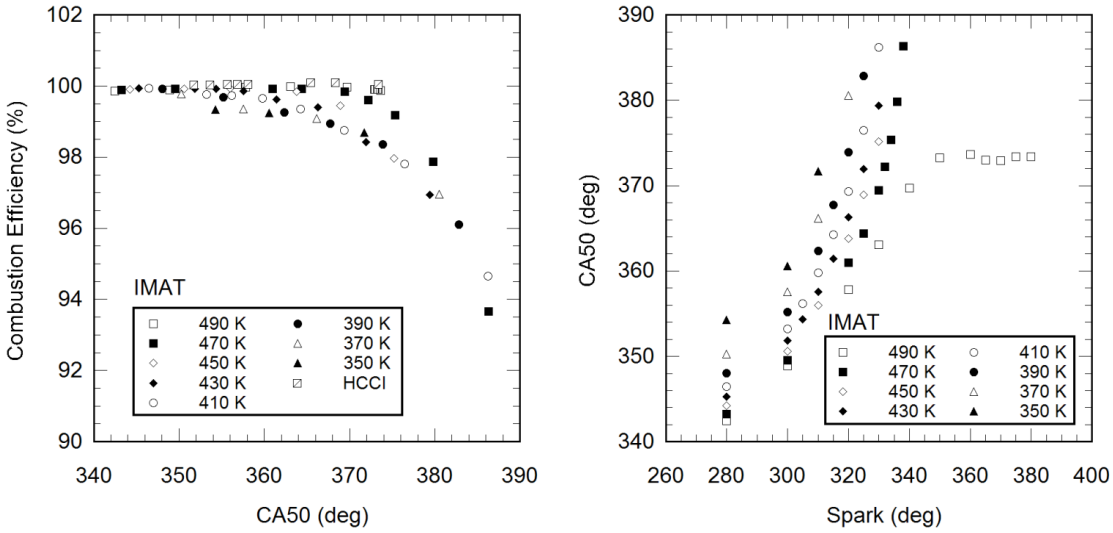

Figure 5.3: Combustion efficiency as a function of crank angle (left) and CA50 as a function of spark timing (right).

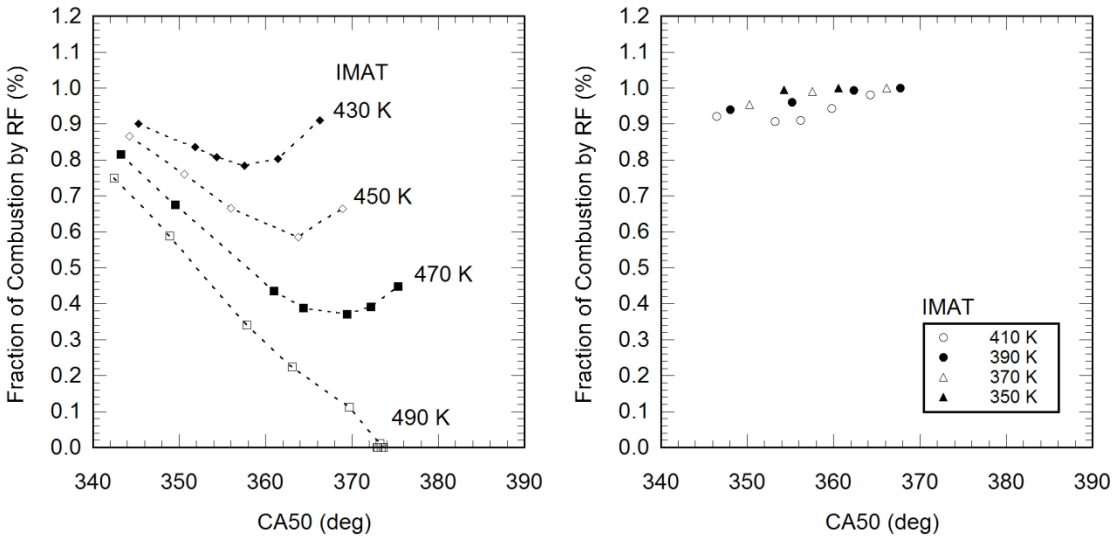

Figure 5.4: Fraction of combustion due to the reaction front (FCRF), for SACI (left) and SI combustion (right) for cases with combustion efficiency greater than 99%.

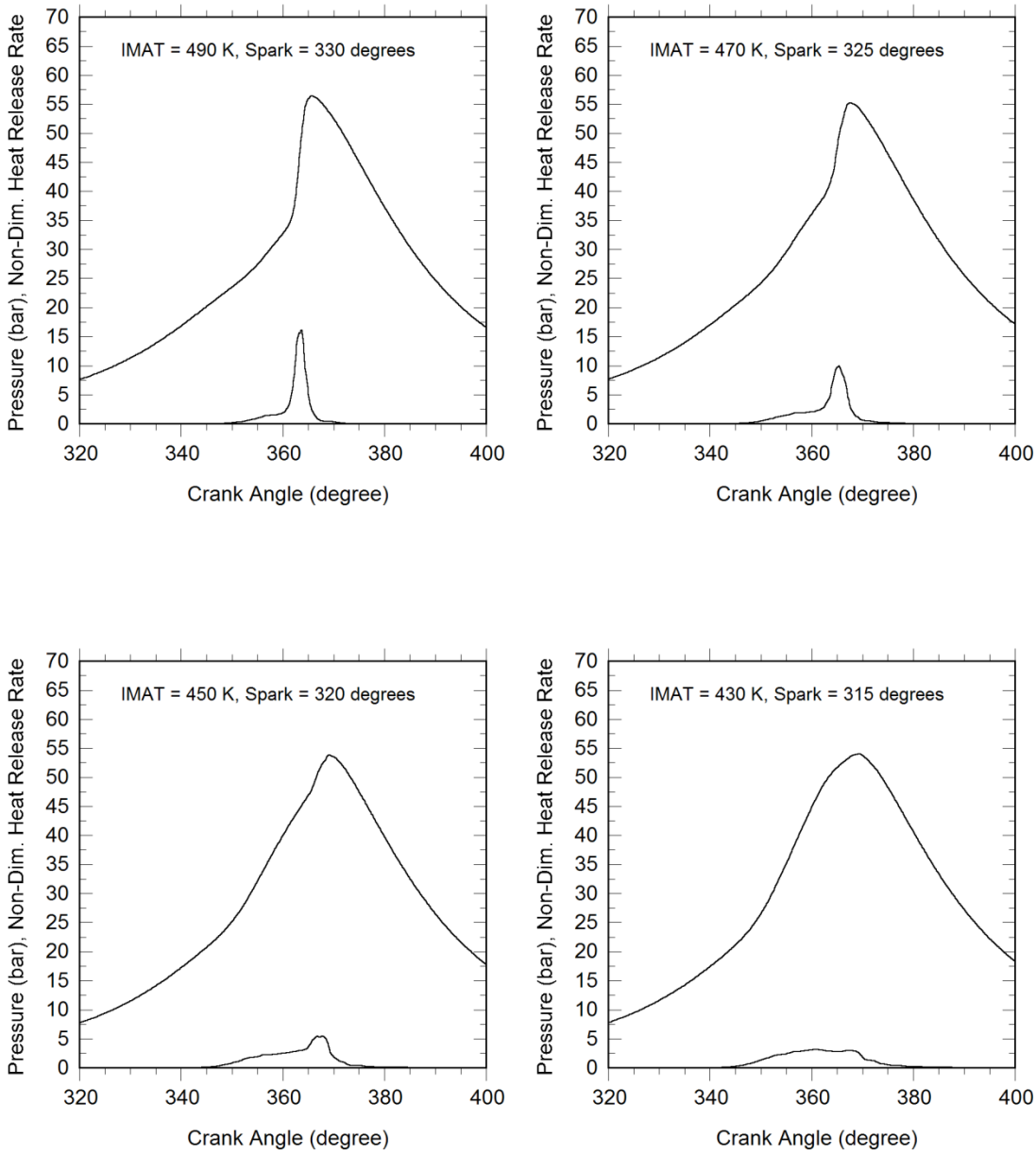

Figure 5.5: Cylinder pressure and non-dimensional rate of heat release vs. crank angle for SACI cases with IMAT ranging from 430 – 490 K, with CA50 between 362º and 364º crank angle.

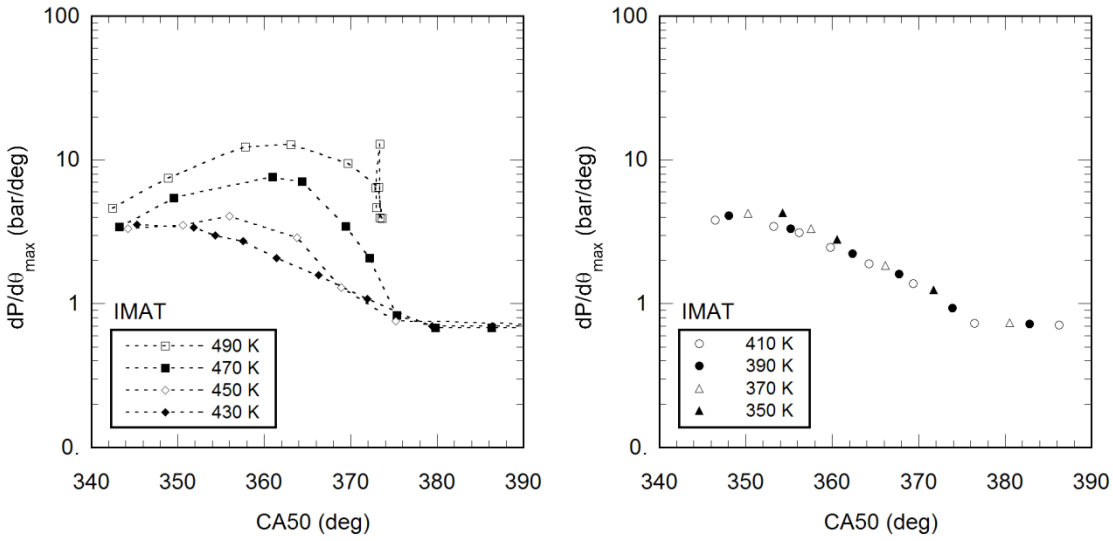

Figure 5.6: $dP/d\theta_{max}$ as a function of CA50 for SACI (left) and SI combustion (right).

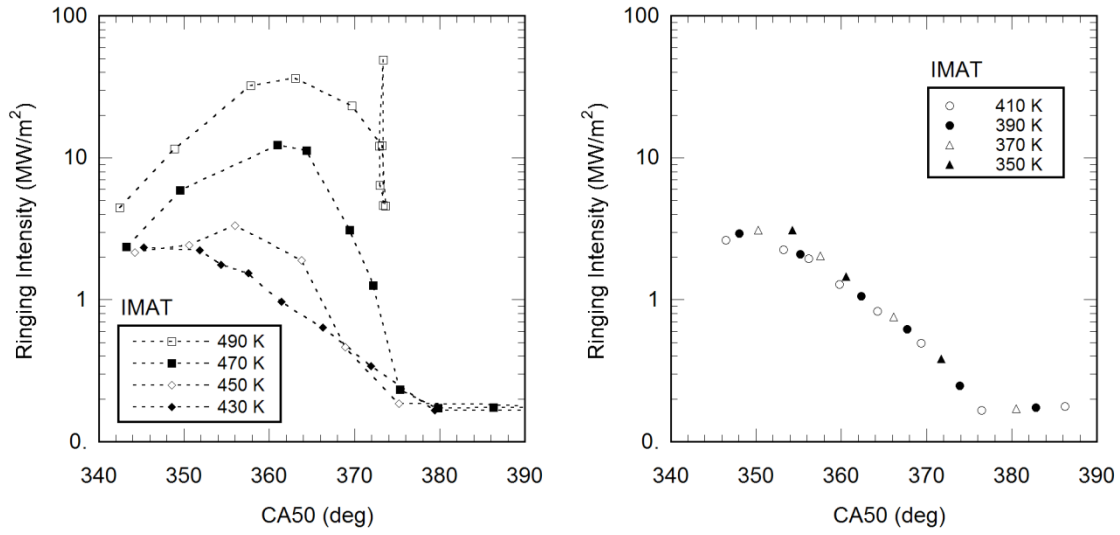

Figure 5.7: Ringing intensity vs. CA50, for SACI (left) and SI combustion (right).

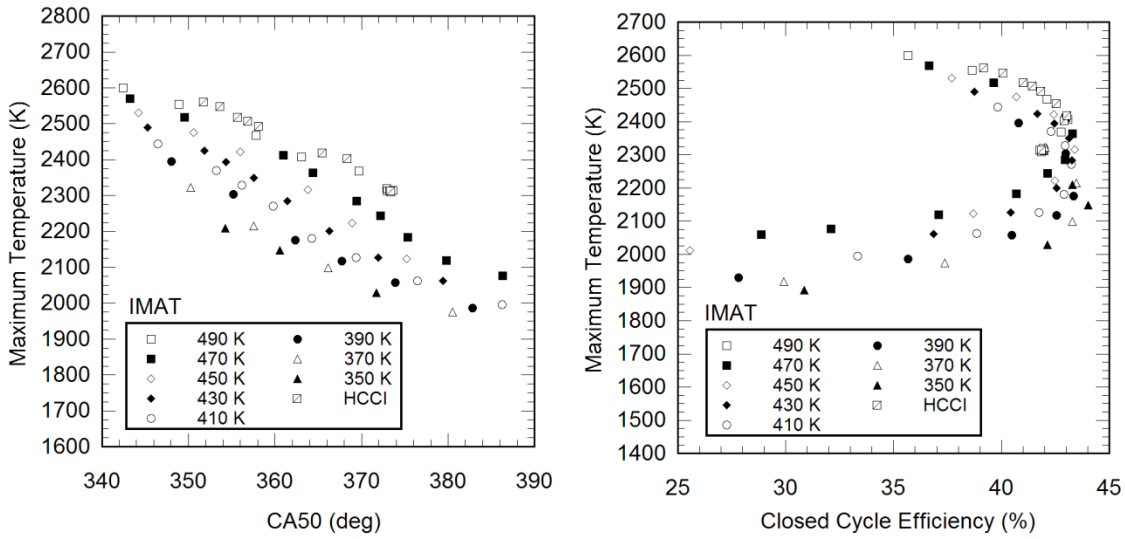

Figure 5.8: Maximum cycle temperature vs. CA50 (left) and closed cycle efficiency (right).

5.3 References

1. Olsson, J.O., Tunestal, P., Johansson, B., Fiveland, S.B., Agama, R., Willi, M., and Assanis, D.N., "Compression Ratio Influence on Maximum Load of a Natural Gas Fueled HCCI Engine," SAE Paper 2002-01-0111, 2002.

2. Hiltner, J., Fiveland, S.B., Agama, R., and Willi, M., "System Efficiency Issues for Natural Gas Fueled HCCI Engines in Heavy-Duty Stationary Applications," SAE Paper 2002-01-0417, 2002.

3. Yun, H., Wermuth, N., and Najt, P.M., "Extending the High Load Operating Limit of a Naturally-Aspirated Gasoline HCCI Combustion Engine," SAE Paper 2010-01-0847, 2010.

4. Olsson, J.O., Tunestal, P., Ulfvik, J., and Johansson, B., "The Effect of Cooled EGR on Emissions and Performance of a Turbocharged HCCI Engine," SAE Paper 2003-01-0743, 2003.

5. Heywood, J.B., 1988, *Internal Combustion Engine Fundamentals*. McGraw-Hill, New York.

6. Dec, J.E., Hwang, W., and Sjöberg, M., "An Investigation of Thermal Stratification in HCCI Engines Using Chemiluminescence Imaging," SAE Paper 2006-01-1518, 2006.

7. Eng, J.A., "Characterization of Pressure Waves in HCCI Combustion," SAE Paper 2002-01-2859, 2002.

8. Dec, J.E., and Yang, Y., "Boosted HCCI for High Power without Engine Knock and with Ultra-Low NOx Emissions - Using Conventional Gasoline," SAE Paper 2010-01-1086, 2010.

CHAPTER 6

SUMMARY, CONCLUSIONS AND RECOMMENDATIONS

6.1 Summary

The work presented in this document has focused on the development and exercise of a detailed SACI combustion model. In Chapter 2, the need for reaction front data within the ultra-dilute, high pressure and preheat temperature conditions characteristic of SACI combustion was addressed. Steady, one dimensional premixed laminar reaction fronts were simulated with Φ, T_u and pressure ranging from 0.1 to 1.0, 298 to 1000 K and 1 to 250 bar, respectively. The range of these simulations extends upon earlier analytical studies which were focused primarily on the SI combustion regime and covered a range of conditions beyond that for which experimental data is available. Correlations for the burning velocity and front thickness, produced with the steady simulation results, showed good agreement with the simulations; and where applicable, with experimental burning velocities obtained from both atmospheric pressure burners and high pressure combustion bombs. Many of the above burning velocity simulations were in close proximity to the conditions required for auto-ignition of the end-gas. Additional one-dimensional simulations for both a steady flow reactor and for a transient reaction front were performed to examine the combustion regime, structure and general behavior of the reaction front as it propagated into an auto-igniting end gas.

With the physical understanding developed from the above simulations, a sub-grid model capable of capturing SI, SACI and HCCI combustion modes, KIVA-CMFZ (KIVA Coherent Flamelet Multi-Zone), was formulated and subsequently implemented into KIVA-3V. The model formulation and implementation were described in detail in Chapter 3. Using the burning velocity and front thickness correlations from Chapter 2, KIVA-CFMZ combines the Coherent Flamelet Model for the modeling of turbulent reaction front propagation with the fully coupled Multi-Zone model for the modeling of detailed end and product gas chemical kinetics.

In Chapter 4, KIVA-CFMZ was compared to data from SI and SACI combustion regime experiments. This comparison assessed the performance of the sub-grid combustion models and the laminar reaction front burning velocity and thickness correlations within the SI and SACI combustion regimes. Using flame model constants with magnitudes similar to those previously reported for SI combustion simulations, the model was shown to be capable of predicting trend-wise agreement with the cylinder pressure profiles from the SI and SACI engine experiments. The evolution of reaction fronts observed in the experimental chemiluminescence images of SACI combustion was similar to that of the predicted flame surface density iso-volume, which originated at the spark ignition source and propagated through the combustion chamber prior to the ignition of the end-gas. Simulated flame surface density magnitudes were similar to those previously reported for both engine experiments and simulations.

Finally, in Chapter 5, a parametric study of spark timing and intake manifold temperature was performed under highly dilute conditions to gauge the utility of SACI

combustion as a mechanism for increasing engine loads, while maintaining acceptable engine performance characteristics.

6.2 Conclusions

In the steady reaction front study of Chapter 2, it was observed that as long as preheat temperatures were sufficiently elevated, moderate reaction front burning velocities could be supported at equivalence ratios typical for mid and high load HCCI operation. It was noted that T_b generally had to exceed 1500 K in order for burning velocities to be greater than 5 cm/s. At a given T_b, it was also shown that burning velocities increased when moving from the SI to the SACI combustion regime, that is by increasing preheat temperature while decreasing equivalence ratio. Under certain conditions with low T_b and elevated T_u and pressure where steady flames were lacking, it was shown that the lack of steady results was largely a result of the insufficient time available to the reaction front to achieve steady propagation prior to auto-ignition.

Also in Chapter 2, for fronts propagating into auto-igniting end-gases, combustion within the steady flow reactor simulations became chemically dominated once the temperature at the beginning of the reaction front approached 1100 K, suggesting that the end-gas temperature may be used as a criterion for marking the transition from deflagration-like to chemically dominated combustion in practical engine simulations. In the transient reaction front simulations, it was shown that the reaction front was initially within the normal deflagration regime, where the peak absolute values of the rate of energy change due to heat conduction and energy release within the front were comparable. The minimal variation in front thickness coupled with the diminishing temperature difference between the end and burned gasses with end-gas reaction progress

led to the continuous decrease in the maximum temperature gradient within the front. The reduced contribution of heat conduction to energy transfers within the front stemmed from this decrease in the peak temperature gradient. Under the conditions examined, heat conduction became negligible once end-gas temperatures exceeded approximately 1600 to 1800 K. These results are consistent with the outcome a transport coefficient sensitivity analysis, where reaction front propagation rates were shown to be sensitive to transport up to approximately 1600 K. The burning velocity correlation in this work was reasonably capable of reproducing the transient burning velocities, up to end-gas temperatures of 1100 K. Even though significant reaction front acceleration was shown for end-gas temperatures beyond 1100 K, the front contributed minimally to the overall end-gas reactant consumption beyond this temperature. The minimal consumption of the end-gas mixture by the reaction front beyond 1100 K resulted from the limited time for front propagation during end-gas thermal runaway and from the decreasing importance of transport within the front during auto-ignition.

In Chapter 3, a generalized sub-grid level combustion model, KIVA-CFMZ, is formulated for SI, SACI and HCCI combustion modeling with KIVA-3V. In Chapter 4, KIVA-CFMZ is compared to data from SI and SACI combustion experiments. Using the correlated laminar flame speed data from Chapter 2, KIVA-CFMZ was capable of predicting trend-wise agreement with cylinder pressure and imaging data from an optical SACI engine. In addition, the turbulent reaction front simulations performed with KIVA-CFMZ utilized the ITNFS flame stretch model of Meneveau and Poinsot, which was developed from direct simulations of flame vortex interaction. An upper limit to the flamelet regime, representing the complete quenching of the flamelet by the turbulent

flow field, was defined by Meneveau and Poinsot as the onset of zero or negative stretch predictions from the ITNFS model. Therefore, the mere presence of flame surface density in the current SACI simulations suggests that although ultra-dilute, the reaction front remains thin and within the flamelet regime under the high pre-heat temperature and pressure conditions of SACI combustion. Under certain conditions, the predicted combustion mode transition from reaction front propagation to end-gas auto-ignition was shown to be abrupt during SACI combustion. Under other conditions, concurrent front propagation and auto-ignition were noted on a global basis. The transition to auto-ignition occurred when charge compression heating through boundary work and heat release combined to drive the end-gas to its ignition temperature. Therefore, the inclusion of deflagrative combustion modes provides an additional degree of freedom for the execution and control of low temperature combustion processes.

In Chapter 5, the parametric study of spark timing and intake manifold temperature showed that operation at lower intake manifold temperatures relative to HCCI was made possible through the additional compression heating provided by the reaction front. Significant load increases resulted from the additional fuel delivery made possible through the resulting increase in trapped air mass. For many of the SACI cases, a reduction in ringing was observed with increases in the fraction of heat release due to the reaction front. Lower ringing intensities were attributable to the reduction in the end-gas chemical energy release and the diminished pressure rise associated with auto-ignition. While combustion in many of the high load cycles was dominated by the deflagrative combustion mode, peak flame temperatures remained elevated. To comply with NO_x emissions constraints, combustion was forced later into expansion, effectively

limiting the maximum achievable thermal efficiency of the cycle. It is anticipated that further variation to one of the several variables fixed during the current study may significantly change the simulation outcomes and conclusions.

6.3 Recommendations for Future Work

There is currently a lack of fundamental experimental data for the validation of the one-dimensional laminar reaction front simulations. Given the relatively small ratio of ignition delay to flame times associated with the SACI regime, it is anticipated that fast acting devices such as shock tubes, rapid compression machines or gas guns will be required to obtain this data. In addition, DNS studies could be performed to provide further insight into reaction fronts within the SACI regime. The reason for the increase in burning velocity observed when transitioning from the SI to SACI combustion regime at fixed burned gas temperature should be further investigated and identified.

The simple spark-ignition model of initial flame development used in the current work lacks key physical phenomena such as the spark energy deposition, the subsequent formation of the ignition kernel and the external heat losses from the flame kernel to the spark plug. In addition, the Lewis number effect on the correlated laminar burning velocity of the geometrically stretched flame kernel was neglected. A more fundamental simulation, either multi-dimensional or in one dimensional spherical coordinates, could be developed or used to either to directly simulate or further develop simplified models for these critical processes. Additional experiments could be defined to further investigate these processes and to validate any newly developed models. These experiments could include the fast acting devices mentioned above, and could also include both optical and metal engine studies with ion probes or other visualization capabilities.

The 1-D transient reaction front simulations performed in this work examined the transition from a pre-existing deflagrative reaction front to the spontaneous ignition front regime. Fronts originating from hotspots have been observed in multiple shock tube, RCF and optical engine experiments. Further transient simulations can be performed to provide insight into the nature of these fronts and to subsequently guide the development of mathematical models for the description of this process.

The ITNFS aerodynamic flame stretch model used in this work was developed under SI combustion conditions. The ability of this model to accurately predict flame stretching given characteristic velocity and length scale information from within the SACI combustion regime should be verified with direct simulation. Additional insight is also needed for the empirical flame surface density destruction terms needed for the modeling of flamelet merging and annihilation, and how this process proceeds within the SACI regime. While the computational expense of direct simulations continues to decline through advances in processing speed and parallelization, the Multi-Zone approach may serve as a potential tool for reducing the cost of detailed chemistry calculations in regions of the DNS domain lacking significant compositional or thermal stratification.

More pragmatically, additional KIVA-CFMZ model validation is required with metal engine data from SI, SACI and HCCI experiments. This data would ideally originate from a single experimental platform and use an exact mesh of the experimental combustion chamber in the simulations. Experiments employing air and residual dilute mixtures for both gasoline and iso-octane fuels should be simulated, and the ability of existing or newly developed sub-models to properly simulate these conditions should be assessed.

Because of low temperature combustion's high cycle to cycle variability, resulting in part from the feedback from the previous cycle, open cycle runs should be performed with KIVA-CFMZ, or KIVA-CFMZ could be coupled to 1-D system gas dynamic

package such as GT-Power to provide further fundamental understanding and recourse for these issues.

Finally, the KIVA-CFMZ model should be further exercised to provide additional fundamental understanding of SACI. The model should be used to improve upon many of the shortcomings of HCCI, including issues associated with ignition timing, heat release rate control and power density. These simulations should be performed in tandem with metal engine experiments, not only to guide the experiments but also to serve as an experimental diagnostic tool. The model should also be used to examine situations not realistically performed by zero dimensional SACI simulations, which are currently in the process of being developed. These situations include cases where specific geometric details are to be investigated or where stratification is employed to affect the overall SACI combustion process.